Final Technical Report to the
Research Partnership to Secure Energy for America, Department of Energy

Prediction of Fault Reactivation in Hydraulic Fracturing of Horizontal Wells in Shale Gas Reservoirs, Task 09122-06

May 16, 2011 – August 30, 2015

By

Ebrahim Fathi

West Virginia University
Petroleum and Natural Gas Engineering Department
347 Mineral Resources Building
401 Evansdale Drive
Morgantown, WV 26506

Research Team Members:

Professor Sam Ameri CO.PI; Jinqing Bao, Ph.D (POST-DOC)

Graduate Students:

Ph.D student: Andrew Jenkins;

MSc Students: Liliia Reddy; Nupur Gupta; Amir Ansari; Zachary Cox

Disclaimer: This report was prepared as an account of work sponsored by an agency of the United States Government. Neither the United States Government nor any agency thereof, nor any of their employees, makes any warranty, express or implied, or assumes any legal liability or responsibility for the accuracy, completeness, or usefulness of any information, apparatus, product, or process disclosed, or represents that its use would not infringe privately owned rights. Reference herein to any specific commercial product, process, or service by trade name, trademark, manufacturer, or otherwise does not necessarily constitute or imply its endorsement, recommendation, or favoring by the United States Government or any agency thereof. The views and opinions of authors expressed herein do not necessarily state or reflect those of the United States Government or any agency thereof.

Abstract

Shale gas reservoirs are characterized by relatively low porosity and ultra-low permeability, i.e. in the order of Nano-Darcy. Exploiting these types of formations requires the use of horizontal drilling and multi-stage hydraulic fracturing technology, which has been continuously developed over the past few decades in order to make these types of reservoirs economically viable. These types of processes drastically increase production by achieving a greater wellbore to reservoir contact.

The process of drilling horizontal wells and hydraulic fracture stimulation however may develop unintended changes to the mechanical stability of the reservoir and surrounding area through the redistribution of in-situ stress fields. The change which develops in these in-situ stress differentials may lead to the reactivation of existing faults, fracture or discontinuity under certain circumstances. The implications of these potential hazards and risks related to this reactivation include hydraulic failure of cap rocks, i.e. reservoir fluid leakage to surroundings, failure of fracture treatment, wellbore instability in nearby wells and in severe cases surface subsidence and seismicity events.

In order to further understand the nature of these induced stress changes to the in-situ stress fields, it is necessary to develop a sound and practical methodology to study their influence on the surrounding reservoir. Issues have often been associated with the development of fractures and fracture propagation inside the reservoir as well as poroelastic effects due to fluid injection or production. Stress change and redistribution due to the opening of hydraulic fractures has been investigated to provide more than qualitative reasoning behind many of these issues. The results of these studies have shown the importance of the initial in-situ stress contrast in the horizontal plain on reservoir stress redistribution as well as the development of stresses within the reservoir during the injection process.

In this study, both single and multi-stage hydraulic fracturing treatments have been generated in order to study their impact on multiple faulting environments. This has been studied by using finite element based numerical simulation, developed by the WVU Research Group specifically for these types of problems. Based on these studies, the angle between fracture orientation and fault strike displays a strong effect on the stability of the fault. This effect is seen to be largest in the case of a normal fault and least in a reverse/strike-slip faulting environment. Additionally, the development of stress throughout critical areas, i.e. surrounding discontinuity or fracture, has been studied in-depth to develop a quantitative understanding of the stresses which often interact, distort or alter the in-situ stress fields. Fluid injection during hydraulic fracturing and gas production after stimulation can also have significantly different impact on change and redistribution of stress field in poroelastic environment. A large component of hydraulic fracturing efficiency often lies in the successful development of intended fracture geometries. It has been found through numerical simulation of proppant transport during the fluid injection phase of hydraulic fracturing that the distribution of proppant is often non-linearly distributed. These types of effects lead to unintended developments in geometry and may therefore impact the surrounding stress fields in a less than ideal manner.

This research has displayed a beneficial impact to the study of fault reactivation due to the stimulation of unconventional reservoirs through hydraulic fracturing. Furthering the understanding of such complex subsurface mechanisms aids in achieving a greater wellbore to reservoir contact by increasing the efficiency of the stimulation. This is due to the effective use of injection energy which is spent on fracture propagation, instead of interaction with surrounding fault, fracture or discontinuity.

THIS PAGE IS INTENTIONALL LEFT BLANK

Table of Contents

Abstract iii
List of Figures vii
List of Tables x
Executive Summary xi
1. Introduction 13
1.1. Background 13
1.2. Objectives 17
1.3. Project Scope 18
2. Methodology 21
2.1. Reservoir Assessment 21
2.1.1. Well Information 21
2.1.2. Core Data Information 21
2.1.3. Seismic Survey 22
2.1.4. Field Geomechanical Model 22
2.2. 3D Geomechanical Model 26
2.2.1. Finite Element Model 26
2.2.2. Governing Equations 27
2.2.3. Validation 30
2.3. 2D Coupled Model 33
2.3.1. Finite Element Model 33
2.3.2. Governing Equations 35
2.3.3. Validation 35
2.4. 3D Coupled Model 43
2.4.1. Finite Element Model 43
2.4.2. Governing Equations 44
2.4.3. Validation 44
2.5. Fault Reactivation Assessment 46
2.5.1. Slip-tendency of faults 47
2.5.2. Fault slip-tendency during hydraulic stimulation 49
2.5.3. Numerical analysis of Fault Slip Tendency 51
2.5.4. Effect of a single pressurized fracture on fault stability 52
2.6. Fracture Efficiency Assessment 54

2.6.1. Proppant transport in hydraulic fractures 54
2.6.2. Fracture Geometry and Permeability 55
2.6.3. Fluid flow during production 55
3. Results 59
3.1. Static 3-Dimensional Model 59
5.3.2 Three Fracture Model 61
3.2. Dynamic 2-Dimensional Model 64
3.3. Dynamic 3-Dimensional Model 65
3.4. Fracture Development and Proppant Efficiency 69
3.5. Characterization of Stresses 76
4. Conclusions 95
5. Acknowledgements 99
6. Publications and Presentations 99
7. References 100
8. Appendix 101
8.1. Marcellus Assessment 101
8.2. Geomechanical Model 105
8.3. Finite Element Solution of Static Stress Reservoir 107
8.4. Finite Element Solution with Dynamic Fracture Propagation 115
8.5. Derivation of Fracture efficiency Equations 124
8.6. Derivation of Slip Tendency and Stress Relationships 126
Normal Faulting Environment 128
Strike-Slip Faulting Environment 129

List of Figures

Figure 1 - Illustration of Stratigraphic Structure 23
Figure 2 - Cross-Plot of Gamma Ray and Density 24
Figure 3 - Illustration of the structural model of the area of study 25
Figure 4 - Illustration of the fault location in the structural model 25
Figure 5 - Comparison of original log data and neural network analysis, from left to right, maximum horizontal stress, Young's modulus, Poisson's ratio, minimum horizontal stress, tensile stress and vertical stress (Red: original log; Blue: neural network) 26
Figure 6 - Schematic diagram of the reservoir configuration and variational tetrahedral mesh 31
Figure 7 - Uniform distribution of three principal stresses (psi) 31
Figure 8 - Principal stress field (psi) 32
Figure 9 - Stress distribution on the fault plane (psi) 32
Figure 10 - Variation of the ratio of the shear stress to the effective normal stress on the fault plane 33
Figure 11 - Definition of the model 35
Figure 12 - Fig. 7 Asymptotic and numerical solutions of net pressure at inlet (a), fracture width at inlet (b), half fracture length (c), and fracture width profile (lt = 11.1m) (d) for large toughness case 37
Figure 13 - Asymptotic and numerical solutions of net pressure at inlet (a), fracture width at inlet (b), half fracture length (c), and fracture width profile (lt = 13.5m) (d) for intermediate case 38
Figure 14 - Asymptotic and numerical solutions of net pressure at inlet (a), fracture width at inlet (b), half fracture length (c), and fracture width profile (lt = 14.2m) (d) for large viscosity case 39
Figure 15 - Evolution of injection efficiency for the example of intermediate case with leak-off 39
Figure 16 - Net pressure profiles with l = 4m (a) and l = 8m (b), and virtual net pressure profiles with l0=8m and l1=4m (b) 40
Figure 17 - Asymptotic and numerical solutions of net pressure at inlet (a), fracture width at inlet (b), half fracture length (c), and fracture width profile (lt = 11.1m) (d) of the examples with large toughness and zero leak-off 42
Figure 18 - Number of iteration in the first 100 steps of the large viscosity examples in the square models: (a) examples without leak-off; (b) examples with leak-off. 42
Figure 19 Cohesive Element Fracture Plane 43
Figure 20 Three Dimensional Cohesive Zone Model Discretization for a Single Fracture 44
Figure 21 Thee Dimensional Cohesive Zone Model Discretization for Multiple Fractures 44
Figure 22 - Numerical results for the CZ Model and semi-analytical solution for the LEFM model. 46
Figure 23 - Flow chart of fracture-proppant efficiency research 56
Figure 24 - Overlook of the gas reservoir model for simulation 57
Figure 25 - (a) Single fracture propagation model with 100 elements (HFWVU) (b) Discretization of the equivalent quarter model with finite elements in HFWVU 57
Figure 26 Ratio of Shear Stress by Net Pressure Surrounding a Single Fracture in a Normal Faulting Environment 59
Figure 27 Ratio of Normal Stress by Net Pressure Surrounding a Single Fracture in a Normal Faulting Environment 59
Figure 28 Ratio of Shear Stress by Net Pressure Surrounding a Single Fracture in a Strike-Slip Faulting Environment 60
Figure 29 Ratio of Shear Stress by Net Pressure Surrounding a Single Fracture in a Strike-Slip Faulting Environment 60

Figure 30 Slip-Tendency for a Normal Faulting Environment Surrounding a Single Fracture, Ts=0.6 60
Figure 31 3-D Slip-Tendency For a Normal Faulting Environment And Single Fracture, Ts=0.6 61
Figure 32 Slip-Tendency for a Strike-SLip Faulting Environment And Single Fracture, Ts=0.6 61
Figure 33 3-D Slip-Tendency For a Strike-Slip Faulting Environment And Single Fracture, Ts=0.6 61
Figure 34 Ratio of Shear Stress by Net Pressure Surrounding Multiple Fractures 62
Figure 35 Ratio of Shear Stress by Net Pressure Surrounding Multiple Fractures 62
Figure 36 Ratio of Shear Stress by Net Pressure Surrounding Multiple Fractures 62
Figure 37 Ratio of Shear Stress by Net Pressure Surrounding Multiple Fractures 63
Figure 38 Slip-Tendency for a Normal Faulting Environment Surrounding Multiple Fractures, Ts=0.6 63
Figure 39 3-D Slip-Tendency For a Normal Faulting Environment And Multiple Fractures, Ts=0.6 63
Figure 40 Slip-Tendency for a Strike-SLip Faulting Environment Surrounding Multiple Fractures, Ts=0.6 64
Figure 41 3-D Slip-Tendency For a Strike-SLip Faulting Environment And Multiple Fractures, Ts=0.6 64
Figure 42 The Development of the Fracture Profile in Three Concurrent Fractures at 5 Meters Spacing. 65
Figure 43 The Development of the Von Mises Stress Surrounding Three Concurrent Fractures at 5 meters Spacing 65
Figure 44 Central Fracture Pressure Profile of 3D Solution at 5 Meters Spacing 66
Figure 45 Central Fracture Width Profile of 3d Solution at 5 Meters Spacing 66
Figure 46 Offset Fracture Pressure Profile of 3D Solution at 5 Meters Spacing 66
Figure 47 Offset Fracture Width Profile of 3D Solution at 5 Meters Spacing 66
Figure 48 Three Dimensional Fracture Geometry at T=30s 67
Figure 49 Three Dimensional View of Fracture Geometry at t=60s 67
Figure 50 Pressure and Width of a Central Fracture Versus Offset Fractures 68
Figure 51 Single Fracture Development Versus Simultaneous Fracture Development 68
Figure 52 - Permeability (left) and pressure (right) distribution in reservoir and hydraulic fracture, considering zero proppant settling velocity 69
Figure 53 - Permeability (left) and pressure (right) distribution in reservoir and hydraulic fracture, considering dynamic proppant settling velocity 69
Figure 54 - Influence of proppant settling on dimensionless productivity index, the proppant size is 0.8mm 70
Figure 55 - The effect of proppant size on dimensionless productivity for different permeability reservoir 71
Figure 56 - The effect of relative proppant density on dimensionless productivity for different permeability reservoir 72
Figure 57 - Influence of Non-Darcy effect on dimensionless productivity index 72
Figure 58 - The effect of proppant size and volume portion combination on dimensionless productivity 73
Figure 59 Pareto chart shows the importance of parameters evaluated on the t-value of original case .. 75
Figure 60 Normal plot of the standardized effects of original case shows the importance of parameters 76
Figure 61 Elastic Modulus Effect on Fracture Length 77
Figure 62 Elastic Modulus Effect on Fracture Width 77
Figure 63 Poisson Ratio Effect on Fracture Length 77
Figure 64 Poisson Ratio Effect on Fracture Width 77
Figure 65 Illustration of Expected Single Fracture 78
Figure 66 Illustration of expected Multiple Fractures 78

Figure 67 Stress Change in the X-Direction 79
Figure 68 Stress Change in the Y-Direction 79
Figure 69 Illustration of Line Locations for Stress-Change Plots 80
Figure 70 The Static Component Stress Distribution Surrounding a Single Fracture, t=60s 81
Figure 71 The Static Principle Stress Distribution Surrounding a Single Fracture, t=60s 81
Figure 72 The Static Component Stress Profile Surronding a Single Fracture, t=60s 82
Figure 73 The Static Principle Stress Profile Surrounding a Single Fracture, t=60s 82
Figure 74 The General Transient Behavior of Stress Surrounding a Single Fracture, t=0 to 60s 82
Figure 75 The Static Component Stress Behavior Surrounding Dual Fractures at 5 Meters Spacing, t=60s 83
Figure 76 The Static Principle Stress Distribution Surrounding Dual Fractures at 5 Meters Spacing, t=60s 83
Figure 77 The Static Component Stress Profile Along the Outermost Fracture in a Dual Fracture System at 5 Meters Spacing, t=60s 84
Figure 78 The Static Principle Stress Profile Along the Outermost Fracture in a Dual Fracture System at 5 Meters Spacing, t=60s 84
Figure 79 The Static Component Stress Profile Along the Reservoir Centerline Between Dual Fractures at 5 Meters Spacing, t=60s 84
Figure 80 The Static Principle Stress Profile Along the Reservoir Centerline Between Dual Fractures at 5 Meters Spacing, t=60s 85
Figure 81 The General Transient Behavior of Stress Surrounding Dual Fractures at 5 Meters Spacing, t=0 to 60s 85
Figure 82 The Static Stress Distribution Surrounding a System of Three Fractures at 5 Meter Spacing, t=40s 86
Figure 83 The Static Principle Stress Distribution SUrrounding Three Fractures at 5 Meter Spacing, t=40s 86
Figure 84 The Static Component Stress Profile Along the Outermost Fracture in a Three Fracture System at 5 Meters Spacing, t=40s 87
Figure 85 The Static Principle Stress Profile Along the Outermost Fracture in a Three Fracture System at 5 Meters Spacing, t=40s 87
Figure 86 The Static Component Stress Profile Along the Center Fracture In A Three Fracture System at 5 Meters Spacing, t=40s 88
Figure 87 The Static Principle Stress Profile Along the Center Fracture in a Three Fracture System at 5 Meters Spacing, t=40s 88
Figure 88 The Dynamic Behavior of the Principle Stresses, t=0 to 60s 88
Figure 89 The General Transient Behavior of Stress Surrounding the Three Fracture System at 5 Meters Spacing, t=0 to 40s 89
Figure 90 Von Mises Stress with Relation to the Fracture Length and Distanct from the Fracture Tip at t=60s for a Single Fracture 89
Figure 91 Maximum Von Mises Stress Behavior Surrounding a Single Fracture 90
Figure 92 Zones of Influence Surrounding A Single Fracture 91
Figure 93 Points of Concern for Static Von Mises Stress Distribution 91
Figure 94 Critical Distance of the Von Mises Stress from the Point of Injection 93
Figure 95 - Young's Modulus of Marcellus Shale 101

Figure 96 - Poisson's Ratio of Marcellus Shale 101
Figure 97 - Tensile Stress of Marcellus Shale 102
Figure 98 - Minimum Horizontal Stress of Marcellus Shale 102
Figure 99 - Synthetic Seismogram, Real Seismic Trace and Well Tops (Hardie Unit 1) 103
Figure 100 - Readjustments of Synthetic Seismogram 104
Figure 101 Illustration of Horizons Picked on Seismic Profile 105
Figure 102 - Illustration of the main faults identified through ant tracking 106
Figure 103 - Spatial relationship of faults and surface of different formations 106
Figure 104 Schematic of the 20 Node Brick Element 107
Figure 105 Mapping a Surface Element in Local Coordinates onto Global Coordinates 107
Figure 106 The 3 x 3 x 3 Integration point scheme on hexahedral elements 110
Figure 107 The 2 x 2 x 2 Integration Point Scheme on Hexahedral Elements 110
Figure 108 - Sketch of a plane-strain fluid-driven fracture 115
Figure 109 - Equivalent quarter model 116
Figure 110 - Hydraulic fracturing regimes in (,) space and its evolution line (after [15]). 118
Figure 111 - Discretization of the equivalent quarter model with finite elements 120
Figure 112 - Domain for the interaction integral 121
Figure 113 Analytical Solution of Stress Distribution Surrounding a Pressurized Fracture 126

List of Tables

Table 1 - List of Wells used for Marcellus Data Acquisition 21
Table 2 - Core Data Information by Well 21
Table 3 - Petrophysical Data included by Well 22
Table 4 - Data of stress field and fault of Rangely oil field 30
Table 5 - Parameters for the simulations 36
Table 6 - Parameters for the cohesive zone simulation verifications 44
Table 7 - Base case parameters 70
Table 8 - Parameter setting of PB design 74
Table 9 - PB matrix for 7 variables (-1 = low value, +1 = high value) 74
Table 10 Single Fracture Sensitivity 77
Table 11 - Reservoir properties 78
Table 12 Point Data for Transient Maximum Von Mises Stress for a Single Fracture Case 92
Table 13 Nodal Coordinate Locations of a 20-Node Hexahedron Element 108
Table 14 Location of Integration Points in Hexahedral Elements 111

Executive Summary

This is a final report to be submitted to the Research Partnership to Secure Energy for America (RPSEA) which concludes the research developed throughout the sponsored project 09122-06, "*Prediction of Fault Reactivation in Hydraulic Fracturing of Horizontal Wells in Shale Gas Reservoirs*". The development of this project was carried out from April 2011 and concluded on August 31, 2015 by the West Virginia University Research Group in Morgantown, West Virginia.

The overall goal of this project was to develop an advanced technology to predict fault reactivation and improve the effectiveness of hydraulic fracturing stimulation of horizontal gas shale wells. The specific objectives for this research include the development of a 3D geomechanical stress-displacement and fracturing propagation models to assess the potential of fault reactivation during and after hydraulic fracturing treatments and also to optimize fracture or fracture stage design with multiple perforation clusters under different reservoir/fault conditions.

First year activities focused on (1) collection of well logs, core data and seismic survey information required for study of stress state of reservoir/faults in Marcellus shale. The Hardie area of Marcellus shale in the Appalachian Basin as the study focus. (2) Development of a 3D- geomechanical stress/displacement model for characterization of the state of stress. (3) Development of a 3D propagation model for multiple transverse fractures created simultaneously in one stage.

Second year activities focused on (1) developing a 2D fracture propagation model. (2) Validating 2D propagation model. (3)

Third year activities focused on (1) extending the 2D fracture propagation model to 3D. (2) Validating the 3D propagation model. (3) Identifying the stress changes and optimizing fracture stage design. (4) Organizing results and data in digital and print form.

The conclusion of this project includes (1) field data study (2) static 3D geomechanical model, (3) dynamic 2D coupled model, (4) dynamic 3D coupled model, (5) assessment of stress interaction, (6) final technical report. The coupled model reflects the combination of the geomechanics and fracture propagation.

THIS PAGE IS INTENTIONALL LEFT BLANK

1. Introduction

1.1. Background

Shale gas reservoirs have become a staple of the oil and gas industry with the advancement of horizontal drilling and stimulation techniques, which have drastically increased the total recoverable hydrocarbons throughout the world. These ultra-low permeability formations are often subject to a multitude of varying conditions, through stress and property heterogeneity and anisotropy. This study has focused upon the Marcellus shale in the northeastern United States in order to determine the specific impacts of hydraulic fracturing in order to develop more efficient stimulation and treatment plans.

Shale reservoirs differ entirely from the traditional reservoir development techniques seen in the past which consist primarily of exploiting naturally permeable beds and formation traps. Unlike these traditional reservoirs, such as sandstones or carbonates, shale serves as both the trap and source rock for hydrocarbons, whereas conventional reservoirs serve only for the accumulation of hydrocarbons from another organic source. Conventional reservoir development allows for the profitable production of hydrocarbons without the requirement for complex stimulation techniques, such as hydraulic fracturing, as the formations permeability and porosity are high enough to allow sufficient volume of fluid migration through the field to the wellbore. With the advancement of horizontal drilling and stimulation techniques, it has allowed for unconventional shale reservoirs to become a new staple of the petroleum and natural gas industry, as these were previously deemed to be unprofitable for development by using past techniques.

The inherent problems with shale deposits lies in their unique properties which associate some of their mechanical behavior more with that of coal bed formations than that of other more conventional reservoirs, or traps. Shale reservoirs allow for adsorption to occur through the bonding of entrained hydrocarbons throughout the rock matrix. This allows for additional hydrocarbon storage beyond that of the associated pore space volume available within the shale rock. The surrounding lithological stresses also play an important role in the physical behaviors related to shale reservoirs as it impacts the total compressibility. This is along the lines of shrinkage and swelling that is seen in coal bed formations which is dependent upon the in-situ and applied stress distributions. The permeability and porosity of the shale rock matrix varies directly with these applied stresses due to the compressibility and higher elastic limit, relative to other types of geological formations in conventional reservoir development. These characteristics affect the trans-missive ability of shale formations, influencing the fluid migration potential through a reduction in inherent permeability and natural fracture closure throughout the formation.

Hydraulic fracturing is a process that is used in order to stimulate both conventional and unconventional reservoirs in an effort to make them more economically feasible to develop, produce or remediate; both new and old fields alike. The process of hydraulic fracturing allows for access to vast amounts of previously inaccessible hydrocarbon deposits throughout a reservoir. This is achieved by generating a greater contact area between the producing formation and the wellbore. As a fracture propagates through the formation, reservoir to wellbore conductivity is increased by the drastic change to permeability throughout the stimulated zone. These fractures increase the fluid migration potential by significantly increasing permeability and therefore, the amount of production and recoverable hydrocarbons from the reservoir is drastically increased throughout these zones.

The process of hydraulic fracturing uses the injection of water or gel and a propping agent (i.e. sand) at high pressure into low permeability formations that do not allow sufficient fluid migration. This process first utilizes perforating guns to puncture the production tubing, cement and steel casing to initiate the location of fracture. These locations are then sealed off on an individual basis by the use of packers which allow for an increase of applied pressure that is isolated only to that specific zone of the wellbore and surrounding formation. The fracturing fluid, typically 99.5 percent water and sand is then pumped down the wellbore to the isolated perforations. As fluid pressures are suddenly increased at the injection site by the use of high pressure pumps, the surrounding stress regimes are affected. Once the applied fluid pressures meet or exceed the fracture initiation pressure of the formation then the crack, or fracture begins to develop. These stress fields continue to alter throughout the immediate and surrounding area as the fracture(s) propagate throughout the formation.

Fracture initiation and propagation is controlled by the relationship of applied pore pressure to the rocks tensile strength and overburden pressure. The propagation of the fracture is further controlled and directed by the orientation of the principal stresses at the immediate fracture tip. The direction of fracture propagation will continue perpendicular to the path of least resistance through the formation (i.e. the least principal normal stress). This implies that a fracture will propagate parallel to the maximum horizontal stress, such that closure and fracture width is related to the minimum horizontal stress.

Proppant within the fracturing fluid stabilizes the developing fracture as it propagates throughout the formation. The distribution of proppant within this developing fracture aids in preventing full aperture closure, providing support to the compressive forces trying to close the fracture. The use of proppant aids in extending both the length of fractures as well as stabilizing the newly created void space to the formations closure pressure. This allows the induced fracture network to maintain maximum conductivity from the producing formation to the wellbore once the treatment process has been completed, while also increasing the volume or surface area of augmented permeability. The types of proppant to be used vary depending upon the specific treatment plan that has been developed, however these are typically a mixture of multiple grades (or sizes) of sand or plastic beads that settle through the developing fracture. These methods of transport are dependent upon the injection pressure gradient and fluid-mass velocity through the fracture which generally cause larger particles to settle first and smaller particles to settle last.

As wellbore zones or stages are fractured throughout a reservoir, the in-situ stress fields are modified. The redistribution of these stress fields relies upon the in-situ conditions of the initial geological strata, rock matrix and induced hydraulic gradients through the propagating fracture network. This redistribution of these stress fields generates the possibility of reduced stability throughout the modified stress regime. This is suggesting that the natural faults and fractures may potentially reactivate within the affected treatment zone and/or surrounding reservoir area that has seen these stress influences. These new stress regimes can lead to a number of possible complications if instability occurs, most notably as felt seismic anomalies leading to fluid loss and reservoir or aquifer damage.

The seismicity induced by hydraulic fracturing is inherent to the process and has been a principal study of the process. These induced seismic events are typically used to map the generated fracture network, aiding in the optimization of the well completion and stage treatment design. As the fracture propagates through the rock matrix, energy is released in the form of vibrations. Monitoring these

vibrations indicates the path, geometry and distribution of fractures within the induced fracture network. These induced seismic events are typically on a micro-seismic scale which indicates that these events do not transmit enough energy to the surface to be harmful or felt. This is because the applied fluid energy is dissipated over a very large area. The occurrence of these micro-seismic events would therefore be expected to last throughout the duration of the treatment period, or until fracture development has subsided below the threshold of the seismic monitoring equipment.

In many instances however, field cases have revealed that the release of seismic energy continues well beyond the length of the injection period. At times, these secondary events are of a higher magnitude than those induced during staged treatments. These types of seismic events can be classified as seismic anomalies, as they are not directly attributed to the fluid injection and fracture propagation but instead to the redistributed stress fields that are developed by these events.

Induced seismic events and related anomalies that fall outside the expected fracture network give an indication to areas of possible fault slippage or reactivation. This is expected to occur along zones or areas of discontinuity, as the modified in-situ stress fields relax to a new equilibrium. These events, can at times help further increase conductivity to the wellbore along the fault faces and interconnecting fractures, increasing hydrocarbon production. In other cases, these seismic anomalies can be detrimental to the well as they are often times associated with hydraulic fracture fluid loss, reservoir or aquifer cap-rock damage and in extreme cases has the potential to damage surface infrastructure(s) through felt seismicity and associated subsidence.

There have been several cases of felt seismicity which possess the capability and have been shown to damage the reservoir or surrounding aquifers given the proper conditions. Although these cases are extremely rare, the possibility is an unacceptable consequence that requires a better understanding of the hydraulic fracturing process in order to diminish the probability of these related seismic anomalies. Typical seismic activity throughout the stimulation process tends to fall below a 1.0 magnitude; however in very rare cases the seismicity associated with hydraulic fracturing has been shown to reach magnitudes in excess of 3.0 (Ellsworth, 2013). In addition to the overall magnitude of the induced seismic anomalies, the frequency of these events occurring is also an extremely important factor. These seismic anomalies have been shown to directly correlate in areas that have been subjected to, or sustained multiple well and fracture treatments.

These types of seismic events can not only further discredit the fracturing process and industry as a whole from the public viewpoint, but it also affects the economic feasibility and recoverable hydrocarbons of the reservoir. In retrospect, these events can also further increase wellbore conductivity and thus surface production. Therefore, understanding these occurrences is an important objective of the industry and this research in order to diminish, predict and better understand the nature of these post-treatment seismic anomalies.

In comparison to the seismicity generated during fracture treatment, the additional or continuation of micro-seismic anomalies post-injection is evident from microseismic monitoring during the treatment process. The location of these seismic events places them a distance beyond that of their respective fracture half-lengths and localized seismicity that can be associated with the induced fracture. This offset distance of seismic activity is suggestive that natural faults, fractures or areas of discontinuity are being stimulated in addition to the intended pay zone where areas of localized seismicity can be seen. This confirms that stress fields are being modified far beyond that of the immediate area surrounding

the induced fracture network and outside the period of injection. The extent of these stress modifications depends upon the specific interaction of geological, thermal and fluid properties in the producing and surrounding formations as well as that of injection fluid. This often becomes an extremely difficult problem to not only measure, but to correlate to analytical and numerical methods of prediction and simulation due to the complicated coupling that occurs through these processes.

The most notable controlling factor in cases of fault reactivation had been shown to be the frictional coefficient that is present along the pre-existing fault and fracture plane(s). As the in-situ stress fields are modified through the induced fracture network and surrounding area, the friction between previously deactivated faults that lie in these altered stress zones may be affected. This can cause material failure or general instability throughout the area, leading to a displacement along the relative fault surfaces. This geological process is most often described by the Mohr-Coulomb Failure Criterion, which describes the principal stress relationship to a materials inherent properties in a straightforward manner by relating the shear and normal stresses along the acting plane. In their natural state, deactivated fault zones do not pose an issue. The confining pressure and past geological events have caused a resistance to sliding or slippage throughout these zones due to the current in-situ stress regimes, as they have been brought to equilibrium over time. With the introduction of fracture(s, discontinuity and pore pressure is increased throughout the induced fracture network as it propagates throughout the reservoir. The related stress changes can lead to a loss of friction as increases in the principal stresses or alterations to the entirety of these in-situ stress fields along these deactivated fault planes.

The process of hydraulic fracturing has become an increasingly complex procedure as it has become more widely used throughout the petroleum and natural gas industries. This has led to the development of new application methods due to industry advancements in horizontal drilling and stimulation techniques, as well as an increased understanding of the key principals involved with the hydraulic fracturing process. The impacts of hydraulic fracturing have been studied throughout its use; however their effects have only recently become readily apparent as it is being used with such an increased frequency. This influx of data has led to the realization that in some cases, what was once merely seen as a coincidental occurrence may be in direct relation to the stimulation techniques used for fracture treatments. The relative natures of these impacts that may be associated with hydraulic fracturing are becoming apparent due to statistical probability of their recent, widespread use.

The delicate nature of this subject, with relation to both the energy industry and environmental concerns has caused it to become a trending sociopolitical topic throughout not only the United States, but throughout the globe. The increased scrutiny that has been brought about from both the public viewpoint and government agencies alike has caused the industry to take notice in an effort to better understand the process of hydraulic fracturing and its related effects. The expansion of research related to this topic will ultimately benefit all parties involved as it is a necessary step in sustainable energy development both here in the United States and abroad.

The study of hydraulic fracturing has been done through a number of differing techniques in order to better understand the consequent alterations of in-situ stress properties and their relation to the associated interactions throughout porous media. Many of the studies within this field have not yet addressed several of the more complex issues involved with the hydraulic fracturing process. In order to study these complex interactions involved with stress induced fault reactivation, the progression

between pre and post-fracturing must be studied in great detail. The complexities surrounding cases of fault reactivation require consideration of the influential geological parameters, rock mechanics, fluid properties and dynamic stress interactions in an effort to understand, classify and predict the proper in-situ stress response and it's relating effects.

1.2. Objectives

The underlying goal of this project and the associated research is intended to investigate advanced methods to predict cases of fault reactivation and therefore improve the effectiveness of hydraulic fracturing treatment plans in horizontal shale gas wells. The research area will focus on the Marcellus shale formation and associated geology throughout the Appalachian Basin region.

The previous work done in this area has not fully related or addressed the complex interactions within the fracture network. Therefore these methods do not offer the desired capability or performance of predicting the pre and post fracturing effects, primarily relating to these modified stress fields. This is beneficial in preventing the reactivation of natural faults lying within these modified stress regimes as well as optimizing the overall design of fracturing stage treatments. Understanding these relationships can provide further insight to creating more effective stimulation plans. In addition, this research may be further applied to similar types of geological deformation problems and fault study investigations due to the close relationship(s) in methodology.

To develop a fundamental basis for characterization of geomechanical performance of shale gas reservoirs during the hydraulic fracturing process, four specific objectives are proposed:

(1) to assess the reactivation potentials of faults by identifying the in-situ stress conditions of faults nearby fracture treatment wells;

(2) develop a propagation model for multiple fractures simultaneously created;

(3) to extend current 2D stress model to characterize the stress state changes of a fault and near-fault zones, and predict fault slippage due to hydraulic fracturing;

(4) to optimize fracture design avoiding reactivation of faults.

In order to achieve these objectives, the following tasks and sub-tasks have been implemented and performed throughout the completion of the project:

- Assessing the reactivation potentials of faults by identifying the in-situ stress conditions of faults nearby fracture treatment wells.
    - Acquisition of data for horizontal shale gas reservoirs
    - Characterization of critically stressed faults
- Development of a 3-D propagation model for multiple transverse fractures created simultaneously in one fracturing stage.
    - Fracture deformation model
    - Fluid flow and leak-off model
    - Fracture tip advance criterion
    - Mass conservation equation
    - Discretization of fracture propagation model with triangle element

- Further extending the 2-D variation model of stress field distribution coupled with the 3-D fracturing propagation model in order to predict fracture geometry and varied stress throughout the stage.
    - Green's functions and displacement continuity method
    - Balance of stress and internal fluid pressure on fracture surfaces
    - Coupled 3-D model (stress variation versus fracture propagation)
    - Discretization of the coupled 3-D model
- Generate code for a 3-D numerical model so that different cases may be studied. These will be validated with synthetic examples to ensure proper modeling.
    - Programming a coupled 3-D model
    - Validation and modification of the coded model
    - Generation of a 3-D simulator for fracturing design
- Characterization of the stress state changes of a fault and near-fault zones, evaluate the potential of fault slippage due to hydraulic fracturing and optimization of fracture design.
    - Reveal changes of stress state of fault and/or near-fault zones during a fracture treatment.
    - Evaluate the potential of fault slippage
    - Optimization of the fracture design by use of the 3-D simulator

In order to test the validity of advanced technology, the Hardie area of Marcellus shale in the Appalachian Basin was selected as the study focus. The stratigraphy and geologic structure of the Hardie area has been characterized using well logs, core and seismic data using Petrel.

To characterize the change of the state of in-situ stress in reservoirs surrounding the treated well by hydraulic fracturing, a 3D geomechanical stress/displacement model was developed using finite element method. By considering poroelastic effects, it can identify potential stable and unstable areas on the plane of a fault, based on the distribution of shear and effective normal stresses following Mohr – Coulomb criterion. With this model, in-situ stress in magnitude as well as orientation can be described in a 3D domain, which can be used to investigate impacts of fracture locations on the state of stress along the fault plane and optimal conditions of fracturing operation in terms of spacing between stages, fracture orientation of the subsequent stage and fault stability.

A 3D fracturing propagation model is being developed using finite element method with elasto-brittle cohesive elements. It can be used to simulate the propagation of multiple fractures simultaneously created in multi-layer reservoirs. The dynamics of hydraulic-driven fractures and the state of stresses in the surrounding region can be described in a 3D domain.

1.3. Project Scope

The specific focus of this research has been to study the influence of hydraulic fracturing on the geomechanical properties and response of a reservoir throughout the fracturing process. This information is useful to determine the effect, or potential of fault reactivation caused by hydraulic fracture and the related stress field modifications that occur throughout a reservoir and its surrounding geology. In relation to this subject, there are numerous commercially available software models which possess the capability to model hydraulic fracturing treatment plans or stages. The downfall in many of

these programs or techniques however is that they do not address many of the more complex rock and fluid mechanics occurring throughout the reservoir or fracturing stage. In addition much of the previous study in these areas have focused primarily upon stresses surrounding the fracture for the determination of propagation criteria. In addition many techniques to date do not adopt a fully coupled solution and thus assume a pressure boundary solution or one way coupling that ignores rock deformation or displacement effect upon the fracture pressure.

The assumptions made through the previous examinations of the topic, raise question to the overall accuracy of these assumptions and thus their associated results. The primary focus of this research is to evaluate the more complex reservoir interactions that occur throughout the fracturing process, including many of these previously neglected parameters and mechanics.

The overall goal of addressing these complexities is to further enhance the development of a three-dimensional model to analyze reservoir stress interactions. This will aid in increasing the result quality related to the prediction of fault reactivation tendency. The previous models used in relation to this objective have addressed the basic mechanical interactions that occur within a reservoir. These solutions allows for a more general determination of stress distributions, both pre and post fracturing. In many cases, this is a satisfactory in creating an effective treatment plane but it does not provide the capability required in relation to specific stability issues.

In conjunction with the Mohr-Coulomb Failure Criterion, the slip tendency seen across the fault plane may be predicted by the results. The preliminary model referenced for this research addresses the reservoir as an isotropic, homogeneous elastic medium which disregards the poroelasticity and leak-off related effects. These assumptions present a number of possible adaptions that can be made in order to account for a larger amount of the effective variations on geological stresses. The proposed methods and theory relating to the material presented in this paper will aid in the development of an effective three-dimensional model, relating reservoir stress interactions throughout the time of the injection period.

A primary focus here is the inclusion of poroelastic effects into the three-dimensional model, also addressing the inclusion of a proper leak-off model. The underlying theory of the model is based upon the Finite Element Method. This will be used to account for each aspect of fracture propagation and their interaction with in-situ stresses, both within and surrounding the reservoir through the coupling of the associated governing equations. These aspects will require that the fluid flow within the fracture be modeled simultaneously with propagation in order to account for stress interactions that occur throughout the time that a stage or fracture is being stimulated. This dependency will require an adaptation in domain discretization by the use of a dynamic mesh structure. This allows the address of time dependent boundary conditions that are associated with a propagating fracture through porous media. The coupling of these parameters will allow for a more precise and in turn, realistic modeling of interactions throughout the induced fracture network. This will ideally create a greater correlation to the responses often seen in field related data.

The inclusion of these parameters will allow for better assumptions to be made through the fracture stage development. The increasing scrutiny in regard to hydraulic fracturing has created the need of a more thorough understanding of the process in an effort to reduce the possible negative impacts surrounding the use of hydraulic fracturing.

2. Methodology

2.1. Reservoir Assessment

The collected information on the Marcellus shale from the Hardie area includes well trajectories and logs for a total of 7 wells, core analysis data for 2 wells and a 3D seismic survey with 196 inlines and 377 crosslines. This information is used for input and verification of numerical models by extracting important information about the field data to set up and test simulation runs.

2.1.1. Well Information

The well information was provided by Range Resources regarding a total of five wells. Two of these horizontal, i.e., Hardie Unit 1H & 2H and three vertical wells, i.e., Hardie Unit #1, Indian Point #1 & #3. Indian point wells #1 and #3 are out of the seismic survey.

Details of information provided on the field are as follows:

Table 1 - List of Wells used for Marcellus Data Acquisition

Well Name	Hole Type	Well Type	Field (Township)	County	State
HARDIE UNIT #1	Vertical	Pilot	GREENE	GREENE	PA
HARDIE UNIT #1H	Horizontal	Gas	GREENE	GREENE	PA
HARDIE UNIT #2H	Horizontal	Gas	GREENE	GREENE	PA
HOWARD #1	Vertical	Pilot	MONOGAHELA	GREENE	PA
HOWARD #9H	Horizontal	Gas	MONOGAHELA	GREENE	PA
INDIAN POINT #1	Vertical	Pilot	GREENE	GREENE	PA
INDIAN POINT #3	Vertical	Pilot	GREENE	GREENE	PA

2.1.2. Core Data Information

Core data information includes mechanical test data of the field samples including mean stress, Young's modulus, Poisson ratio, shear modulus. In addition, petrophysical data has been provided including density, porosity, saturation of gas oil and water, permeability.

Table 2 - Core Data Information by Well

	HARDIE UNIT #1	HARDIE UNIT #1H	HARDIE UNIT #2H	HOWARD #1	HOWARD #9H	INDIAN POINT #1	INDIAN POINT #3
Core Data	Y			Y			
Well Deviation	Y	Y	Y	Y	Y	Y	Y
Regular Well Log	Y	Y		Y		Y	Y
Geomechanical Log		Y		Y			

Table 3 - Petrophysical Data included by Well

				LOGS															CORES - CUTTINGS											Studies	
Well Name	State	County	TD (MD)	Microsois	Deviation Survey	Mud log	Dipole Sonic	FMI	PEX/TripleCombo	ECS	Sonic	Rock Mechanic	Anistrophy Analysis	Fracade Advisor	Caliban	Shale Montage	CORE LAB SPECTRA SCAN	Tracer Survey	CORED	Cuttings Analyzed	Rock Eval./TOC	VIT. REF.	Desorption Adsorption	XRD	PET. ANALYSIS	Mechanical	Fracture Analysis	SEM	Thin Section	TerraTek Geomechanical and Wellbore Stability	GMI Geomechanical and Wellbore Stability
Hardie Unit #1	PA	Greene	8335	X		X		X	X	X	X	X	X		X	X			FHC		X	X	X	X	X	X	X	X	X	X	
Howard #1	PA	Greene	8250		X	X		X	X	X	X	X	X	X	X	X			SWC		X	X		X	X			X	X		
Howard #9H	PA	Greene	10645		X	X																									X
Indian Point Unit #1	PA	Greene	8135		X				X	X																					
Indian Point Unit #3	PA	Greene	8299		X				X																						

2.1.3. Seismic Survey

A 3D seismic survey grid has been provided by Range Resources covering Green County, PA.

2.1.4. Field Geomechanical Model

Study Area Selection

The Hardie area of Marcellus shale in the Appalachian Basin was selected as the study area to test and validate the techniques developed in this project. The data acquired from the Hardie area includes well trajectories and logs for 7 wells, core data for 2 wells and seismic survey data with 196 in-lines and 377 cross-lines. Two wells are not located within the seismic survey area. We have been characterizing the stratigraphic and geologic structure of the Hardie area with available data using Petrel (2012).

Stratigraphic Characteristics

Marcellus shale is the target formation of hydraulic fracturing treatments for economic production of gas. In our study, overlain and underlain formations from upper and middle Devonian are also included in characterization of the geomechanical model to cover an adequate interval possibly influenced by fracturing activities (Fig. 1). Stratigraphically, the Marcellus is the lowest unit of the Devonian age Hamilton group, and is divided into several sub-units. Although black shale is the dominant lithology, it also contains lighter shales and inter-beded limestone layers. The Marcellus formation is classified as the basal unit of the Hamilton group, lying beneath the Mahantango/Hamilton formation member of this group in Penn and Maryland. It can also lies disconformably beneath the Rhinestreet shale member of the West Falls formation. The Marcellus shale is typically found deposited on the limestone of the Onondaga formation, which extends down to the end of the Early Devonian period. The contact between them may be sharp, gradational or erosional.

The Onondaga limestone is a fine-grained limestone that distributes widely as the base and can be identified by its low gamma ray value sharply contrast to the overlying Marcellus shale. It is found that the Marcellus is typically deposited on the Onondaga and can be identified by a gamma ray value greater than 200 API and a bulk density less than 2.55 g/cc. The Marcellus contains one or more thin limestone beds including the Purcell limestone which distributes irregularly and has a thickness range from 0 to 50 feet. The Mahantango/Hamilton shale consists of laminated marine shale, siltstone, very fine sandstone and some limestone. It has a gamma ray value less than 200 API and a bulk density value greater than 2.55g/cc. The Tully limestone is a fine-grained limestone and can be defined by a gamma ray range from 30 -110 API. Upper Devonian shales include the Genesee formation which has a thickness

range from 10 -150 ft, the Middlesex shale of the Sonyea formation and the Rhinestreet shale of the West Falls formation. The Rhinestreet is laminated, low-permeability, organic-rich shale. The Rhinestreet thickness varies significantly across the basin, with a gamma ray value over 200 API and bulk density value over 2.55 (Milici and Swezey 2006, and Matthew 2009).

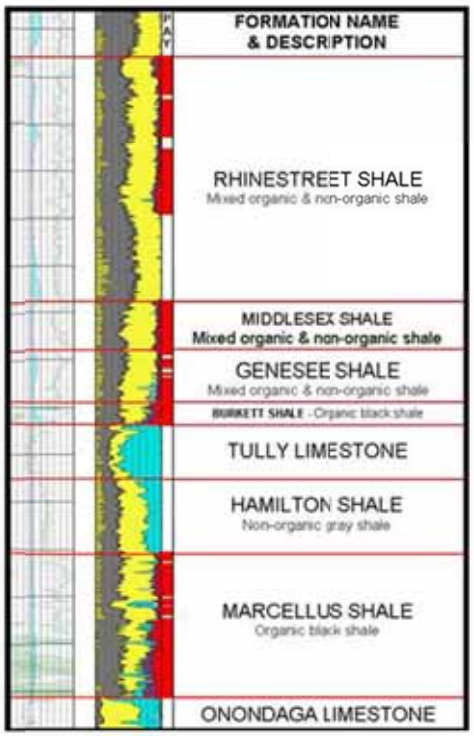

Figure 1 - Illustration of Stratigraphic Structure

Structural Model Construction

In the Hardie area, the stratigraphy is basically consistent with that described above and illustrated in Fig. 1, from well logs available in this study area. Four wells have proper gamma ray log data that can be used to pick up well tops. To identify horizons, a synthetic seismogram was produced based on the sonic log, density log and check shots, and manual adjustments were conducted to establish more accurate time-depth relation based on well tops recognized. The sonic log data from the well Hardie Unit 1 is relatively complete and was used to make the synthetic seismogram. For some intervals missing density log, sonic log is used to estimate density profile. If sonic log is also not complete, a cross-plot of bulk density versus gamma ray or sonic log versus gamma ray can be established and correlation can be used to estimate the missed parts of logs. For example, since the density log of Hardie Unit 1 starts from about 2000 ft, the gamma ray log was used to generate a cross-plot of density versus gamma ray as shown in Fig. 2. The correlation is shown in figure 2.

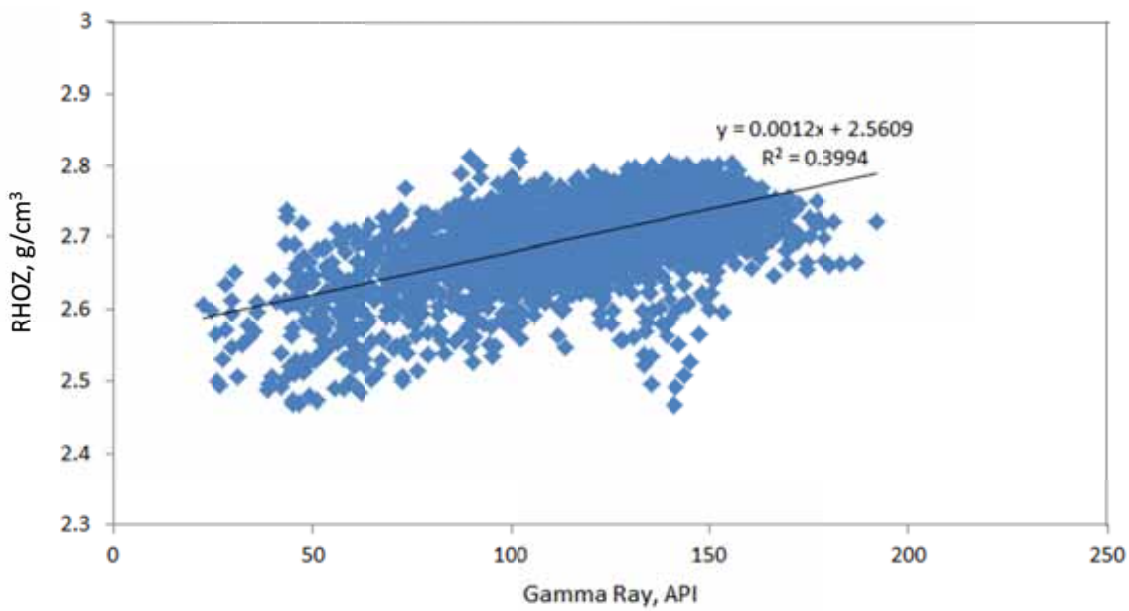

Figure 2 - Cross-Plot of Gamma Ray and Density

The synthetic wavelet like Ricker and wavelet extracted from seismic data around a borehole were used for generation of synthetic seismogram. Fig. 3 shows a comparison between the synthetic seismogram and real seismic traces of borehole side of Hardie Unit 1, along with identified well tops including Rhinestreet shale, Middlesex shale, Genesee shale, Burkett shale, Tully limestone, Hamilton shale, Marcellus shale and Onondaga limestone. As we can see, the amplitude responses on the synthetic seismogram are basically consistent with those on the seismic traces. Further adjustment in vertical position was made on the synthetic seismogram, which is shown in Fig. 4. The identified different horizons on seismic profile are illustrated in Fig.5.

The study area for construction of a structural model was determined primarily based on seismic survey boundary, as shown in Figs. 6 (a) & (b). There are two wells Indian Point 1 and Indian Point 3 located outside the seismic survey area. The boundary of the study area is defined by the green line while the boundary of the seismic survey is given in the pink line in Fig. 6 (b). A primary structure model of the study area was constructed and shown in Fig. 7.

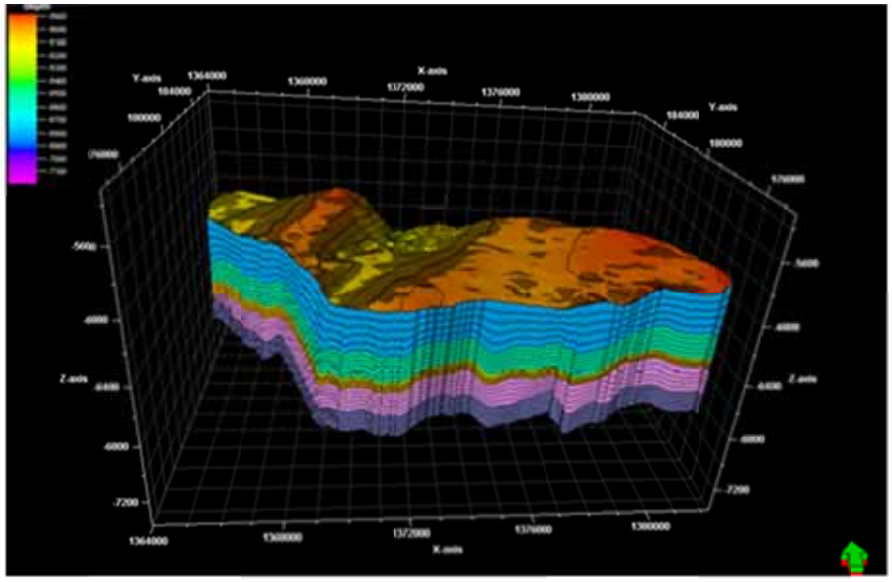

Figure 3 - Illustration of the structural model of the area of study

The ant tracking technique is used to identify faults from seismic data. There are two recognized main faults in this study area, as shown in Fig. 8. They may go up to the bottom of Rhinestreet shale, cross Marcellus shale, Hamilton shale, Tully limestone, Genessee shale and Middlesex shale and down to the top of Onondaga limestone. Fig. 9 gives an illustration of faults, well path and transparent stratigraphy in the structure model. Fig. 10 demonstrates the relative spatial position of the faults to different formation surfaces such as Middlesex shale and Onondaga limestone.

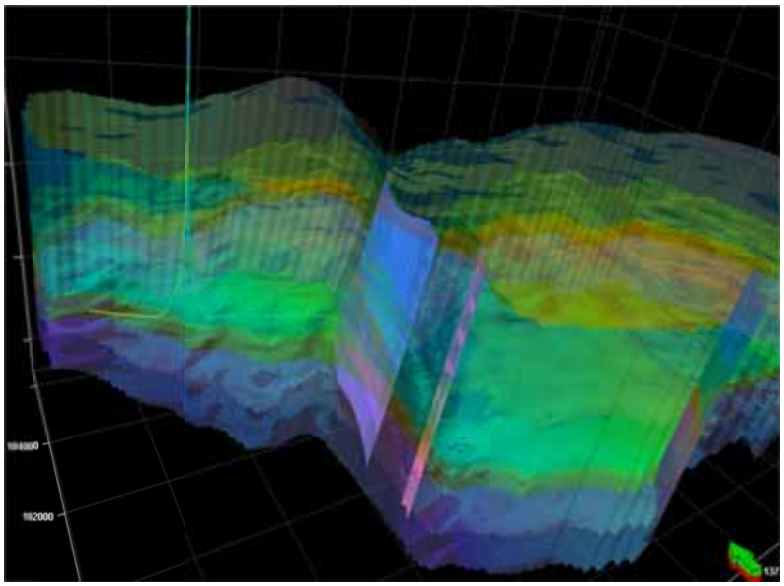

Figure 4 - Illustration of the fault location in the structural model

Then, Artificial Neural Network analysis is conducted using different seismic attributes as inputs and geomechanical properties including principle stresses, Young's modulus, Poisson ratio and tensile stress as targets. The Artificial Neural Network analysis model is first trained using half of the available geomechanical logging data and then 3-D geomechanical model is generated using the trained model.

The rest of the geomechanical logging is used for quality control, which is illustrated in Fig. 11. Different geomechanical properties on the Marcellus shale plane which has the same depth as the horizontal parts of the wells are shown in Fig.12 to 15. These 2D maps will be used in HFWVU-2D fracture propagation model to simulate single and multiple-fractures propagation in heterogeneous formation. Also, the 3-D view of Poisson ratio, Young's modulus and minimum horizontal stress of formations from the Middlesex shale to Marcellus shale are shown in Fig. 16 to 18. These models will be inputs for our HFWVU-3D to simulate single and multiple-fractures propagation in heterogeneous Marcellus shale formation.

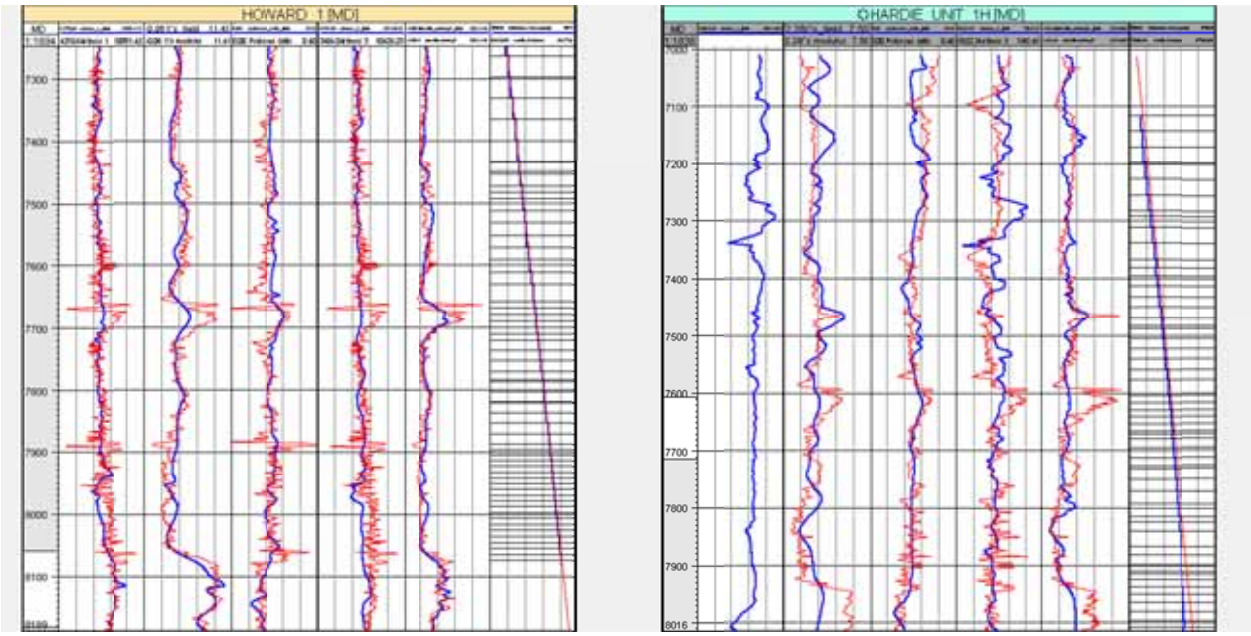

Figure 5 - Comparison of original log data and neural network analysis, from left to right, maximum horizontal stress, Young's modulus, Poisson's ratio, minimum horizontal stress, tensile stress and vertical stress (Red: original log; Blue: neural network)

2.2. 3D Geomechanical Model

2.2.1. Finite Element Model

In order to account for variations throughout the in-situ stress fields the mechanical deformation needs to be correlated to their associated stress fields, either naturally occurring or induced by the hydraulic fracturing process. This requires that the constitutive equations be determined for the descriptive physics of the mechanical problem to be solved.

Nonlinearity is often observed in structures due to stress-strain relations, large deformations, conditions of support, conditions of failure, or a combination of these causes. Nonlinear behavior is most often associated with cases of material behavior or conditions of support involving inelasticity (Nathan M. Newmark, 1971). In an effort to determine the trends in developing stress regimes, it is required that the problem be expanded to allow for time integration so that these dynamic relationships may be further understood and accounted for.

The 20-node brick element is also known as a quadratic (hexahedron) element, shown in **Figure 104**. The quadratic element is referenced from that the interpolation along each edge of the element is a

quadratic function. This allows them to simulate curved boundaries by a piecewise-quadratic approximation. The largest disadvantage of this type of element is during the mesh generation process as it requires more experience to properly design in order to reduce numerical difficulties, such as hour-glassing. It is noted however that if one of the faces of the 20-node brick element is collapsed then the element can simulate the singular strain and stress fields used in applications such as those of linear elastic fracture mechanics from (Dhondt, 2004).

The relationship of nodal points and elements is controlled through the constitutive equations of the defining problem. These are established through a series of independent, partial or fully coupled differential equations and associated boundary conditions. These differential equations establish the related physical relationship to the laws of conservation which control the behavior of many types of problems, such as: elastic, thermal and fluid flow.

In a reduced integration scheme, the next smallest available integration scheme is chosen. In this case, the reduced integration scheme for a 20-node hexahedral element is the same as that of a fully integrated 8-node element. This is represented by a 2 x 2 x 2 integration scheme. This provides the vertex nodal values in which the middle values of the element are obtained by taking the mean of the neighboring vertex nodal values. The process of reduced integration allows for a reduction in the number of unknowns which decreases the size of the linear system in order to increase the efficiency of the solution.

2.2.2. Governing Equations

The solution of the governing finite element equations will yield the displacements at each node. This may then be used to calculate the stresses and strains throughout the element and nodal matrices. Since the accuracy of the solution is greatest at the given integration points, the field variables are typically evaluated at these locations and then extrapolated to the surrounding nodes. This extrapolation is done on an element basis so that for any given node one obtains as many values as the number of elements it belongs to. This usually means that the values are discontinuous at the element border, however this is remedied by calculating the mean value over all elements that the node belongs to.

The specific application of the finite element method to discontinuity modeling is a particularly difficult task. Much of the difficulty in determining these solutions lies in the discretization of the continuum during stages of propagation as the elements are breached by discontinuity. This causes a special case of interpolating integration point values where discontinuity arises.

The mathematical model used here was derived based on the four basic principles: equation of stress equilibrium, continuity equation, Darcy's law and equation of state. The subsurface rock is considered as a porous medium that consists of rock matrix and pores/cracks filled with fluid. The pore fluid pressure can cause elastic deformation of rock and change of stress state to rock failure, while stress change can cause fluid flow. Therefore, the mechanical and hydrological behavior of the rock needs to be fully coupled to be evaluated correctly.

Equation of Stress Equilibrium

To represent the distribution of stress and strain, the equation of stress equilibrium – a governing partial differential equation in the displacement form is needed (Jaeger, Cook and Zimmerman, 2007). The hydro-mechanical behavior can be considered based on Biot's theory of poroelasticity.

$$G\nabla^2\boldsymbol{\delta} + \frac{G}{1-2\nu}\nabla(\nabla\cdot\boldsymbol{\delta}) + \alpha\nabla p + \rho\mathbf{F} = 0$$

*where G is the shear modulus, $\boldsymbol{\delta}$ is the displacement vector with three components (u, v, w), ν is Poisson's ratio, α is Biot's poroelastic constant (generally assumed as 1), p is the pore pressure, ρ is the bulk density and **F** is the body force vector per unit mass. ∇^2 is the Laplacian operator and ∇ is the gradient/divergence operator. With the strain-displacement relations*

$$\boldsymbol{\varepsilon} = \frac{1}{2}[\nabla\boldsymbol{\delta} + (\nabla\boldsymbol{\delta})^T]$$

and the stress-strain relations

$$\boldsymbol{\sigma} = \lambda trace(\boldsymbol{\varepsilon})\mathbf{I} + 2G\boldsymbol{\varepsilon}$$

strain and stress can be found once the displacement is solved. In Eqs 2 and 3, $\boldsymbol{\varepsilon}$ represents the strain matrix, $\nabla\boldsymbol{\delta}$ is the displacement gradient, *T* stands for the transpose of a matrix, $\boldsymbol{\sigma}$ is the stress matrix, λ is the Lamé parameter, **I** is the identity matrix and *G* is the shear modus.

Continuity Equation

It is a mathematical representation of the principle of mass conservation. Continuity equation of a fluid in a porous rock is given by

$$\nabla\cdot(\rho\mathbf{u}) = -\frac{\partial(\nabla\cdot\boldsymbol{\delta})}{\partial t} + \phi c_f\frac{\partial p}{\partial t}$$

The assumption related to Eq. 4 is that the density of the rock grains is constant (Chin, Raghavan and Thomas, 2000, Thomas, *et al.*, 2003). In the equation, **u** is the fluid velocity vector, c_f is the compressibility of the fluid in pores of rock and ϕ is the porosity.

Darcy's Law

The flow of a fluid through a porous medium is modeled by Darcy's law, which is an expression of conservation of momentum. It relates fluid velocity proportionally to the gradient of the potential.

$$\mathbf{u} = -\frac{k}{\mu}\nabla\Phi$$

where k is the permeability of a porous medium and μ is the fluid viscosity.

In Eq. 5, $\nabla\Phi$ is the gradient of flow potential defined as

$$\nabla\Phi = \nabla p + \rho g\nabla Z$$

where g is the gravitational acceleration and Z is elevation.

Equation of State

An equation of state presents a relation between properties of matters and a given set of physical conditions. In a porous medium, both pores and fluid are compressible. With the assumption of isothermal conditions, the compressibility of the pores is represented by the change in porosity with pressure,

$$c_p = \frac{1}{\phi}\frac{\partial \phi}{\partial p}$$

while the compressibility of the liquid is represented by the change in density with pressure

$$c_f = \frac{1}{\rho_l}\frac{\partial \rho_l}{\partial p}$$

where ρ_l is the liquid density. For gas, the real-gas law is used to model the behavior of the gas

$$\rho = \frac{pM}{zRT}$$

where M represents the molecular weight of the gas, z stands for the compressibility factor, R is referred to as universal gas constant and T is the reservoir temperature. The compressibility of the gas is given by

$$c_g = \frac{z}{p}\frac{\partial}{\partial p}\left(\frac{p}{z}\right)$$

Eq. 1 provides three governing equations, one for each of displacement components. The diffusion equation for pore fluid obtained by combination of continuity equation, Darcy's law and equation of state is accounted for another governing equation. The three displacement components and the pore pressure are taken as the four basic field unknowns of poroelasticity. This is a well-posed problem to solve.

The reservoir geometry is assumed a parallelepiped. The outer boundary conditions are given at a constant displacement for each of individual boundaries except the top. At the reservoir top, a constant overburden stress is used. The inner boundary condition is a constant net pressure applied along the hydraulic fractures.

A numerical model was established by discretization of partial differential equations over each element using the finite element method. With the Galerkin's method, the equation of stress equilibrium and the diffusion equation are discretized into a linear system of equation with unknowns of nodal displacement field and nodal pore pressure field. The displacement and pore pressure at an arbitrary point over an element are

$$\boldsymbol{\delta} = \sum_{i=1}^{n} N_i \boldsymbol{\delta}_i$$

$$\mathrm{p} = \sum_{i=1}^{n} N_i p_i$$

where N is the shape functions, $\boldsymbol{\delta}_i$ and p_i represent values at nodes, respectively. The discretized equations have the following forms,

$$[\mathbf{k}_s]\boldsymbol{\delta} + [\boldsymbol{c}_s]p = \mathbf{r}_s$$

$$[\mathbf{k}_p]\dot{\boldsymbol{\delta}} + [\mathbf{b}]\dot{p} + [\boldsymbol{c}_p]p = \mathbf{r}_p$$

where $\boldsymbol{k_s}$ is a matrix related to rock elastic properties and shape functions; $\boldsymbol{c_s}$ and $\boldsymbol{k_p}$ are matrix dependent on shape functions; $\boldsymbol{c_p}$ and $\boldsymbol{b}$ are matrix related to properties of rock and reservoir fluid; $\boldsymbol{r_s}$ and $\boldsymbol{r_p}$ represent residual force vectors; $\dot{\boldsymbol{\delta}}$ is the partial derivative of the displacement with respect to time; and $\dot{p}$ is the partial derivative of the pore pressure with respect to time.

2.2.3. Validation

Validation was performed with the case of Rangely oil field, Colorado (Raleigh and Bredehoeft 1976, Zoback and Healy 1984). An experiment was conducted at this field from 1969 to 1974 to investigate the physical basis of earthquakes occurred during fluid injection in terms of in-situ stresses, rock/fault frictional strength and pore pressure, and to establish the relationship between fluid pressure and seismicity. The measured initial pore pressure is 2349 psi. Water was injected into the reservoir and earthquake activity was recorded by seismographs. The derived critical pore pressure for triggering seismicity is 3988 psi consistent with the recorded frequency of earthquake activity. There is an inferred strike-slip fault through the center of the field and the majority of recorded earthquakes occurred trending along (or parallel to) the mapped fault.

The measured data based on field tests and laboratory experiments were provided in the studies of Raleigh and Bredehoeft (1976) and Zoback and Healy (1984), including the principal stresses and initial pore pressure etc.

Table 4 - Data of stress field and fault of Rangely oil field

Overburden stress	**6192 psi**
Maximum horizontal stress	8555 psi
Minimum horizontal stress	4553 psi
Initial pore pressure	2349 psi
Critical pore pressure	3988 psi
Orientation of maximum horizontal stress	N80^{o}W
Orientation of minimum horizontal stress	N10^{o}E
Mapped strike of fault	N50^{o}E
Mapped dip of fault	80°NW

We constructed a 3D geomechanical model with dimensions of 2000 ft (length) by 2000 ft (width) by 1000 ft (height). The initial overburden stress, maximum horizontal stress and minimum horizontal stress were used to find pseudo displacements at boundaries under which the measured stress data can be matched by a 3D homogeneous but anisotropic stress field with no considering the change in gravity effects of rock solid and pore fluid.

Fig. 1 shows the schematic diagram of the reservoir configuration in which a fault strikes N50oE with the dip of 80°NW. The tetrahedral finite elements of discretized reservoir model are also displayed in Fig. 1. In the case with the assumption that there is no change in gravity effect in terms of rock solid and pore fluid within the model, the three principal stresses are uniformly distributed, as shown in Fig. 2 on arbitrarily selected principal planes. In an environment of the strike-slip fault, the maximum horizontal stress is the largest, the vertical stress is the intermediate, while the minimum horizontal stress is the least. The shear and normal stresses also exhibit homogeneous distributions along the fault plane as a

result of a homogeneous stress model. Using the critical pore pressure of 3988 psi (Table 1) required for triggering seismicity in Rangely oil field, the coefficient of friction representing frictional strength of the fault plane can be evaluated. This coefficient of friction for fault slip is obtained from the ratio of the shear stress to the effective normal stress, which has a value of 0.67 on the entire fault plane (Fig. 3). The computed coefficient of friction (0.67) from our model is consistent with the result from the study of Zoback and Healy (1984).

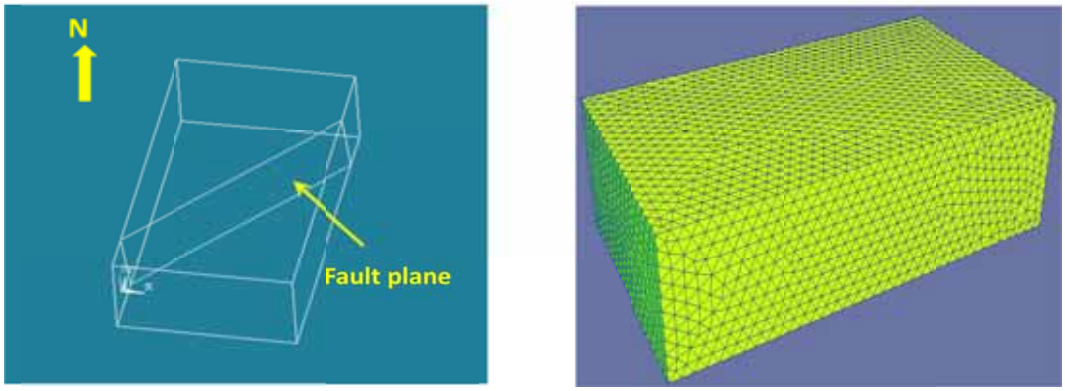

Figure 6 - Schematic diagram of the reservoir configuration and variational tetrahedral mesh

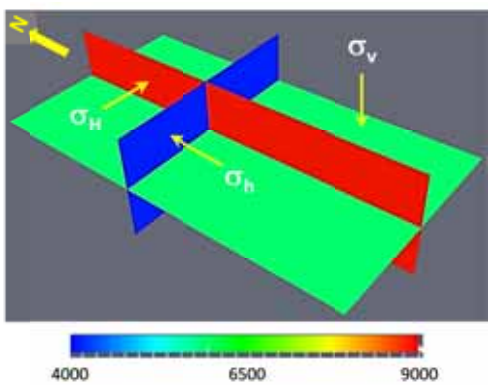

Figure 7 - Uniform distribution of three principal stresses (psi)

Our model can consider the change gravity effect and fluid pressure in pores, and generate a 3D heterogeneous stress field by applying the pseudo displacement boundary conditions.

To demonstrate the capacity of our model in handling 3D problems, the above case of Rangely oil field was extended with some practical consideration that gravity effect of rock solid and pore fluid changes with depth within the model. Note that the geomechanical properties of Young's modulus and Poisson's ratio and densities of rock solid and pore fluid are still all assumed constant within the model. As shown in Fig. 4, the resultant principal stress fields vary with depth.

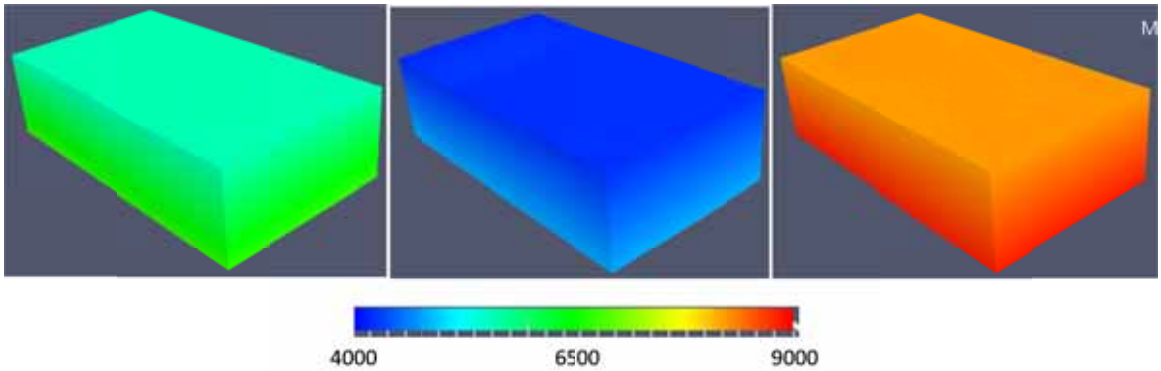

(a) Vertical stress (b) Min. horizontal stress (c) Max. horizontal stress

Figure 8 - Principal stress field (psi)

Similarly, there are variations along depth in the shear and normal stress fields on the fault plane, as indicated by Fig. 5. Associated with the dip angle of the fault and the relative magnitudes of three principal stresses, the shear stress component has slight changes with depth, while the normal stress component has relatively large changes.

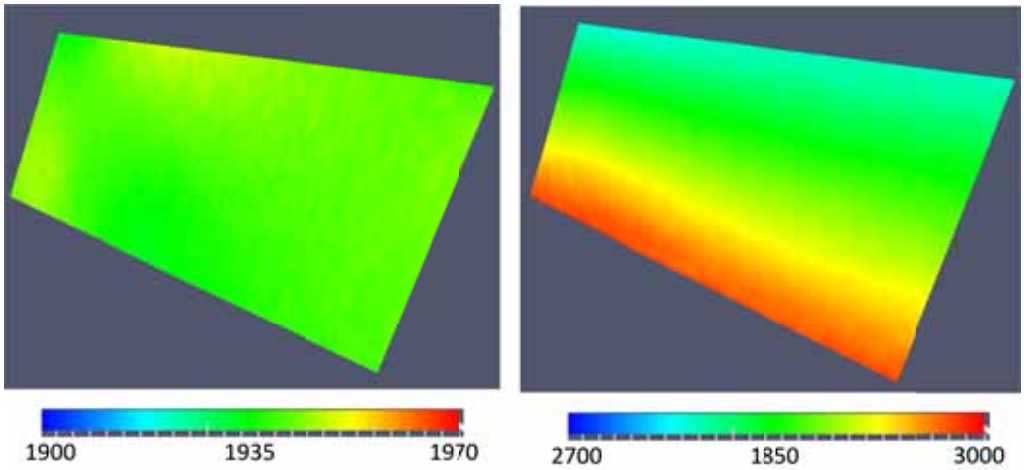

(a) Shear stress (b) Effective normal stress

Figure 9 - Stress distribution on the fault plane (psi)

The distribution of the computed ratio of the shear stress to the effective normal stress on the fault plane is demonstrated by Fig. 6. If we assume that the entire fault plane has the same frictional strength of 0.67, the stress state is at equilibrium of frictional failure when the ratio of the shear stress to the effective normal stress is equal to 0.67. Based on Mohr – Coulomb criterion, the areas with the ratio larger than 0.67 tend to be unstable with fault slip potentially being induced while the areas with the ratio less than 0.67 tend to be stable. At the depth around the center of the fault (Fig. 6), the ratio of the shear stress to the effective normal stress is approximately equal to 0.67 and thus the central zone of the fault is in a state of equilibrium of frictional failure. The upper portion of the fault, however, has relatively less stability because the ratio is larger than the frictional strength of 0.67. On the contrast, the lower portion of the fault is relatively more stable than the upper portion because the ratio is less

than the frictional strength of 0.67. Although the ratio of the shear stress to the effective normal stress is not strictly the same at the same depth due to numerical calculations related to tetrahedral meshing, the pattern of variational feature in this parameter is clearly captured.

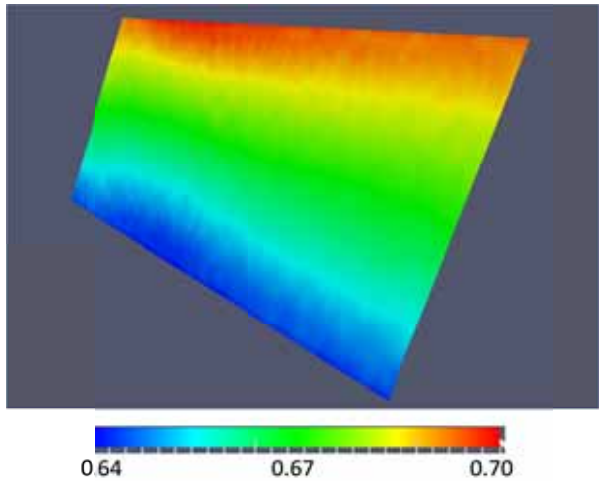

Figure 10 - Variation of the ratio of the shear stress to the effective normal stress on the fault plane

2.3. 2D Coupled Model

2.3.1. Finite Element Model

Hydraulic fracturing is a complicated coupled process, where fracture propagation in a solid medium is driven by pressurized fluid. Apart from natural occurrences such as magma-driven dikes, hydraulic fracturing is also applied as a technique in industry. The applications include underground storage of hazardous material, measurement of in situ stress, barrier walls for the prevention of containment from transporting, and heat production from geothermal reservoirs. However, one of the most important applications of hydraulic fracturing now is to improve the recovery of unconventional energy resource such as shale gas.

The complicated coupled process of hydraulic fracturing involves: (i) non-local relationship between fracture width and net pressure in the fracture; and (ii) non-linear dependence of fluid flow on fracture width and its linear dependence on pressure gradient. The coupled process is accompanied by leak-off, which is history-dependent, and fracture propagation, which gives rise to the continual configuration variation. These four behaviors lead to a variety of hydraulic fracturing propagation regimes, which depend on the material parameters of the solid, fluid, and the fracture configuration. Simplified hydraulic fracturing models have been developed, which can be used to study the influence of various material parameters. These models include the plane strain model, the PKN model, and the axis-symmetric penny-shaped model.

In the plane strain model, hydraulic fracturing propagation regimes are controlled by a time-independent parameter K_m, and a time-dependent parameter C_m under the assumption of linear elastic fracture mechanic (LEFM) for fracture propagation, lubrication theory for fluid flow, Carter's leak-off model, zero fluid flag between the fluid front and the fracture tip, constant injection rate, and uniform confining stress. Parameter K_m is used to distinguish the energy dissipation regime, and C_m is used to distinguish the storage regime of the injected fluid. Large K_m indicates that the energy dissipated in the viscous fluid is marginal compared to that dissipated by the extension of fracture, and the hydraulic

fracturing is referred to as toughness-dominated regime. For a viscosity-dominated regime, however, the K_m is small and the energy is mainly consumed by the viscous fluid flow. For a specific K_m, C_m always evolves from zero to infinity if it has a non-zero leak-off coefficient. In most applications of hydraulic fracturing, the fluid is expected to be mainly stored in the fracture, that means C_m is expected to be smaller than 1.0.

Great efforts have been made to obtain the asymptotic solutions for some regimes in the plane strain model. The key issue to construct the asymptotic solutions is to capture the correct tip behavior, as it controls the global response of the fluid-driven fracture and is regime-dependent. These asymptotic solutions are classified into the toughness-dominated ($K_m > 4$), the intermediate ($1 \leq K_m \leq 4$), and the viscosity-dominated ones ($K_m < 1$). These asymptotic solutions can be further classified according to C_m. The asymptotic solutions are regime-dependent, and they have good accuracy only if the material properties fall into their ranges. Although Spence and Sharp have proposed a regime-independent asymptotic solution for arbitrary K_m values, leak-off is not considered in their asymptotic solution, and fracture toughness is not prescribed as an input material parameter. A uniform framework that incorporates all the asymptotic solutions does not exist yet, although all the asymptotic solutions have the same theoretical basis and assumptions.

A possible way to investigate hydraulic fracturing propagation regimes in a uniform way is to use numerical methods. The common numerical method for hydraulic fracturing is the displacement discontinuity method, which is a variant of the boundary element method. Great efforts have been made to investigate hydraulic fracturing propagation regimes with finite element method in recent years, as the finite element method can overcome the limitations that are imposed on the boundary element method. Chen investigated the toughness-dominated and viscosity-dominated regimes with zero leak-off using finite element method. Similarly, Carrier and Granet investigated the toughness-dominated regime with small and large leak-off, and the viscosity-dominated regime with zero and large leak-off. The cohesive zone model rather than LEFM was used to simulate fracture propagation in their investigations. A key issue for cohesive zone model is that special technique is needed to ensure its numerical stability because of the negative tangential stiffness in the cohesive constitutive law. Based on LEFM, Lecampion applied the extended finite element method to investigate the hydraulic fracture problems, and proposed special functions to capture the tip asymptotes. Also based on LEFM, Hunsweck et al proposed a coupled finite element method and investigated the viscosity-dominated hydraulic fracturing propagation regime for impermeable elastic medium. Their work is based on the assumption that the fluid front never reaches the fracture tip. The purpose of the assumption is to avoid addition care to deal with the contact condition at the fracture tip.

In this paper, an alternative numerical method based on finite element method is proposed to uniformly investigate the hydraulic fracturing propagation regimes in the plane strain model based on LEFM. A distinctiveness of the proposed method is that no special attention is paid to the fracture tip behavior, even when the fluid front coincides with the fracture tip. In addition, a wide range of hydraulic fracturing propagation regimes can be uniformly investigated by the proposed method, which range from the toughness-dominated case to the viscosity-dominated case, and from zero leak-off examples for impermeable elastic medium to leak-off examples for permeable elastic medium.

The assumptions shared by the numerical method and the asymptotic solutions are LEFM, lubrication theory, Carter's leak-off model for fluid penetration into permeable solid medium from hydraulic

fracture, constant injection rate, and large enough confining stress that leads to zero fluid lag. Furthermore, the shear stress on the fracture surface is ignored, and the hydraulic fracture is assumed to propagate in the tensile mode and along a straight line that is perpendicular to the confining stress.

The rest of this paper is organized as follows: the theoretical model of hydraulic fracturing is presented in section 2. The hydraulic fracturing propagation regimes in the plane strain model, as well as some asymptotic solutions, are introduced in brief in section 3. The proposed numerical model is described in section 4. The uniform investigation is presented in section 5, as well as some discussions and comparisons of numerical results with asymptotic solutions. Some conclusions are made in section 6. It is worth pointing out that we would like to focus our attention on cases of which $0 \leq C_m \leq 1$, although the proposed regime-independent numerical model has no simplification or assumption related to C_m, and it is applicable to cases with any

2.3.2. Governing Equations

2.3.3. Validation

A plane strain model is shown in Fig. 6, with a fracture lying on the left bottom edge horizontally. The model is discretized with 2324 linear quad elements. Due to the symmetry, edge AB as shown in Fig. 6 is fixed for displacement in *x* direction, and edge CD except the fracture zone is fixed for displacement in *y* direction. The characteristics size of the elements on the first 15 meters of the left bottom edge is 0.05m. The initial half fracture length equals 0.05m, and there are 2523 nodes and 10331 degrees of freedom in the initial model. The initial uniform net pressure in the fracture is 0.1MPa.

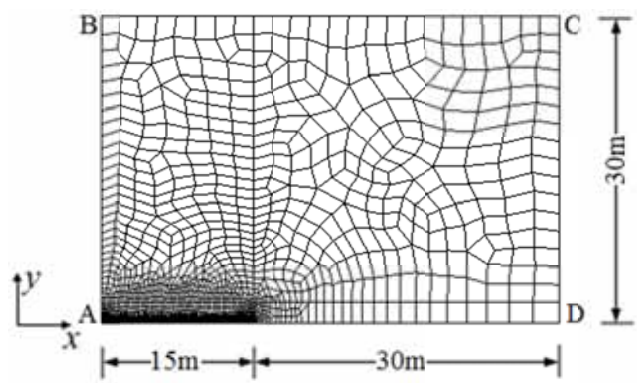

Figure 11 - Definition of the model

The investigation includes three cases covering the toughness-dominated, the intermediate, and the viscosity-dominated regimes. There are two examples in each case, one with zero leak-off and the other with non-zero leak-off. The parameters used in the investigation are listed in Table 1. For all the three non-zero leak-off examples C_m equals 1.00 at the moment of 67.83s. The numerical results and the asymptotic solutions in all three cases are plotted in Figs. 7-9, covering the net pressure at the inlet, the fracture width at the inlet, the half fracture length, and the width profile for a specified half fracture length.

Table 5 - Parameters for the simulations

Elastic modulus	E	18000MPa
Poisson' s ratio	ι	0.2
Injection rate	Q_0	0.001m^2/s
Dynamic viscosity	μ	7.98e-7KPa·s
Fracture toughness	K_{IC}	4MPa·m$^{1/2}$ (large toughness case, K_m =4.53) 1.77MPa·m$^{1/2}$(intermediate case, K_m =2.00) 0.25MPa·m$^{1/2}$(large viscosity case, K_m =0.28)
Leak-off coefficient	C_l	0.0(zero leak-off examples) 7.0e-5 m·s$^{1/2}$(non-zero leak-off examples)

(i) Toughness-dominated case

For the leak-off example, the injection efficiency equals 0.426 when C_m equals 1 in the numerical result, and it equals 0.406 when C_m equals 1 in the $K\tilde{K}$ edge solution. Fig. 7 illustrates the numerical results and the asymptotic solutions for the toughness-dominated case.

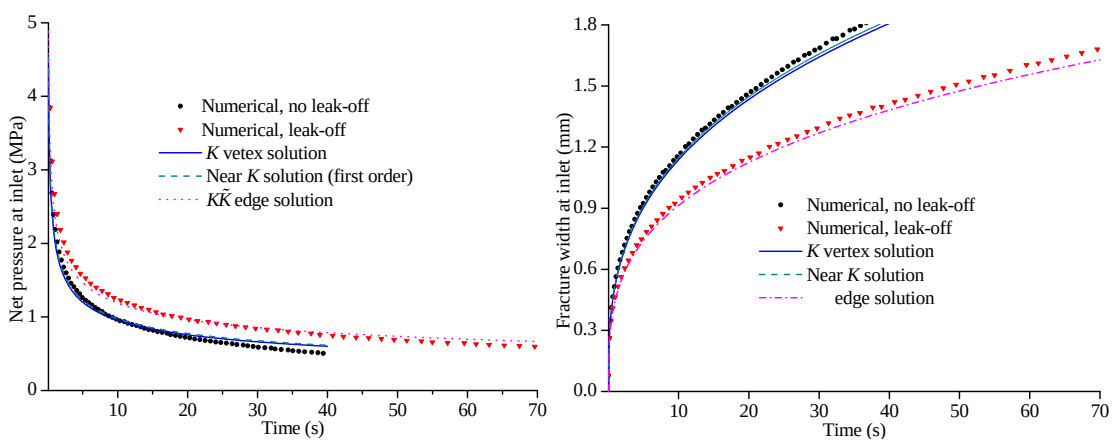

(a) (b)

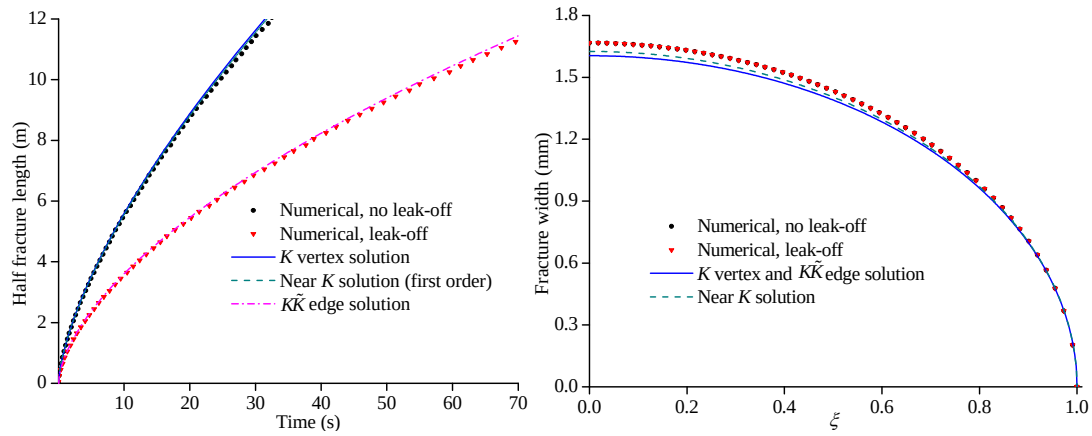

(c) (d)

Figure 12 - Fig. 7 Asymptotic and numerical solutions of net pressure at inlet (a), fracture width at inlet (b), half fracture length (c), and fracture width profile (lt = 11.1m) (d) for large toughness case

(ii) Intermediate case

For the leak-off example, the injection efficiency equals 0.294 when C_m equals 1 in the numerical result, and it equals 0.290 when C_m equals 1 in the intermediate solution. The numerical results and the asymptotic solutions for the intermediate case are plotted in Fig. 8.

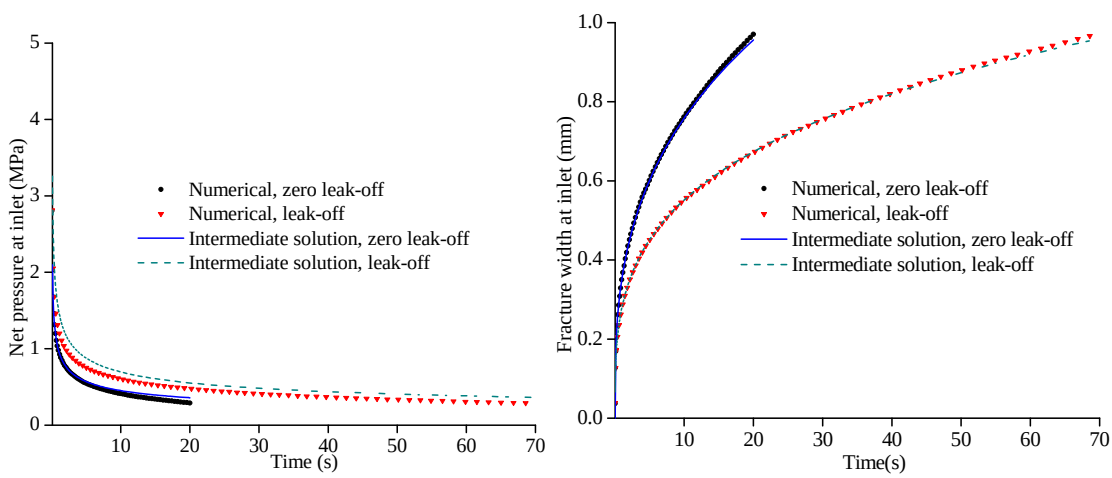

(a) (b)

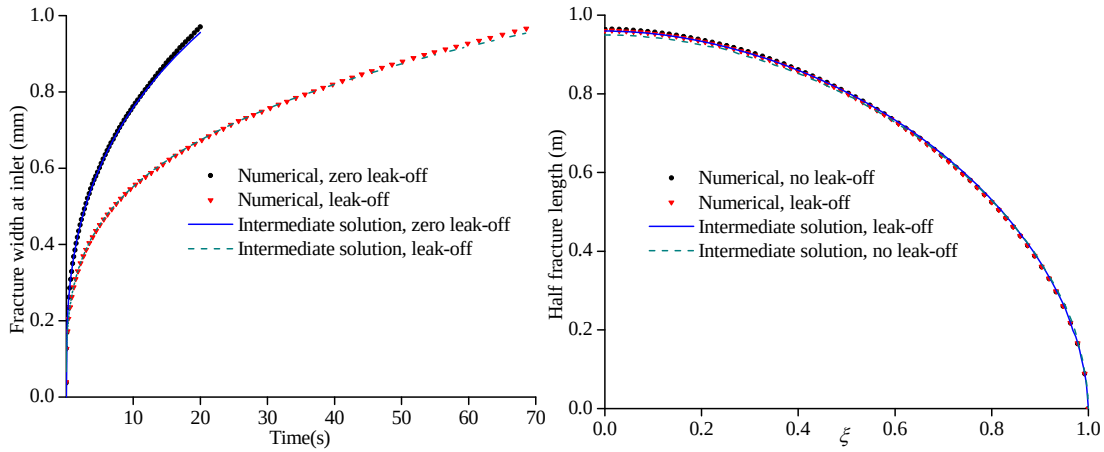

(c) (d)

Figure 13 - Asymptotic and numerical solutions of net pressure at inlet (a), fracture width at inlet (b), half fracture length (c), and fracture width profile (lt = 13.5m) (d) for intermediate case

(iii) Viscosity-dominated case

For the leak-off example, the injection efficiency equals 0.254 when C_m equals 1 in the numerical result, and it equals 0.249 when C_m equals 1 in the $M\widetilde{M}$ edge solution. Fig. 9 shows the numerical results and the asymptotic solutions for the viscosity-dominated case.

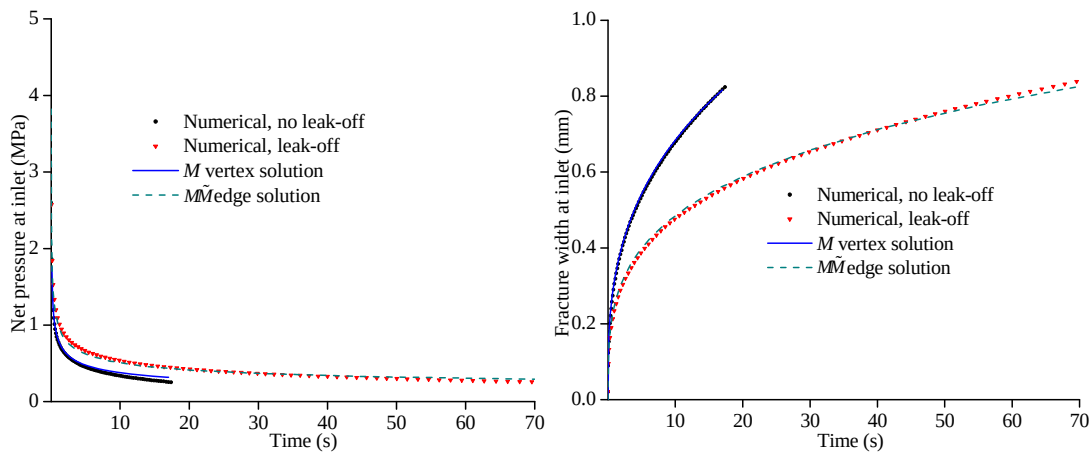

(a) (b)

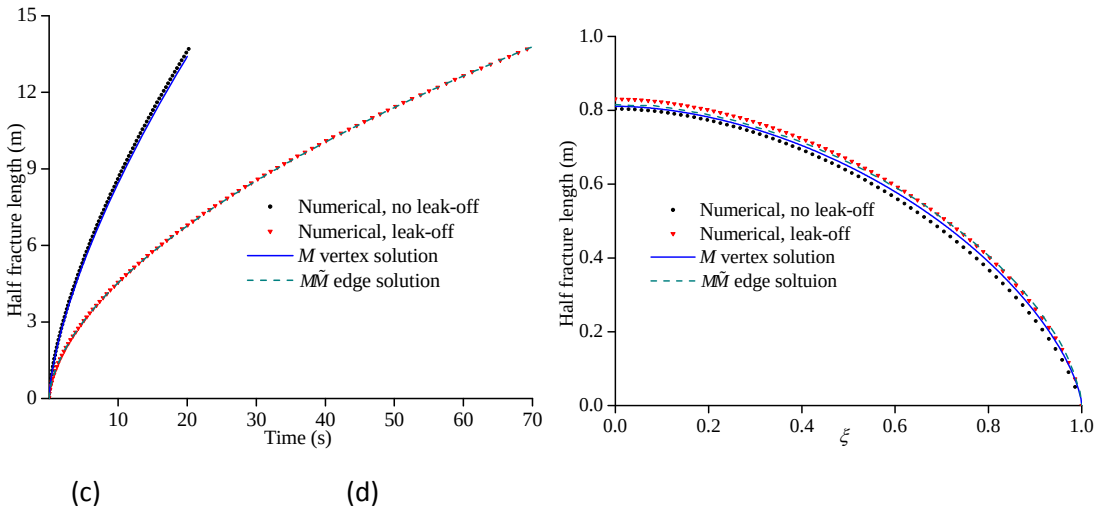

Figure 14 - Asymptotic and numerical solutions of net pressure at inlet (a), fracture width at inlet (b), half fracture length (c), and fracture width profile (lt = 14.2m) (d) for large viscosity case

Although it is shown in Figs. 7-9 that the gap between the numerical results and the asymptotic solutions on net pressure at inlet, fracture width at inlet, and fracture half length increases when the fracture propagates, it is clear that the numerical results have good agreements with asymptotic solutions in the six examples when the half fracture length is not longer than 15m. The validity of the proposed numerical method is verified. Apparently, the good agreement on fracture length and fracture width between the asymptotic solutions and the numerical results leads to the good agreement on injection efficiency, which can be seen in Fig. 10 for the example of intermediate case with leak-off.

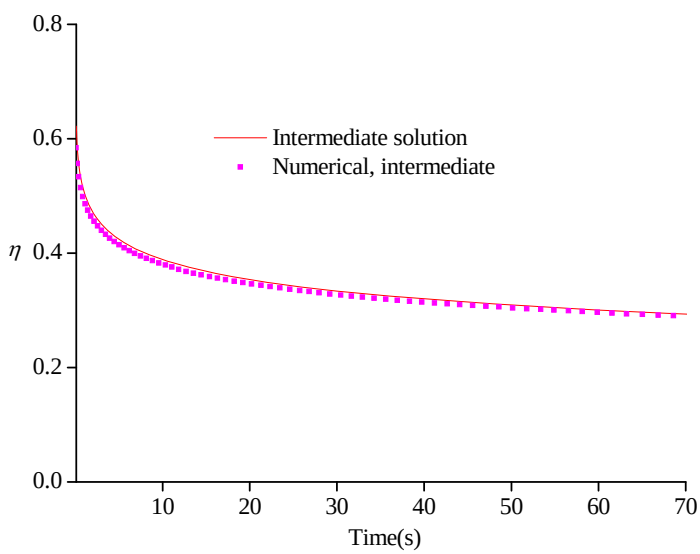

Figure 15 - Evolution of injection efficiency for the example of intermediate case with leak-off

Both numerical results and the asymptotic solutions in Figs. 7-9 show that for specific fracture half-length in each case, the fracture profile around the inlet in the leak-off example is slightly different from that of zero leak-off examples. It is shown in Figs 7-8 that when K_m is not smaller than 2.0, the tip behavior in the leak-off example is much similar to that in the example with zero leak-off. However, it is demonstrated by the numerical results and the asymptotic solutions in Fig. 9(d) that leak-off has non-

ignorable effect on tip behavior for the large viscosity case. This observation has good agreement with the tip behavior analysis.

The good approximation of the numerical result for the case with small K_m to the asymptotic solution for the case with zero K_m in Fig. 9 is also found elsewhere.

Some discussion

For a constant injection rate, hydraulic fracturing has the property of self-similarity when there is no leak-off. To study the self-similarity in the proposed numerical method, virtual net fluid pressure $\tilde{p}_{l_1}^{l_0}$ is defined in the following form as

$$\tilde{p}_{l_1}^{l_0}(\xi) = \frac{p_{l_0}(0)}{p_{l_1}(0)} p_{l_1}(\xi)$$

in which $P_{l_0}(0)$ and $P_{l_1}(0)$ are net fluid pressures at the inlet when l equals l0 and l1, respectively, and $P_{l_1}(\xi)$ is net fluid pressure at ξ when l equals l1. The net fluid pressure profiles $P_{4.0}(\xi)$ in the three examples with zero leak-off in the investigation sub-section are plotted in Fig. 11(a), including those obtained by the numerical method and by some of the asymptotic solutions. The virtual net fluid pressure profile $\tilde{P}_{4.0}^{8.0}(\xi)$ and net fluid pressure profile $P_{8.0}(\xi)$ obtained by the numerical method for the three examples with zero leak-off in the investigation sub-section are plotted in Fig. 11 (b).

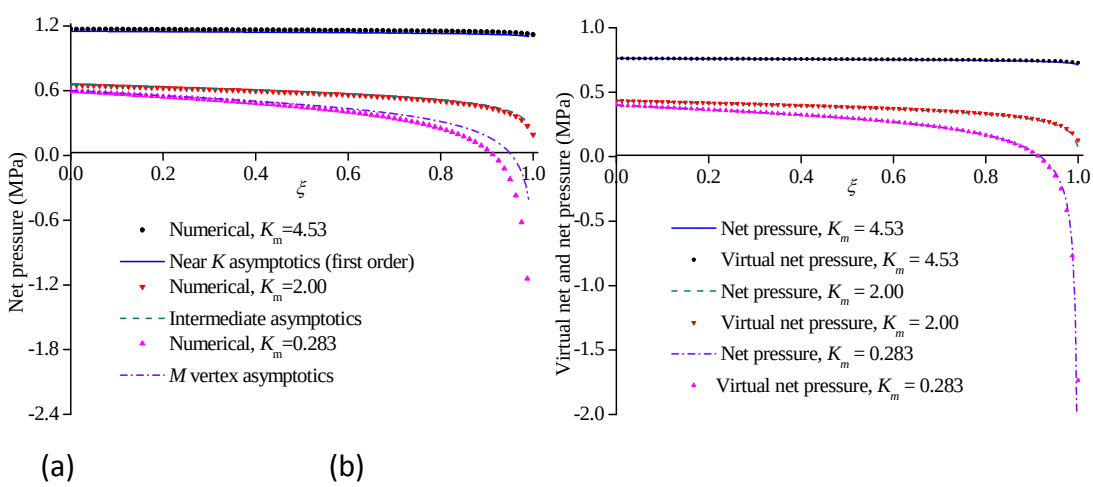

(a) (b)

Figure 16 - Net pressure profiles with l = 4m (a) and l = 8m (b), and virtual net pressure profiles with l0=8m and l1=4m (b)

It is worth pointing out that the net fluid pressure profiles obtained by the asymptotic solutions in Fig. 11(a) are truncated at $\xi = 0.99$ because of the net pressure singularity at the fracture tip. It is observed in Fig. 11(a) that the net pressure profiles obtained by the numerical method have excellent agreement with those obtained by the asymptotic solutions for the toughness-dominated and intermediate cases. Although in the viscosity-dominated case the net pressure profile obtained by the numerical method is slightly different from that by the asymptotic solution around zero net-pressure zone, the net pressure over there has limited contribution to fracture width and the overall numerical result matches well with the asymptotic solution as shown in Fig. 9. The good agreement between the net pressure profiles and

the virtual net pressure profiles shown in Fig. 11(b) means that the properties of self-similarity in hydraulic fracturing is well reflected by the numerical method.

Although the asymptotic solutions and numerical method share the same theoretical background, the domain in the asymptotic is infinite, and the domain in the numerical method is finite. Two additional numerical models are used here to study the dependence of numerical results on domain size. The edge lengths of the square domains in the two numerical models are 120m and 240m, respectively. The elements in the investigation sub-section can be treated as a set of the elements in the two numerical models. The characteristics size of the other elements in the two models is 3.5m. Like the model in the investigation sub-section, the left edges of the two models are fixed in *e* direction, and the bottom edges except the fracture zone are fixed in *y* direction. There are also six examples in each model, which have the same material parameters and initial conditions with the examples in the investigation sub-section.

For the two square models and the rectangular model in the investigation sub-section, some numerical results of the examples of large toughness and zero leak-off are plotted in Fig. 12, as well as the near *K* asymptotic solution. It is seen in Fig.12 that on the beginning the numerical results have no big difference from each other and they are very close to the analytical solution. The reason is that on the early time the fracture is short, and the domain effect is limited. However, when the injection time is larger than 20 seconds, the effect of domain size gets apparent, and the numerical results of the two square models get improved compared with those of the model in the investigation sub-section. Similar improvements are also observed in other examples of the two models. These improvements indicate that domain difference is an import source that contributes to the gap between the asymptotic solutions and the numerical results as shown in Fig. 7-9.

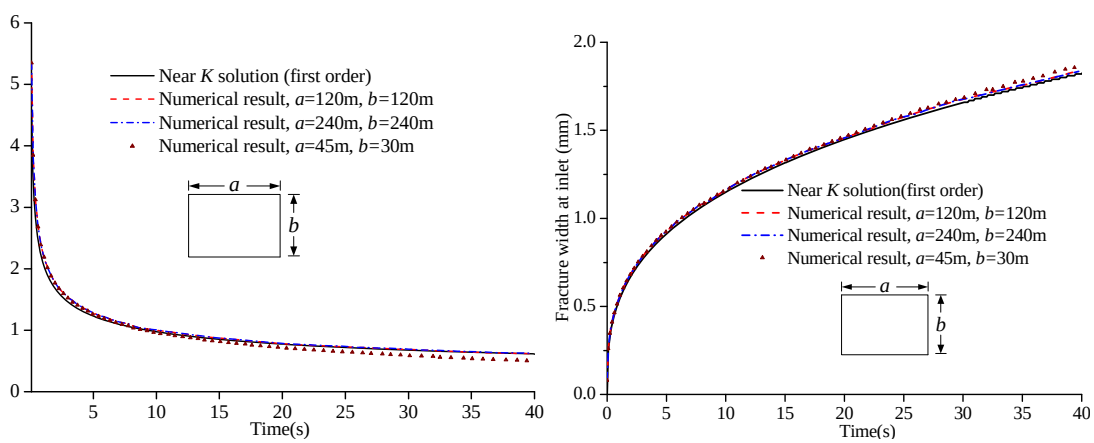

(a) (b)

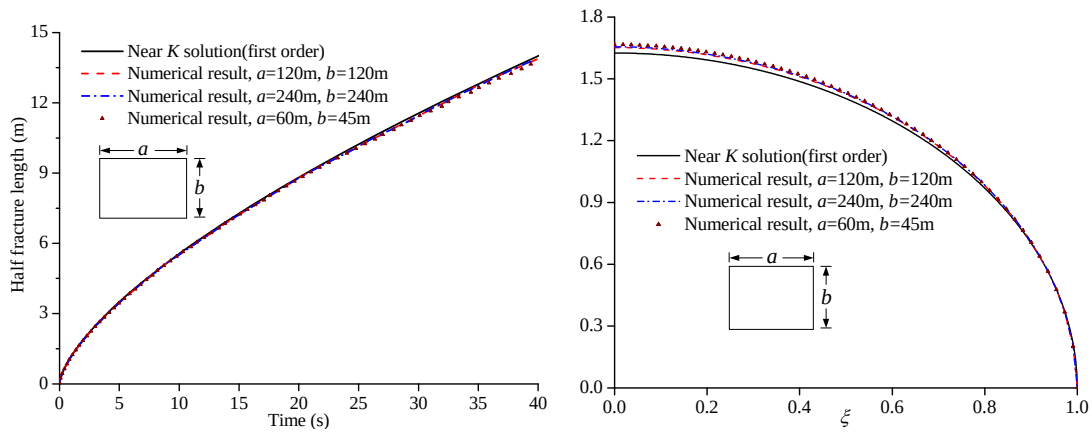

(c) (d)

Figure 17 - Asymptotic and numerical solutions of net pressure at inlet (a), fracture width at inlet (b), half fracture length (c), and fracture width profile (lt = 11.1m) (d) of the examples with large toughness and zero leak-off

It is seen in Fig. 11 that the fracture tip gets more singular with decreasing K_m. This indicates that the examples in the large viscosity case is harder to get convergent than those in other cases. The number of iteration needed to solve the non-linear coupled Eqs. (19) and (28) in the large viscosity examples of the square models are plotted in Fig. 13 for the first 100 steps. It is seen in Fig. 11 that in most steps the solution gets convergent within ten iterations. This phenomenon is also found in all other examples, including those in the investigation sub-section. This means that the proposed method has good robustness.

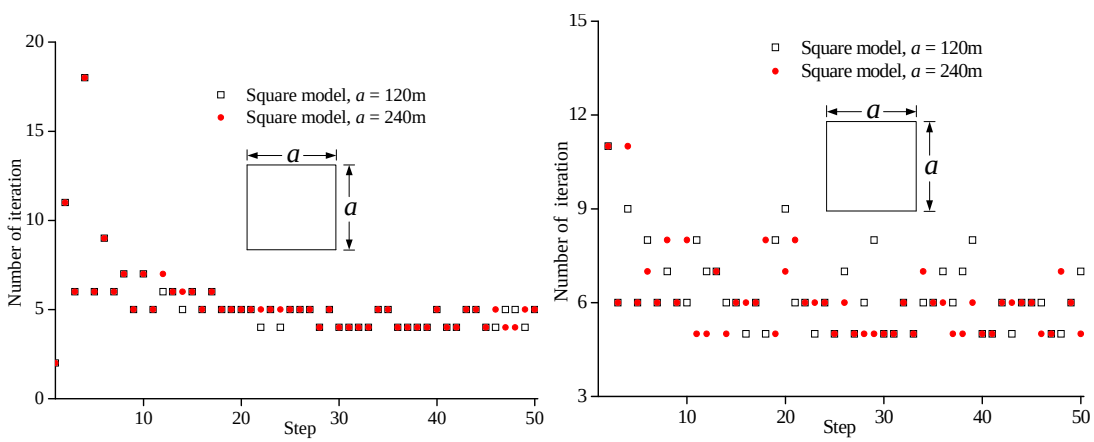

(a) (b)

Figure 18 - Number of iteration in the first 100 steps of the large viscosity examples in the square models: (a) examples without leak-off; (b) examples with leak-off.

2.4. 3D Coupled Model

2.4.1. Finite Element Model

The cohesive zone model is an approach to idealize the Mode I type of fracture opening for three dimensional analysis, neglecting in-plane and out-of-plane shear. This approach identifies a prospective fracture path prior to injection, along which the fracture is expected to propagate. This area is subject to local mesh or grid refinement in order to correctly map the large fluctuations that occur near the area of injection and surrounding the fracture tip. The propagation and further geometry of the fracture is then controlled by the geological properties, resistance to fracture and the hydraulic injection properties.

The cohesive zone model in three dimensions essentially states an initial 2-D fracture plane within the 3-D model. This is known as a zero thickness element which can be implemented to the classic finite element framework. This cohesive zone is prescribed as having zero width between the surrounding solid elements comprising the mesh. As pressure is applied to the injection point then this 2-D plane will begin to separate, thus expanding to 3-D if the conditions for propagation are met. This process is continued for each solution time step until either a prescribed time or the end of propagation by encroaching upon the domain boundary.

The structure of the 2-D finite element code remains relatively intact with the use of the cohesive zone model. The main difference is the element discretization, using an 8 node solid element and a 4 node hydraulic element.

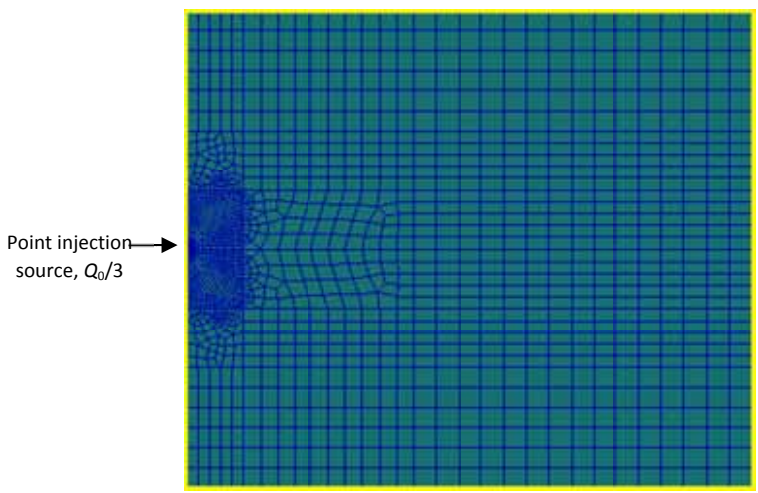

Figure 19 Cohesive Element Fracture Plane

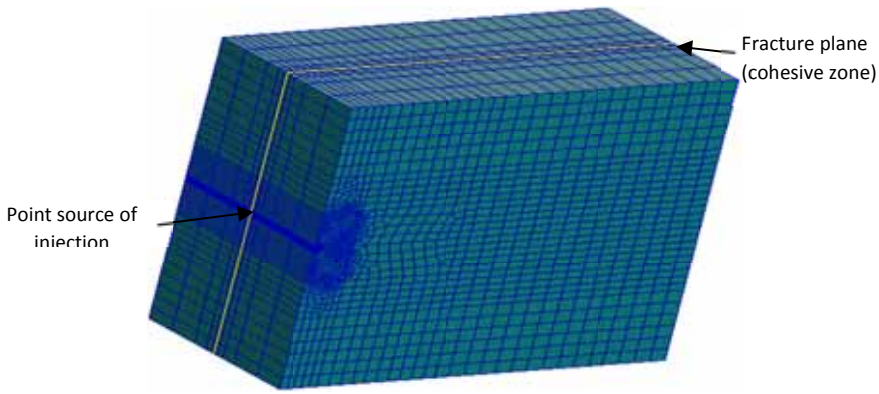

Figure 20 Three Dimensional Cohesive Zone Model Discretization for a Single Fracture

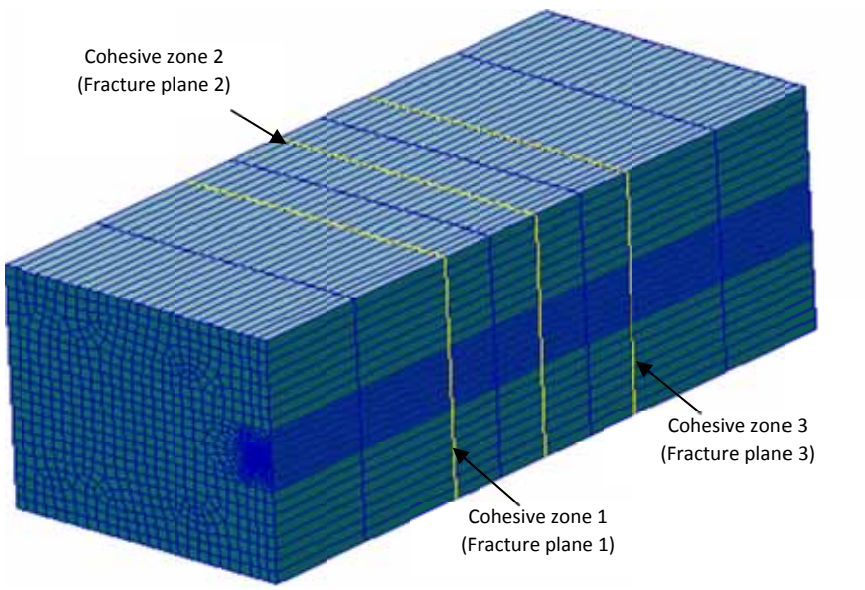

Figure 21 Thee Dimensional Cohesive Zone Model Discretization for Multiple Fractures

2.4.2. Governing Equations

2.4.3. Validation

Table 6 - Parameters for the cohesive zone simulation verifications

Elastic modulus	E	30GPa
Poisson' s ratio	υ	0.2
fracture energy	Gc	104Pa m
Fracture toughness	K_{IC}	1800 KPa·m$^{0.5}$
Tensile strength	f_t	3500KPa
Injection rate	Q_0	0.001m^3/(m·s)
Fluid viscosity	μ	0.000001Pa s
Initial fracture length	l_0	0.05m
Initial fluid pressure	p_0	300 KPa

Simulation results & verification

(i) Fluid pressure and fracture width at the injection points, and fracture length

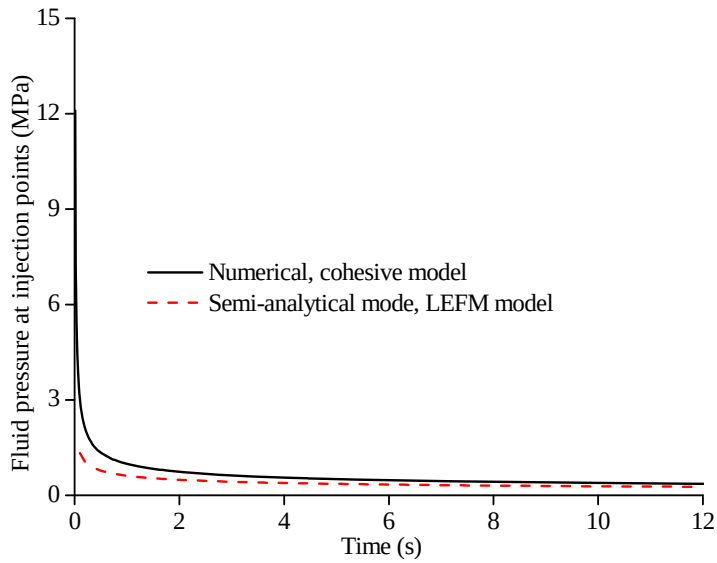

(a) Fluid pressure at the injection points

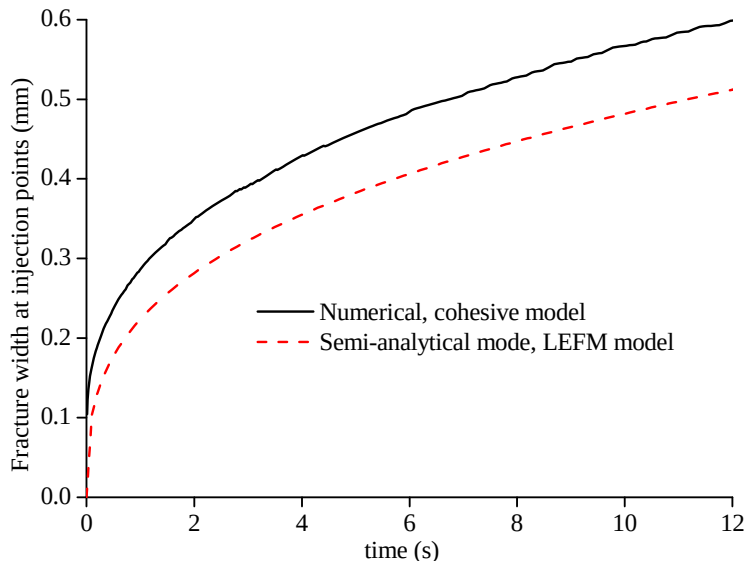

(b) Fracture width at the injection points

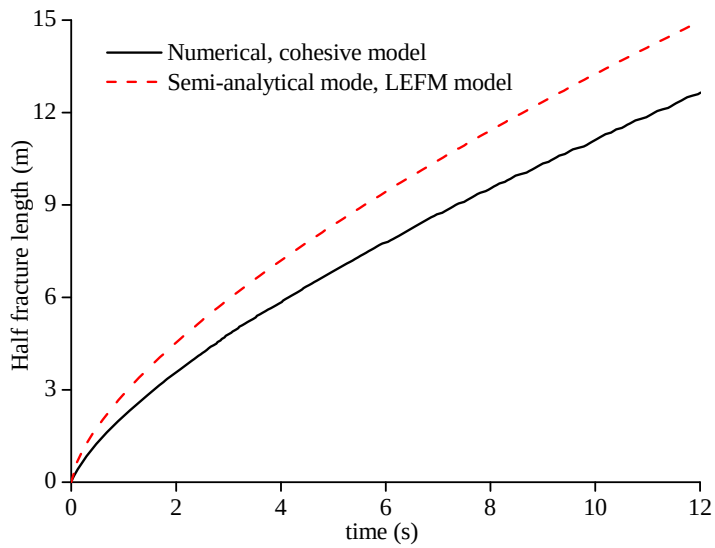

(c) Fracture length

Figure 22 - Numerical results for the CZ Model and semi-analytical solution for the LEFM model.

AS CZ model is always more flexible than the LEFM model, so the fracture width obtained by CZ model is wider than that by the LEFM model, as can be seen in Fig. 2(c). The wider fracture width in CZ model leads to its shorter fracture length as shown in Fig. 1(b). This shorter and wider fracture obtained by CZ model is also found in the literature [3]. The CZ model-based mode is verified. To appraise effect of hydraulic fracturing on the possibility of fault reactivation, the key parameter is the net pressure on the fracture surface. It is seen Fig. 1(c) that the net pressure obtained by the CZ model has good agreement with that by the LEFM model.

2.5. Fault Reactivation Assessment

A 3D numerical model was developed using the finite element method. It can be used to describe the change of the principal stresses in magnitude and orientation in 3D space potentially influenced by hydraulic fracturing, which would provide important information for design of an optimal azimuth of the horizontal lateral to be drilled and adequate perforation cluster spacing. Multiple fractures simultaneously created at one single stage can be considered and stress disturbance can be assessed. The fault intersecting the reservoirs is included and the state of stress along the fault plane can be identified based on the ratio of shear stress to effective normal stress following Mohr – Coulomb criterion.

The coulomb failure criterion was used in order to describe the slip tendency of the given fault plane or stress state. These stresses, taken from the finite element stress tensors evaluate their ratio to a generalized failure criterion.

The general approach of Coulomb Failure Criterion is shown below.

$$\tau > \tau_f = S_0 + \mu\sigma_n$$

Where τ_f, a failure criterion is set by a maximum shear stress limit and τ is the measured or calculated shear stress. Therefore, σ_n is the stress normal to the plane and μ is the resistive or frictional coefficient.

The Anderson fault theory is used to determine the principal stress relationships, representative of each type of faulting (i.e. possible reactivation).

$$Normal\ Faulting \qquad \frac{\sigma_1}{\sigma_3} = \frac{S_v - P_p}{S_{h\,min} - P_p} \leq \left[(\mu^2 + 1)^{\frac{1}{2}} + \mu\right]^2$$

$$Strike - Slip\ Faulting \qquad \frac{\sigma_1}{\sigma_3} = \frac{S_{h\,max} - P_p}{S_{h\,min} - P_p} \leq \left[(\mu^2 + 1)^{\frac{1}{2}} + \mu\right]^2$$

$$Reverse\ Faulting \qquad \frac{\sigma_1}{\sigma_3} = \frac{S_{h\,max} - P_p}{S_v - P_p} \leq \left[(\mu^2 + 1)^{\frac{1}{2}} + \mu\right]^2$$

2.5.1. Slip-tendency of faults

Geological discontinuities such as faults are inherent in most of the petroleum-bearing formations. Frictional sliding of the faults, therefore, can be expected to occur on a fault plane when the shear stress is sufficient to overcome resistance to sliding. This relationship is known as the Coulomb criterion (Jaeger et al. 2007).

$$\tau = S_0 + \mu\sigma_n$$

where S_0 is known as the cohesion (strength on pre-existing faults due to a healing mechanism), τ is the shear stress along the fault plane, σ_n the effective normal stress, defined as (S_n - P_p), and μ is a material property, called the coefficient of static friction. S_n is the normal stress on the plane, P_p is the pore-pressure, a compression positive sign convention is adopted here. Since poroelastic effects are not considered, we use σ (σ_1, σ_2, σ_3, σ_n etc.) to represent the total stresses in the following contents.

The shear and normal stresses that act on a fault plane are functions of the fault orientation with respect to the horizontal plane and can be shown as follow:

$$\sigma_{n(\beta)} = \frac{1}{2}(\sigma_1 + \sigma_3) + \frac{1}{2}(\sigma_1 - \sigma_3)cos2\beta$$

$$\tau_{(\beta)} = \frac{1}{2}(\sigma_1 - \sigma_3)sin2\beta$$

where β is the angle between the normal direction of the fault plane and the first principal direction. To calculate shear and normal stress on an arbitrarily oriented plane in three dimensions, please refer to Zoback (2007). It should be noted that the calculated slip-tendency for arbitrarily oriented fault planes in 3D is less than that obtained for fault plane parallel to the intermediate principal stress.

We are using the slip tendency (T_s) as a criterion to evaluate the stability states of faults before and during hydraulic fracturing operations. The calculation of the slip tendency is derived from the following procedures.

The slip tendency (T_s) along an arbitrarily oriented plane at an angle β to the first principal stress is defined as (Morris et al. 1996):

$$T_s = \frac{\tau_{(\beta)} - S_0}{\sigma_{n(\beta)}}$$

The fact that the stress state in many reservoirs is controlled by the frictional strength of optimally oriented faults indicates that the faults are under a critically stressed state (Zoback 2007). For any given stress state, the slip tendency and the orientation of the corresponding sliding plane are functions of the maximum and minimum principal stresses. The calculated slip tendency can be compared then with the coefficient of friction of the fault in order to quantify the stability state of the fault. When performing hydraulic stimulation, the underground stress field will be altered due to the creation of fractures; so is the slip tendency. We compare the slip tendency calculated before and during hydraulic fracturing stimulation in order to evaluate whether the fault would become more stable or would be activated.

It should be mentioned that only compressional shear failure along faults is considered and the cohesion of faults is assumed to be zero. These assumptions were used by investigators to study the reactivation of faults with widely ranging orientations with respect to the direction of maximum principal stress (Sibson 1985, 1990; Hill and Thatcher 1992; Stein et al. 1992). The combined shear and tensile failure is a complex process due to the angular relation of a fault plane with respect to stress field and because of the possibility of initiating shear or tensile failure in rock matrix before failure conditions are attained in the plane of weakness (Fournier 1996). Failures in extensional field require very small shear stresses, lower than those that prevail within the uppermost crust (Fournier 1996; Streit 1999). Fournier (1996) discussed this problem in great detail. In recent US development of unconventional shale reservoir, sub vertical and open-model fractures are frequently observed in outcrop (Gale et al. 2014). Under moderate to deep burial conditions, many natural fractures are lined or sealed with mineral cement over geological time scales (Laubach 2003). In Barnett shale, it is considered that the tensile strength of the contact between the cement and shale wall is low, which is manifested by commonly observed core-handling damage of sealed fractures (Laubach 2003; Gale et al. 2007).

Reservoir formations contain widely distributed faults, fractures, and other planar discontinuities at many different scales and orientations, therefore it is critical to find the surface with a maximum value of slip tendency among all potential slip surfaces. In other words, we assume all planar discontinuities are equally weak, distributed randomly in all directions and are in a critically stressed state under initial conditions, then the maximum value of slip tendency calculated. Should be equal to coefficient of friction of the discontinuities (faults, fractures, etc.). This assumption was proposed and discussed in great detail in Townend and Zoback (2000) and Zoback (2007). During hydraulic fracturing stimulation, the stress field around the hydraulic fracture is altered; thus, the maximum slip tendency should also be changed. Therefore, the slip tendency can be used as an indicator of the stability state of discontinuities and faults around the stimulated region.

In this work, the coefficient of friction is assumed to be independent of stresses, temperature, rock types and acts as a constant for all faults and discontinuities. Byerlee (1978) demonstrated that the friction behavior in laboratory experiments could be fit by a bilinear empirical expression. The coefficient of friction is found to be within a relatively small range ($0.6 \leq \mu \leq 1.0$). In general, measurement of the friction coefficient is rarely done in the field due to its complexity and cost (Reches et al. 1992).

As shown earlier, the maximum slip tendency (T_s) and the angle (β) between the normal of the corresponding slip surface and the maximum principal stress are functions of principal stresses. Given normalized initial in-situ stresses ($\sigma_v/\sigma_{h,min}$ and $\sigma_{H,max}/\sigma_{h,min}$), T_s and β are obtained under different in-situ stress fields, illustrated in Error! Reference source not found.. The relations among β, μ and σ_1/σ_3 are discussed in detail for different faulting environments in Zoback (2007).

2.5.2. Fault slip-tendency during hydraulic stimulation

Through the combination of Mohr-Coulomb criterion and analytical solutions for the stress distribution around a single fracture, the slip tendency of faults during hydraulic fracturing stimulation can be derived. Sneddon and Elliot (1946) derived the analytical solutions for the stress distribution in the vicinity of a semi-infinite crack in an elastic medium. In order to simplify the problem, they assumed that the fracture is open under uniform internal pressure and it is in plane strain condition, with limited height and infinite length.

Error! Reference source not found. illustrates the geometry of a pressurized crack, *x* indicates the direction of minimum horizontal principal stress, *y* indicates the vertical direction, and the direction of maximum horizontal principal stress is perpendicular to the x-y plane. The orientations of maximum, intermediate and minimum stresses are related to three forms of faulting environments according to Anderson's fault theory (Anderson and Hubbert 1972). The vertical stress is considered as a principal stress, the directions of other two principle stresses are parallel to the earth's surface. The slip tendency and the orientation of the slip plane are functions of maximum and minimum principal stresses, as shown in Eq. **Error! Reference source not found.**. In the present study, we discuss the normal and strike-slip faulting environments. For the reverse faulting environment, the hydraulic fracture plane is horizontal.

Normal faulting environment

At initial conditions, the slip tendency is set equal to a particular coefficient of friction. With the given slip tendency, the ratio of σ_1 to σ_3 can be calculated based on Eq. (7). In this work, normal and strike-slip faults are considered. σ_{hmin} is the minimum principal stress (σ_3) in both normal and strike-slip faulting environment. σ_v is the maximum principal stress (σ_1) in normal faulting environment. In strike-slip faulting environment, σ_{Hmax} is the maximum principal stress (σ_1). σ_v is the intermediate principal stress, which is not included in Mohr-Coulomb failure criterion, thus not considered in slip tendency calculation. In addition, the applied injection pressure is usually larger than the minimum principal stress (σ_{hmin}), which is a prerequisite for hydraulic stimulation design. The difference between the injection and the minimum principal pressure is called net pressure (p_{net}). Induced stresses around pressurized hydraulic fracture are functions of p_{net}, as shown by Sneddon and Elliot (1946). Here p_{net} is also normalized by $\sigma^0_{h,min}$, which is convenient with respect to hydraulic stimulation design.

Strike-slip faulting environment

According to Anderson's faulting theory, the strike-slip fault requires that the maximum and minimum principal stresses lie in a horizontal plane, so that $\sigma_1 = \sigma_{H,max}$, $\sigma_3 = \sigma_{h,min}$. The analytical expressions derived by Sneddon and Elliott (1946) assume that the fracture is semi-infinite, which indicates the generated maximum horizontal stress due to hydraulic stimulation could be calculated according to the plane strain condition. In actual hydraulic fracturing process, the length of fracture is finite in the direction of maximum horizontal stress and stress state right at the fracture tip does not follow the plane strain solution. However, away from the fracture tip, such as at the center of the pressurized

hydraulic fracture, the 3D stress field could be approximated by the plane strain solution (Roussel and Sharma 2011; Cheng 2012), which is manifested in the following 3D numerical simulation.

Slip tendency (T_s) is a function of initial in-situ stresses. During hydraulic fracturing stimulation, the slip tendency is calculated on the plane with dip angle θ determined by the initial stress state. The slip tendency along the line with ϑ = 90° and ϑ = 30° are plotted vs. the dimensionless distance r/H in Error! Reference source not found.. ϑ = 90° represents a horizontal central line perpendicular to the fracture. (a) Indicates that the maximum slip tendency decreases during hydraulic stimulation, which implies the faults, if existing, around the pressurized fracture become more stable along these paths. The slip tendency restores to its initial value as the distance from the fracture increases. For ϑ = 30°, there is a critical point at r/H = 0.5 that implies when r/H < 0.5, the slip tendency is less than its initial value. Beyond the critical point, the slip tendency is larger than its initial value. This suggests that the stability states of faults distributed along the line with ϑ = 30° change from stable to unstable as the distance from the pressurized fracture increases. Higher in-situ stress contrast, corresponding to larger value of σ_1/σ_3, generates larger T_s and larger perturbed region of T_s. Despite this difference, the patterns of slip-tendency distributions around a pressurized fracture are the same for a particular faulting regime. In the following, only the initial in-situ stresses corresponding to an initial slip tendency of 0.6 is adopted for description concise.

The shear and normal stresses around a pressurized fracture are functions of r and ϑ, and so is the slip tendency. It is shown that at some distance from the pressurized fracture, about r>2.5H, T_s, τ and σ remain as constants along r, regardless of ϑ value. Under this condition, a homogeneous stress field dominates the stress distribution, and the slip tendency is close to 0.6. However, within this range, T_s, τ and σ are dependent on the position of the point around the fracture with a completely nonlinear relation. For ϑ > 50° and r < 2.5H, the slip tendency decreases as the θ increases and takes a value less than 0.6 and slip tendency reaches to its minimum value at ϑ = 90°. This indicates that the faults or discontinuities become more stable within this range and they become more and more stable as θ increases toward 90°. On the other hand, when ϑ < 50° the slip tendency is larger than 0.6, that means pre-existing faults or discontinuities will become unstable within a zone of width less than 2.5 times the height of the fracture. Moreover, when ϑ < 50° the slip tendency increases with the decrease in ϑ at r < 0.75H. However, beyond this range the trend is reversed. It is clearly shown that the extent of the unstable region is less than that of stable one.

The normal and shear stresses calculated for different value of ϑ angle for both Normal and strike-slip faulting environments. They clearly show that along the horizontal line perpendicular to fracture surface (ϑ = 90°), the shear stress decreases, while, the normal stress increases, and the combination of these two effects leads to reduction of the slip tendency. Along the vertical line (ϑ = 0°), however, the shear stress remains constant in the normal faulting environment since there is no change in the shear stress in this direction. In the strike-slip faulting environment the shear stress increases where r < 0.5H, and decreases if r > 0.5H. The normal stress on the other hand increases in vertical direction for both normal and strike-slip faulting environments. T_s, τ and σ experience abrupt alteration at the point where r = 0.5H, especially when ϑ has low values, this is due to the stress singularity at the pressurized fracture tips.

In many situations at scales comparable to horizontal well lengths, pre-existing fractures and faults are presented in many rocks targeted for hydraulic fracturing (Laubach et al. 2009). Despite vertical coring is

in the least favorable configuration for sampling near vertical fractures, frequently observed sub vertical cement-filled fractures in vertical shale core indicate they are abundant under the subsurface (Gale et al. 2014). Some of these discontinuities are likely to be well-oriented for slip in the initial in-situ stress field prior to stimulation, and these are sometimes termed as critically-stressed faults or discontinuities (Zoback 2007). In the regions surrounding the hydraulic fractures where $r < 2.5H$ and $\vartheta < 50°$, the critically-stressed faults and fractures (or any other kind of discontinuities), if they exist, are expected to slip on fault planes and to create a network of permeable flow paths, thus enhancing productivity from low permeability reservoirs, such as organic-rich shale gas reservoirs. This discussion is valid for both normal and strike-slip faulting environments.

Successful development of unconventional reservoir with extremely low permeability is largely depended on natural fracture networks underground (Mayerhofer et al. 2010). The relationship between fracture development and mechanical stratigraphy provides a way to extrapolate surface geological characteristics and scatter information from field and laboratory experiments into the subsurface at different simulated burial depths (Corbett et al. 1987; Laubach et al. 2009). Mechanical stratigraphy divides stratified rock into discrete mechanical elements such as brittleness, fracture mechanical properties, and rock strengths.

The interaction between a hydraulic fracture and a natural fracture is a complex process. The hydraulic fracture could be arrested by natural fracture, or cross natural fractures. Microseismic events were observed well after the fracture tip has passed. In some cases, half or more of the seismic events are clearly not related to the fracture tips and occur all along the length of the existing fracture (Warpinski et al. 2013). These events are most likely caused by leakoff of the high-pressure fracturing fluid into natural fractures or other permeable discontinuities which intersect with created hydraulic fracture. For example, natural fracture may be perpendicular to the created hydraulic fracture. When hydraulic pressure is sufficient enough to overcome the stress acting on natural fractures (maximum horizontal stress plus induced stress by hydraulic fractures), the nature fractures or other discontinuities tend to be opened and act as flow paths. Due to pore pressure dissipation during these processes, the slip-tendency tends to be raised, the contour of it would be enlarged.

The net pressure is equal to the hydraulic pore pressure minus the minimum horizontal stress σ_{hmin}. It is shown that higher net pressures generate a larger magnitude of slip tendency where $r > 0.5H$. The normal faulting environment demonstrates larger variations in slip tendency than the strike-slip faulting environment as a function of hydraulic net pressure. The maximum differences of T_s, $\tau/\sigma_{h,min}$ and $\sigma_n/\sigma_{h,min}$ between the two faulting stress regimes are 0.01, 0.12 and 0.06, respectively. Where $r < 0.5H$, the relationships are reversed, and the faults under the strike-slip faulting environment become more stable than in the normal faulting environment.

2.5.3. Numerical analysis of Fault Slip Tendency

Numerical modeling of stress distributions around pressurized fractures has been well described in the literature (Warpinski and Branagan 1989; Roussel and Sharma 2011; Cheng 2012). Stress reorientation and stress interference of multiple fractures were also analyzed for the purpose of well-spacing optimization. In this study, 3D finite element models are developed to simulate the distribution of slip tendency for faults parallel to σ_{Hmax} in a normal faulting regime and for faults parallel to σ_v in a strike-slip faulting regime. We used in-house codes to perform simulations. The element type was 20-node hexahedron element. The bottom boundary was fixed in vertical direction. Roller boundary and traction

boundary conditions were used for the rest of boundaries in order to generate horizontal and vertical stresses.

The fracture surfaces on which hydraulic pressure is imposed are treated as interior boundaries in numerical model, where a constant pressure is acting normally on the surfaces of the fractures. When hydraulic pressure is applied, the pressure is transferred into node forces, and the forces are applied along the surfaces. The remaining model should experience stress redistribution so that the surfaces where hydraulic pressure is applied are indeed 'interior boundaries'. The basic reservoir model and fracture properties are provided. Multiple pressurized fractures are assumed having the same dimensions within the model and fracture spacing is set to be 100 ft. The influence of fracture spacing on stress distributions was analyzed in Germanovich and Astakhov (2004), Roussel and Sharma (2011) and Cheng (2012). As stated earlier, the faults and other discontinuities are under critical conditions, and have an initial in-situ stress field, which generates a slip tendency of 0.6 on a plane with the angle β equal to 60°. In the normal faulting environment, the ratio of vertical to minimum horizontal stresses ($\sigma_v/\sigma_{h,min}$) is calculated as 3.12. In strike-slip faulting environment, the ratio of maximum horizontal to minimum horizontal stresses ($\sigma_{H,max}/\sigma_{h,min}$) is also 3.12. For all the numerical models, $p_{net}/\sigma_{h,min}$ is set as 0.2.

2.5.4. Effect of a single pressurized fracture on fault stability

The analytical solution for stress distribution around a single pressurized fracture was derived based on the plane strain condition (Sneddon and Elliot 1946; Atkinson 1987). In this study, the results of the 3D numerical model with a single fracture were compared with analytical solutions. Induced horizontal stresses in the directions perpendicular ($\Delta\sigma_{yy}$) and parallel ($\Delta\sigma_{xx}$) to the fracture as well as the induced vertical stress ($\Delta\sigma_{zz}$) were calculated along a symmetric line of the fracture. This symmetric line is perpendicular to the fracture. The normalized induced stresses represented by the ratio of stress changes to the net pressure (p_{net}), along the distance perpendicular to fracture face (L) normalized by fracture height (H).

An excellent agreement has been achieved between the numerical and analytical solutions. The similar verification of the stress distribution around a pressurized fracture can be found in Warpinski and Branagan (1989), Roussel and Sharma (2011), and Cheng (2012). The induced stresses in the y-direction (direction of the initial minimum horizontal stress) are always larger than those in the x-direction (direction of the initial maximum horizontal stress) and the extent of the stress-reversal region and the reoriented-stress region largely depends on the initial in-situ stress contrast and net pressure. When the initial in-situ stress contrast ($\sigma_{xx} - \sigma_{yy}$) is larger than the generated stress contrast ($\Delta\sigma_{yy} - \Delta\sigma_{xx}$), there will be no stress-reversal region in the vicinity of the fracture, however, a reoriented-stress region still exists around the fracture tips.

Based on 3D numerical simulations, the generated stress contrast ($\Delta\sigma_{yy} - \Delta\sigma_{xx}$) normalized by net pressure (p_{net} = 1000 psi) is plotted along a symmetric line normal to the fracture. The maximum ratio of the generated stress contrast ($\Delta\sigma_{yy} - \Delta\sigma_{xx}$) to net pressure ($p_{net}$) is less than 0.7 and there would be no stress-reversal regions if the normalized initial in-situ stress contrast $(\sigma_{xx} - \sigma_{yy})/p_{net}$ is larger than 0.7. Here, we assume $(\sigma_{xx} - \sigma_{yy})/p_{net}$ is larger than 0.7 for normal faulting environment, that means there are no stress-reversal regions around the single pressurized fracture, is still applicable for the calculation of slip-tendency. In strike-slip faulting environment, $(\sigma_{xx} - \sigma_{yy})/p_{net}$ is equals to 10.6, so that there are no stress-reversal regions around the pressurized fracture, in this case the slip-tendency can be obtained.

As mentioned before, we evaluate the slip tendency at each node of the numerical model on a plane with β equal to 60°. Distributions of normalized normal and shear stresses (σ_n/p_{net}, τ/p_{net}) on a vertical profile through the center point of the pressurized fracture are presented for normal and strike-slip faulting environments, respectively. The shear stress (τ/p_{net}) on fault planes with β = 60° has both the maximum and minimum values around the fracture tips, since the direction of shear stress (σ_{vh}) is opposite to each other on the two sides of the fracture. The distribution of normalized shear and normal stresses are anti-symmetrical relative to the fracture for the normal faulting environment, which is, however, symmetrical for the strike-slip faulting environment. This is due to the fact that the normal fault plane at each finite element node intersects the pressurized fracture with an intersection line in horizontal direction, as indicated (b), however, the strike-slip fault plane has an intersection line in vertical direction. Generally, the hydraulic pressure creates larger normal stress (σ_n/p_{net}) in the regions around the fracture surfaces and leads to the decease of normal stress in the regions extended from fracture tips due to the tensile stress created around fracture tips.

The distribution of slip tendency for normal and strike-slip faulting environments, respectively. The contour lines in (a) and (b) represent the initial slip tendency of 0.6. After applying hydraulic pressure, the slip tendency tends to decrease along the distance perpendicular to the fracture face, which indicates the faults or other discontinuities (such as natural fractures) become more stable within this region. On the other hand, along the distance parallel to the fracture face, the slip-tendency tends to increase, this indicates that the discontinuities become unstable and have potential to slip within this region. The stable and unstable regions are shown in a 3D model(c). The unstable region could be treated as stimulated zone, where permeability could have been improved. The above mentioned characteristics of the normal faulting environment are also valid in the strike-slip faulting environment.

Three parallel fractures were simultaneously generated in our 3D numerical model through a single stage hydraulic fracturing treatment with three perforation clusters, vertical profiles for the distribution of shear and normal stresses projected on a plane with β equal to 60° (Figure 3) at each numerical node. The shear stresses (τ/p_{net}) around the tips of the two out most fractures are increased significantly due to the creation of hydraulic fractures. Within the regions between the two out most fractures, the shear stresses (τ/p_{net}) decrease while the normal stresses (σ_n/p_{net}) increase. Similar to the single pressurized fracture model, the distributions of shear and normal stresses are non-symmetrical relative to the fractures for the normal faulting environment, and are symmetrical for the strike-slip faulting environment.

The distribution of the slip tendency under normal and strike-slip faulting environments. The trends of slip-tendency distribution for models having multiple pressurized fractures are similar to those of a single pressurized fracture. In the direction normal to the fracture faces, the slip tendency is less than the initial value of 0.6 and the minimum slip tendencies occur at the regions close to the fracture faces having the values of 0.473 and 0.476 for normal and strike-slip faulting environments, respectively. On the other hand, along the direction parallel to the facture faces, especially for the regions nearby the fracture tips, the slip tendency is greater than 0.6 where the maximum values of slip-tendency for normal and strike-slip faulting environments are 0.925 and 0.944, respectively. The extent of unstable regions on the boundaries (a) is 2200 ft. and 3000 ft. for normal and strike-slip faulting environments, respectively. The extent of unstable regions on the boundaries in (b) are 1180 ft. and 1100 ft., respectively. (c) Present the contour surface for a slip tendency of 0.6.

Comparing the distributions of slip tendency from to, following observations have been made: (1) It is found that the shapes of the slip-tendency contours are highly depends on the types of faults; (2) If critically stressed faults or other discontinuities (such as natural fractures) exist within the unstable regions around the hydraulic fracture, these regions can be considered as improved apparent permeability regions.

2.6. Fracture Efficiency Assessment

Velocity and pressure fields for an incompressible fracturing fluid can be obtained solving Navier-stokes equations using finite difference technique. Under the assumption of constant density, the mass and momentum governing equations can be simplified as follow:

$$\frac{\partial v_x}{\partial x} + \frac{\partial v_y}{\partial y} = 0$$

$$\frac{\partial v_x}{\partial t} + \frac{\partial P}{\partial x} = -\frac{\partial ({v_x}^2)}{\partial x} - \frac{\partial (v_x v_y)}{\partial y} + \frac{1}{Re}\left(\frac{\partial^2 v_x}{\partial x^2} + \frac{\partial^2 v_x}{\partial y^2}\right)$$
$$\frac{\partial v_y}{\partial t} + \frac{\partial P}{\partial y} = -\frac{\partial (v_x v_y)}{\partial x} - \frac{\partial ({v_y}^2)}{\partial y} + \frac{1}{Re}\left(\frac{\partial^2 v_y}{\partial x^2} + \frac{\partial^2 v_y}{\partial y^2}\right)$$

The mass conservation equation is time-independent for incompressible flow that makes it an additional constraint for the momentum conservation equations. To capture the dynamics of flow, a commonly used projection method is preferred to solve discrete equations. The key advantage of the projection method is to decouple velocity and the pressure fields. Nonlinear convection, viscous diffusion and pressure correction can be calculated in three steps: I) Solve the momentum equation for intermediate velocity field without explicit pressure variation, then II) Solve pressure Poisson equation based on intermediate velocity field and III) Update the intermediate velocity field using pressure gradient.

2.6.1. Proppant transport in hydraulic fractures

Proppant pumped in vertical hydraulic fractures mainly moves in two directions, horizontal and vertical. Horizontal movement along fracture length follows fluid flow in horizontal direction where no slippage between proppant and fluid is concerned. Horizontal movement of proppant in the fracture width direction is usually negligible due to the small scale of the fracture width in compare to fracture length and height. Vertical motion of proppant, however, is induced by fluid flow in vertical direction and gravity forces. Vertical velocity of proppant is referred as settling velocity and is influenced by fracturing fluid properties (density and viscosity), solid properties (proppant size and density) and fracture geometry. Proppant settling stops when the proppant concentration in the slurry reaches to the maximum value beyond which it cannot move, or the fracture width becomes so small that proppant particles stuck by fracture walls due to proppant particles form a bank filling the fracture.

The governing equation for proppant concentration is:

$$\frac{\partial c v_y^p}{\partial y} + \frac{\partial c v_x^p}{\partial x} = \frac{\partial c}{\partial t}$$

Where v_x^p and v_y^p are proppant velocity in horizontal and vertical direction respectively, v_x and v_y is fluid velocity, v_{settle} is proppant settling velocity induced by gravity, c is the proppant concentration by volume.

Finally, the corrected settling velocity can be obtained as:

$$\mathrm{v_{settle}} = \mathrm{V_\infty}\left[0.563\left(\frac{\mathrm{d_p}}{w}\right)^2 - 1.563\left(\frac{\mathrm{d_p}}{w}\right) + 1\right](2.37c^2 - 3.08c + 1)$$

2.6.2. Fracture Geometry and Permeability

Different hydraulic fracturing models have been developed to study the nonlocal relationship between the net pressure in the fracture and fracture width and non-linear relationship between the fluid flow in the fracture and fracture width including the plane strain, PKN, and axisymmetric penny-shaped models. In this paper, an in-house numerical simulator (HFWVU) based on PKN model and the finite element method is used to simulate hydraulic fracturing in a unified way where no additional effort is needed to track the fluid front explicitly when a fluid lag exists or occurs. The simulation results of HFWVU have been confirmed with asymptotic solutions in different hydraulic fracturing regimes. After expected hydraulic fracture length is achieved injection stops and fracturing fluid will be produced during the flow-back process and fracture starts to closing up due to overburden pressure. This process increases the proppant concentration till it reaches a maximum value depending on the proppant distribution during injection period and stops the fracture walls from closing the fracture. The maximum proppant concentration required to stop closing the fracture is around 0.634, assuming the proppant particles are perfect spheres and considering irregular sphere packing theory. This is also verified by experimental studies using different proppant size. Experimental studies show that fracture width can be reduced by about 16% from 0 closure stress to 8000 psi closure stress.

While studies did confirm that closure pressure can crush proppant particles or embed proppant particles into fracture walls, leading to a reduction of proppant pack permeability, it is also shown that this effect can be ignored when the closure pressure is under 4000 psi.

2.6.3. Fluid flow during production

During the gas production from the hydraulically fractured reservoir, single-phase gas flow in proppant pack is governed with similar mass and momentum conservation equations that govern fluid flow in porous media.

The governing equation of compressible fluid flow in porous media can be written as:

$$\frac{\partial}{\partial x}\left(\frac{k_x A_x}{\mu B}\frac{\partial \Phi}{\partial x}\right)\Delta x + \frac{\partial}{\partial y}\left(\frac{k_y A_y}{\mu B}\frac{\partial \Phi}{\partial y}\right)\Delta y + \frac{\partial}{\partial z}\left(\frac{k_z A_z}{\mu B}\frac{\partial \Phi}{\partial z}\right)\Delta z + q = v_b\frac{\partial}{\partial t}\left(\frac{\emptyset}{B}\right)$$

First the proppant distribution in a single hydraulic fracture is obtained and then hydraulic fracture geometry and fracture permeability after flow back is calculated. The simulation results of hydraulic fracture geometry and permeability after the flow back are then used in a fractured reservoir model for hydraulic fracturing performance optimization. Here, the dimensionless productivity index "I" is employed to compare the performance of different hydraulic fracturing operations.

$$I = J_a/J_b$$

Where J_a is the productivity index after stimulation, J_b is the productivity before stimulation.

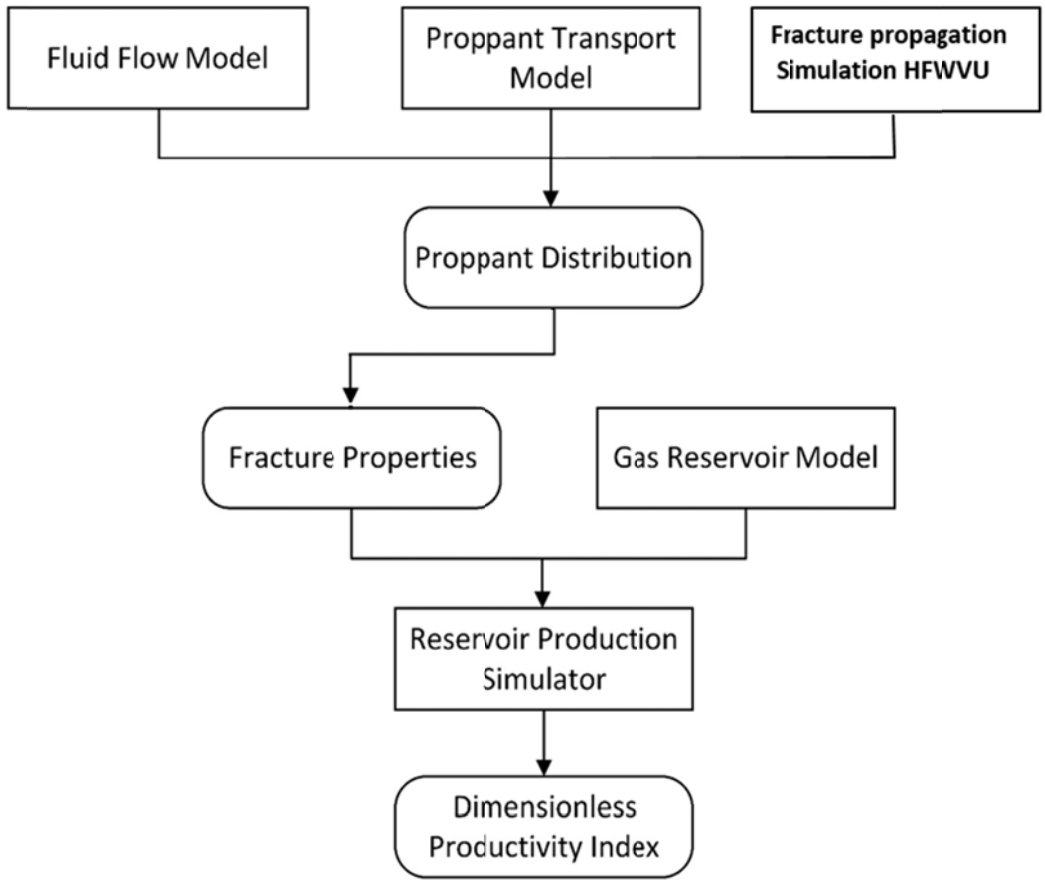

Figure 23 - Flow chart of fracture-proppant efficiency research

The figure below illustrates the schematic of the hydraulically fractured reservoir model that is a 500*500*10 ft^3 reservoir with a producer located at the center of the reservoir. Symmetric behavior is assumed, therefore, reservoir performance analysis will be performed on a quarter of the entire model. The range of proppant size is very important. Typical proppant sizes are generally between 8 and 140 mesh (106 µm - 2.36 mm), including 16-30 mesh (600 µm – 1180 µm), 20-40 mesh (420 µm - 840 µm), 30-50 mesh (300 µm – 600 µm), 40-70 mesh (212 µm - 420 µm) and 70-140 mesh (106 µm - 212 µm). When describing frac sand, the product is frequently referred to as simply the sieve cut, e.g. 20/40 sand. The range of proppant size used here is a typical proppant sizes, i.e., 0.1-0.8 mm. For the base case the proppant size of 0.6 mm, i.e., 20/40 mesh, and reservoir permeability of 100 nano-Darcy is assumed with maximum fracture half-length of 200 ft.

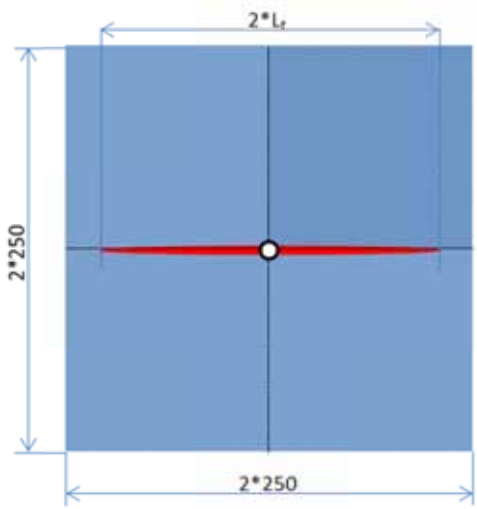

Figure 24 - Overlook of the gas reservoir model for simulation

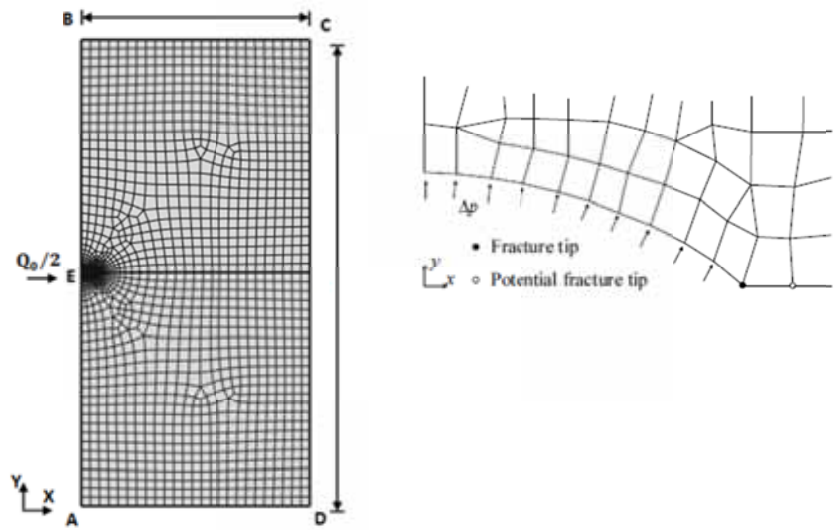

Figure 25 - (a) Single fracture propagation model with 100 elements (HFWVU) (b) Discretization of the equivalent quarter model with finite elements in HFWVU

The effect of Proppant transport and settling on pressure and permeability distributions in a single hydraulic fracture in Marcellus shale gas reservoir is investigated and compared with commonly used uniform proppant distribution models. The effects on efficiency of hydraulic fracturing stimulation in different cases is compared using dimensionless productivity index of the hydraulically fracture reservoir. Next, the effect of injecting different proppant size and volumes for different reservoir permeability and initial fracture geometries are studied and multi-proppant size combination treatment for maximum stimulation efficiency is obtained for a specific set of reservoir parameters. Systematic approach based on design of experiments has been used to determine the most important parameters and their correlations impacting the hydraulic fracturing stimulation performance. Multi-proppant size combination treatment is also optimized.

3. Results

3.1. Static 3-Dimensional Model

Normal Faulting Environment

Figure 26 (a) normalized shear stress, normal to the z-axis and **(b)** normalized shear stress, normal to the y-axis below represents shear stress distributions in a normal faulting environment in a homogenous environment surrounding a single fracture. It can be seen from the distribution on the diagrams that the shear stress magnitude (dark blue) have decreased slip tendency. The magnitude of shear stress is seen to be amplified along the tips of the fracture while a reduction in shear stress is seen across the body of the fracture.

(a) **(b)**

Figure 26 Ratio of Shear Stress by Net Pressure Surrounding a Single Fracture in a Normal Faulting Environment

The normal stress surrounding the fracture is seen below in **Figure 27 (a)** normalized normal stress, normal to the z-axis and **(b)** normalized normal stress, normal to the y-axis. This indicates that the stresses are highest around the body of the fracture in this environment. The skewed nature of these stresses is representative of the ratios of σ_{hmin} and σ_{Hmax}. This normal stress shown in orange/red have an increased slip tendency.

(a) **(b)**

Figure 27 Ratio of Normal Stress by Net Pressure Surrounding a Single Fracture in a Normal Faulting Environment

Strike-Slip Faulting Environment

The following results present the stresses determined for a strike-slip faulting environment where σ_{hmin} and σ_{Hmax} are switched from the results shown above for a normal faulting environment. **Figure 28 (a)** normalized shear stress, normal to the z-axis and **(b)** normalized shear stress, normal to the y-axis displays the effects of shear stresses upon the fracture. This also indicates the role that the principle stresses play in the stress surrounding the fracture in comparison with **Figure 26**.

(a) **(b)**

Figure 28 Ratio of Shear Stress by Net Pressure Surrounding a Single Fracture in a Strike-Slip Faulting Environment

Figure 29 (a) the normal stress, normal to the z-axis and **(b)** the normal stress, normal to the y-axis displays the effects of the normal stress surrounding the fracture. This displays a similar pattern to that seen in the shear stresses above due to the way in which the principal stresses are oriented. This again displays significantly different results than the normal faulting environment.

(a) **(b)**

Figure 29 Ratio of Shear Stress by Net Pressure Surrounding a Single Fracture in a Strike-Slip Faulting Environment

Fault Reactivation / Slip-Tendency

The following Figure 30 **(a)** slip tendency, normal to the z-axis and **(b)** slip tendency, normal to the y-axis display the distributions of slip-tendency in a normal faulting environment. The contour lines on both the 2D models represent a 0.6 slip-tendency (reactivation factor), as discussed earlier. The diagrams below indicate that in the regions surrounding the fracture tips the zones can be said to decrease in stability while the zones lying adjacent to the fracture tend to increase in stability.

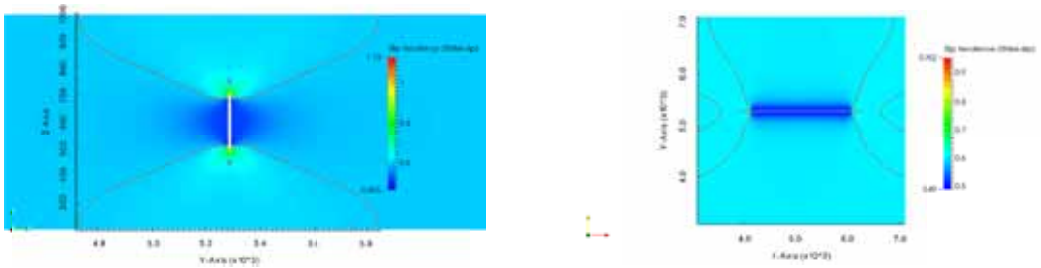

(a) **(b)**

Figure 30 Slip-Tendency for a Normal Faulting Environment Surrounding a Single Fracture, Ts=0.6

The pattern described above becomes more visible with the aid of the 3D diagram shown below in **Figure 31**. This is a representation of the reservoir volume where the zones highlighted in red are indicative of a particular reacivation factor in a critically stressed state.

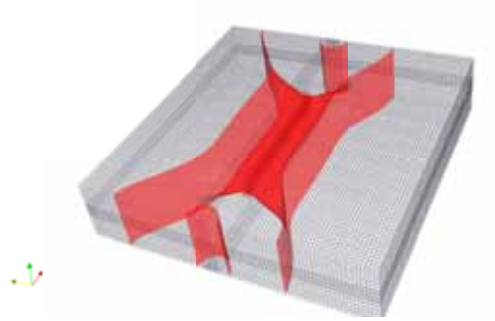

Figure 31 3-D Slip-Tendency For a Normal Faulting Environment And Single Fracture, Ts=0.6

The distributions of slip-tendency in Figure 32 **(a)** slip tendency, normal to the z-axis and **(b)** slip tendency, normal to the y-axis for a strike-slip faulting environment. The contour lines on both 2D models represent the critically stressed conditions surrounding a single fracture in a homogenous reservoir domain.

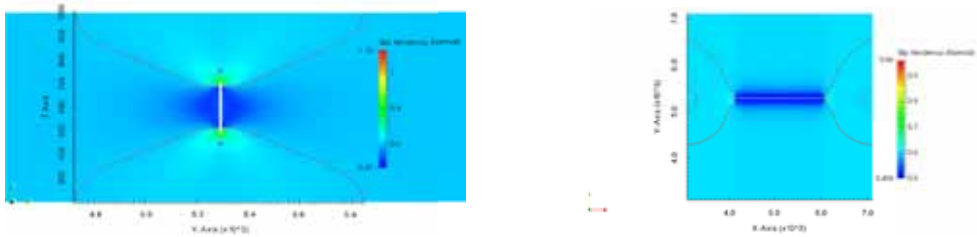

(a) **(b)**

Figure 32 Slip-Tendency for a Strike-SLip Faulting Environment And Single Fracture, Ts=0.6

The pattern for a strike-slip environment is shown below in **Figure 33** using a contour plot of the slip tendency factor in a critically stressed state. The strike-slip environment is shown to extend its instability towards the outer extents of the reservoir domain

Figure 33 3-D Slip-Tendency For a Strike-Slip Faulting Environment And Single Fracture, Ts=0.6

5.3.2 Three Fracture Model

Normal Faulting Environment

The identical simulation was carried out for a set of three fractures as was in the base of a single fracture in the previous section. The shear and normal stress are shown below for the case of a normal faulting environment in **Figure 34 (a)** shear stress surrounding three fractures, normal to the z-axis and **(b)** shear stress surrounding three fractures, normal to the y-axis. For a normal faulting environment the

stress is distributed non-uniformly for both shear and normal stresses, however the normal stress depicts an increase in slip tendency while the shear stress shows a decrease in slip tendency across the normal faulting environment.

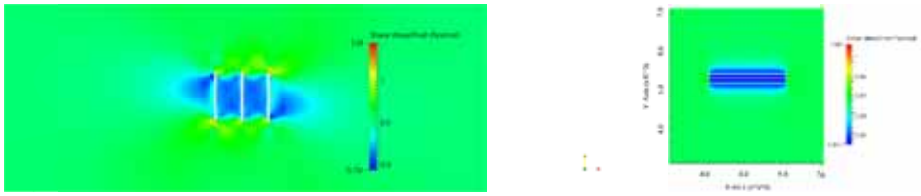

(a) **(b)**

Figure 34 Ratio of Shear Stress by Net Pressure Surrounding Multiple Fractures

Figure 35 (a) normal stress surrounding three fractures, normal to the z-axis and **(b)** normal stress surrounding three fractures, normal to the y-axis displays the normal stresses surrounding three congruent fractures in a normal faulting environment. This displays a similar trend as those depicted in the single fracture case. This static analysis does not lend insight to many of the interactions that will be portrayed later in this thesis regarding these transient stress dynamic.

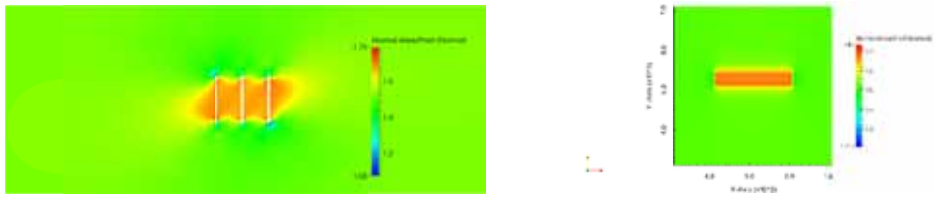

(a) **(b)**

Figure 35 Ratio of Shear Stress by Net Pressure Surrounding Multiple Fractures

Strike-Slip Faulting Environment

The shear and normal stress are shown below for a strike-slip faulting environment. **Figure 36 (a)** shear stress surrounding three fractures, normal to the z-axis and **(b)** shear stress surrounding three fractures, normal to the y-axis depict these results. The stresses are distributed uniformly across all three fractures for both normal and shear stresses. Again, the normal stress depicts an increase in the slip tendency while the shear stress depicts a decrease in slip tendency across the strike-slip faulting environment.

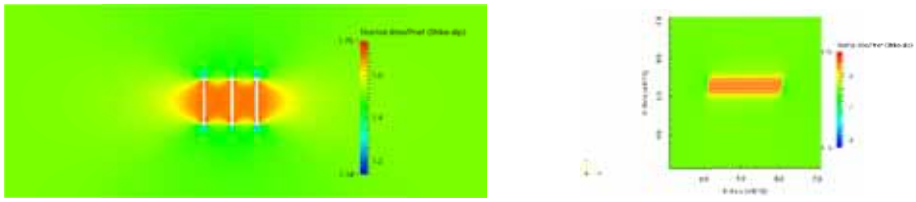

(a) **(b)**

Figure 36 Ratio of Shear Stress by Net Pressure Surrounding Multiple Fractures

Figure 37 (a) shear stress surrounding multiple fractures, normal to the z-axis and **(b)** shear stress surrounding multiple fractures, normal to the y-axis represent the shear stress distributions for a strike

slip faulting environment. These results indicate a similar behavior to that seen in the single fracture case with a uniform distribution spread across all three fractures.

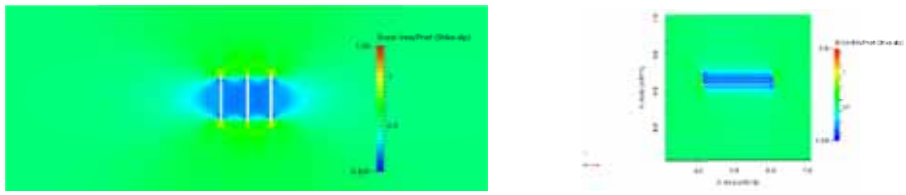

(a) **(b)**

Figure 37 Ratio of Shear Stress by Net Pressure Surrounding Multiple Fractures

Fault Reactivation / Slip-Tendency

The distribution of slip tendency is shown below in Figure 38 (a) slip tendency surrounding three fractures, normal to the z-axis and (b) slip tendency surrounding three fractures, normal to the y-axis for a normal faulting environment. Just as in the single fracture case a symmetrical slip tendency profile is seen with respect to the fracture tips.

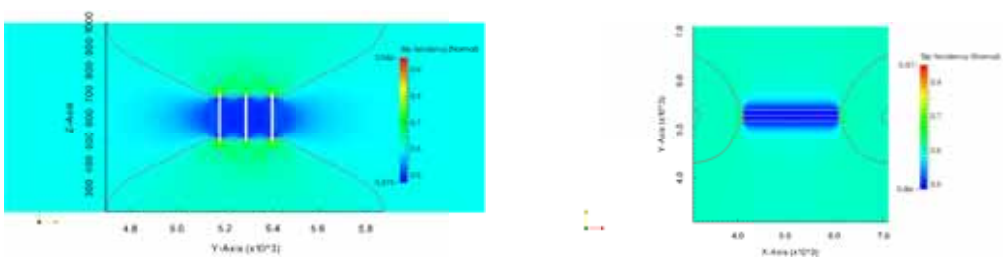

(a) **(b)**

Figure 38 Slip-Tendency for a Normal Faulting Environment Surrounding Multiple Fractures, Ts=0.6

Figure 39 below depicts the three dimensional sip tendency profile in the case of three fractures in a critically stressed state. This displays an expansion of the slip profile, however it is observed this is due to the additional fractures and not to the interaction of stresses as the profile does not change.

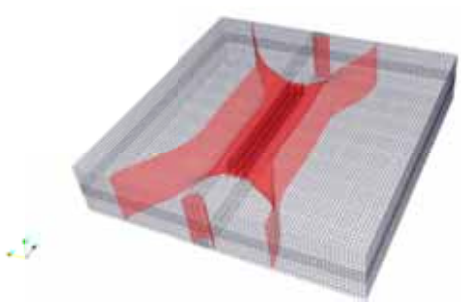

Figure 39 3-D Slip-Tendency For a Normal Faulting Environment And Multiple Fractures, Ts=0.6

Slip tendency for a strike-slip faulting environment is depicted in **Figure 40 (a)** slip tendency surrounding three fractures, normal to the z-axis and **(b)** slip tendency surrounding three fractures, normal to the y-axis. These slip tendency profile are again reflective of the same observations shown in the single fracture case.

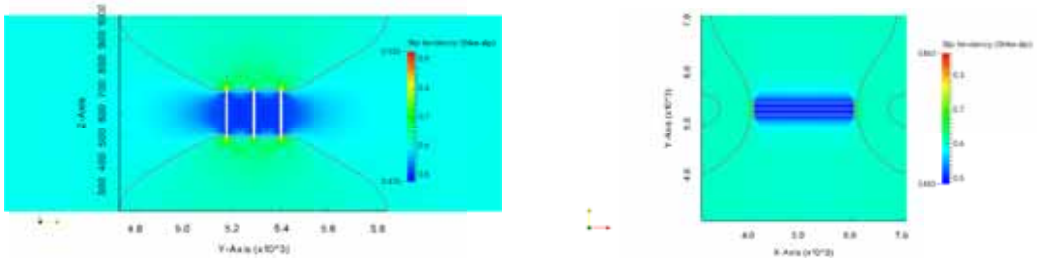

(a) **(b)**

Figure 40 Slip-Tendency for a Strike-SLip Faulting Environment Surrounding Multiple Fractures, Ts=0.6

A three-dimensional slip tendency plot is shown in **Figure 41** below for a three fracture case in a strike-slip faulting environment. This reflects the same results as shown in the single fracture case in **Figure 33**. There is a slight expansion of this profile but this is attributed to the extra 100 feet to each side of the center fracture due to the fracture spacing.

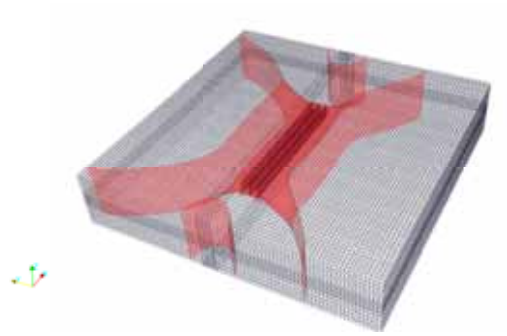

Figure 41 3-D Slip-Tendency For a Strike-SLip Faulting Environment And Multiple Fractures, Ts=0.6

3.2. Dynamic 2-Dimensional Model

One of the most observable impacts of these stresses surrounding the fracture is that upon the fractures geometry. This can be seen with propagation in systems with more than one concurrent fracture as the stresses from one or more fractures influences their length and width. The impacts of these stress behaviors and fracture width are depicted below for a system of three concurrent fractures in order to visualize these interactions. The fracture displacements have been magnified 2000 times in order to clearly see the interaction of these behaviors.

This series of figures in **Figure 42** displays a three fracture case at different moments in time. At **(a)** the initial fracture propagation the central fracture is smaller and longer as it is compressed by the large stresses that are exchanged with the onset of injection. As the fracture begins to propagate the stresses begin to interact as they being to equalize in **(b)**. The profile at **(c)** again displays an expansion of width where the impacts of the stresses from the central fracture begin to become apparent. The last figure **(d)** is taken at a time of 60 seconds where the effects of the stress interactions are clearly evident with the central fracture appearing symmetrical but the offset fractures appear oblique and the outer edge begins to point inwards, towards the central fracture.

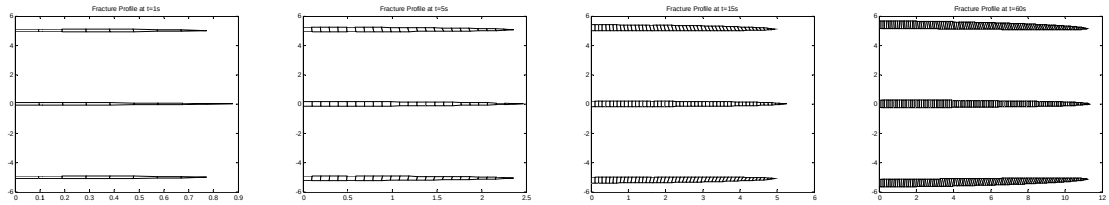

(a) **(b)** **(c)** **(d)**

Figure 42 The Development of the Fracture Profile in Three Concurrent Fractures at 5 Meters Spacing

The resultant effects of these stress interactions are clearly evident, however the development of this transient behavior is difficult to recognize from these images alone. In order to see these stress interactions the Von Mises stress has been displayed in **Figure 43** throughout the same time period as shown above for the fracture profile.

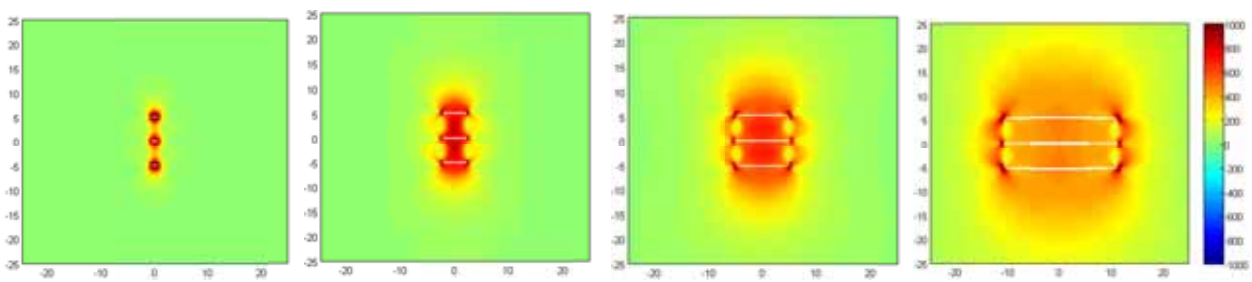

(a) **(b)** **(c)** **(d)**

Figure 43 The Development of the Von Mises Stress Surrounding Three Concurrent Fractures at 5 meters Spacing

3.3. Dynamic 3-Dimensional Model

The three dimensional model using the cohesive zone method was used to compare results throughout the two dimensional simulations. The verification of these previous assumptions and conclusions should hold true when expanding to the three dimensional model for validity if these conclusions are indeed true. Figure 20 and Figure 21 identify the discretization of the 3-D model used in this study.

These interactions are further investigated using the three-dimensional model where the fracture interaction can be visualized. The fracture width profiles are displayed below in **Figure 45** and **Figure 47** for the offset and center fracture in a three fracture system, respectively. Being a homogenous system at this point, the two outlying fractures are identical in their geometry and internal pressure distribution as they influence the center fracture equivalently. This interaction can be seen through the development of the center fracture through time as both its length and width are seen to be influenced in both rate of change and magnitude versus that of the outlying fracture(s).

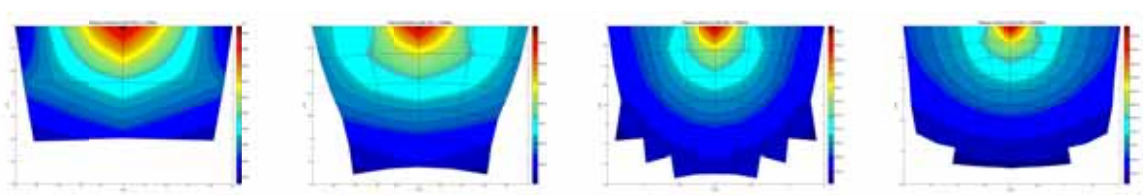

(a) **(b)** **(c)** **(d)**

Figure 44 Central Fracture Pressure Profile of 3D Solution at 5 Meters Spacing

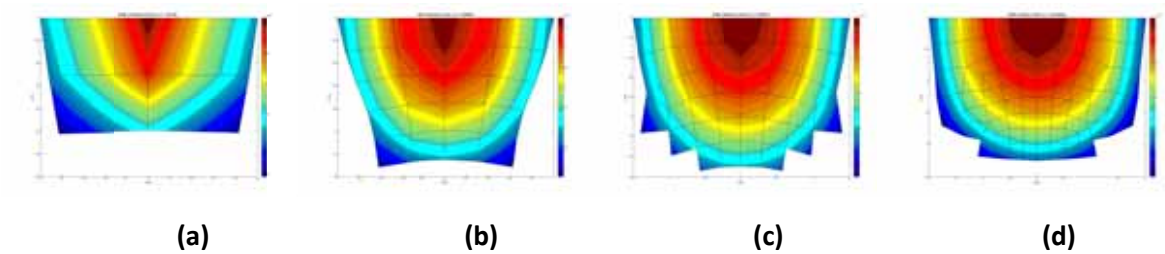

Figure 45 Central Fracture Width Profile of 3d Solution at 5 Meters Spacing

Although there is an impact seen throughout the development of the center fracture, it appears counterintuitively as the center fracture growth becomes arrested to the outer fracture development. In order to verify this observation this is being investigate in more detail in future work surrounding this topic.

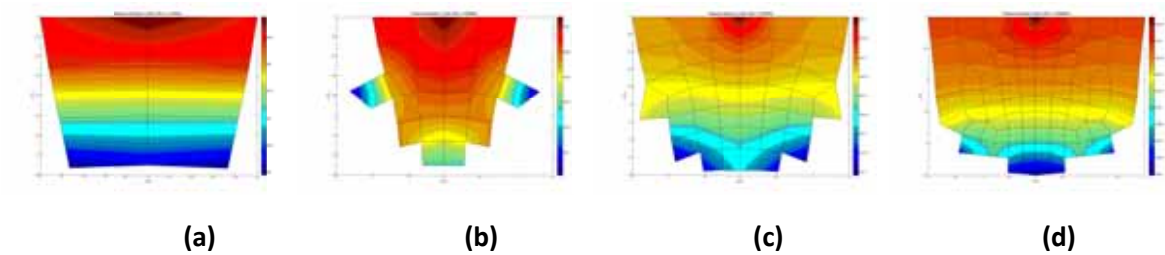

Figure 46 Offset Fracture Pressure Profile of 3D Solution at 5 Meters Spacing

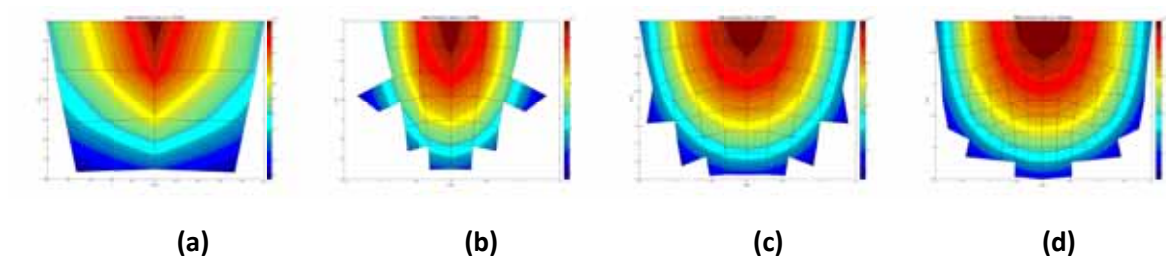

Figure 47 Offset Fracture Width Profile of 3D Solution at 5 Meters Spacing

The visualization of the fracture profile in 3-D is displayed below for same fracture in **Figure 48** and **Figure 49**. This highlights the opening of the 2-D cohesive zone layer which was discussed earlier. The development of the fracture occurs as the conditions are met for the entire element and therefore these diagrams do not depict a smoothly distributed fracture geometry.

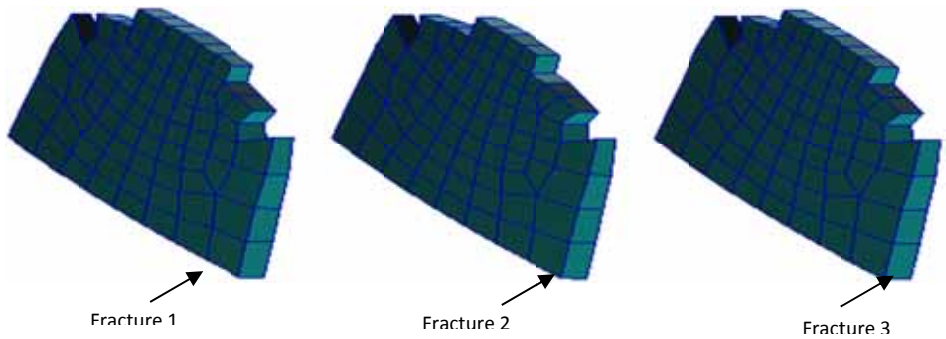

Figure 48 Three Dimensional Fracture Geometry at T=30s

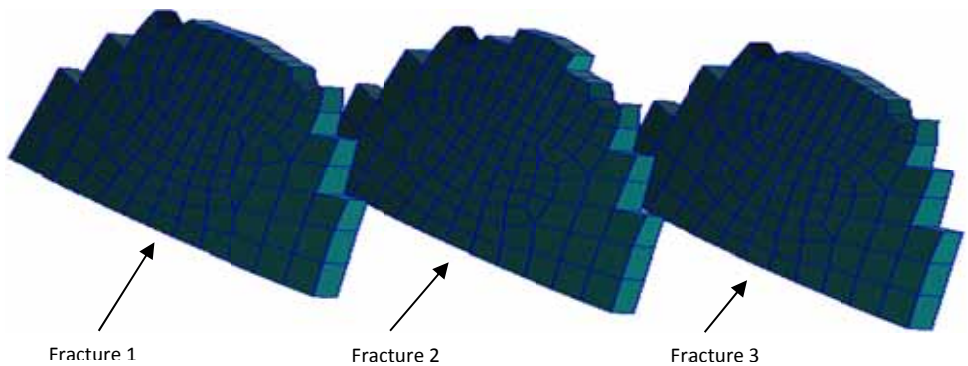

Figure 49 Three Dimensional View of Fracture Geometry at t=60s

The effects of injection pressure and fracture width have been studied using a relative relationship. Since the reservoir domain is homogenous and symmetrical, then the outlying fractures during simultaneous injection are equivalent. This generalization was used for comparison of the fracture width and pressure development throughout the injection period using the central fracture as a point of reference. In addition this generalization is made to the case of a single fracture at the center of the domain in order to determine the impacts of the simultaneous fracture development. These multi-fracture effects can be seen from the figures below.

Figure 50 depicts the pressure and width ratios of the central fracture versus the outlying or offset fractures in a three fracture system. This was to determine the impact of these outlying fractures on the central fracture development. The ratio of fracture pressure versus fracture width was used in order to determine these impacts. This investigation found that a linear relationship occurred, regardless of the injection rate which can be further developed in future study to create a direct correlation between these properties. It is predicted that this linear relationship will continue until the distance between fractures is reduced to a specific distance between the offset fractures.

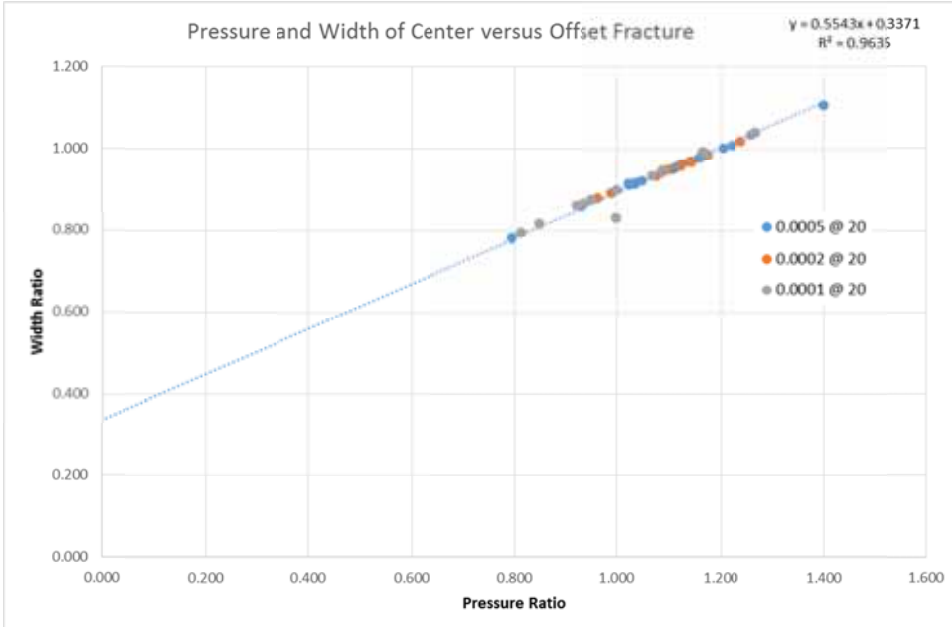

Figure 50 Pressure and Width of a Central Fracture Versus Offset Fractures

The baseline for the fracture geometry was made using the central fracture and a single fracture case to see the impact of the offset fractures in **Figure 51** below. This information will be used in addition to that found above in future study but it is apparent that the increase in the number of fractures impedes the growth of the fracture width. This is determined due to the influence of stresses surrounding the development of the fracture throughout its propagation which was discussed throughout the 2-D fracture simulation results.

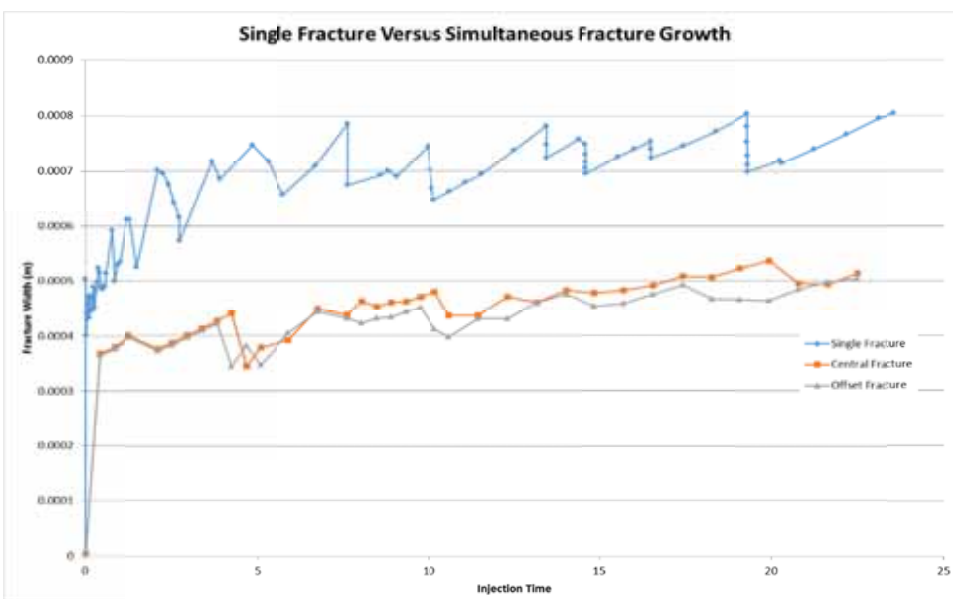

Figure 51 Single Fracture Development Versus Simultaneous Fracture Development

3.4. Fracture Development and Proppant Efficiency

If proppant settling velocity during the injection period is not considered, the proppant will distribute uniformly in the hydraulic fracture and results in a uniform distribution of hydraulic fracture permeability as shown in **Error! Reference source not found.** (left). Pressure distribution after 2 days in the hydraulic fracture and reservoir matrix are also shown in **Error! Reference source not found.** (right). Considering the fluid-rock interactions, however, leads to dynamic proppant settling velocity causing non-uniform proppant distribution along the hydraulic fracture, as clearly illustrated in **Error! Reference source not found.** (left). Pressure distribution after 2 days of gas production in the reservoir matrix and hydraulic fracture can also be obtained, **Error! Reference source not found.** (right).

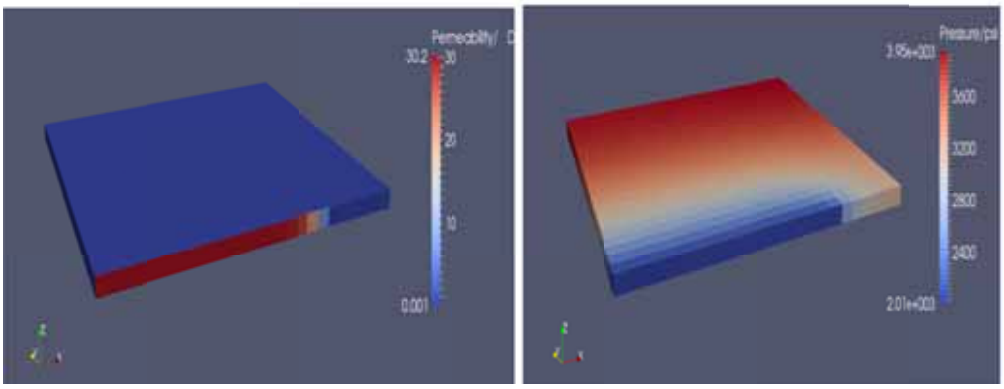

Figure 52 - Permeability (left) and pressure (right) distribution in reservoir and hydraulic fracture, considering zero proppant settling velocity

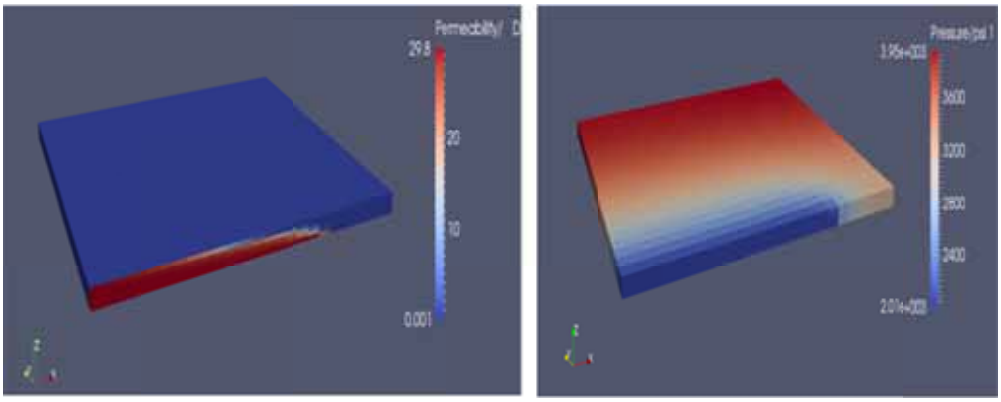

Figure 53 - Permeability (left) and pressure (right) distribution in reservoir and hydraulic fracture, considering dynamic proppant settling velocity

The effect of proppant settling velocity on hydraulic fracturing performance is investigated using dimensionless productivity index for the base case model. The simulation results show that ignoring the effect of proppant settling leads to more than 18.6% overestimation on dimensionless productivity index, i.e., the ratio of productivity index after and before stimulation, and therefore hydraulic fracturing stimulation efficiency. Decreasing the reservoir matrix permeability or increasing the proppant size pronounces the effect by 32.4% overestimation. Larger proppant size leads to much better proppant pack permeability, however, that increases the proppant settling velocity and creates early proppant banks that reduce propped area. Therefore it's critical to find the optimum proppant size that leads to best combination of proppant pack permeability and propped area leading to higher productivity index

of the fracture for given set of parameters defined in table 1. The proppant size has different impact on stimulation performance depending on the shale matrix permeability. In high permeability formations, i.e., K>100 μD for the sets of parameters defined in Table 1, injecting larger proppant size leads to higher productivity index, for intermediate shale matrix permeability, i.e., 1 μD < K <100 μD, injecting larger proppant size leads to higher productivity index, however, the productivity index is not sensitive to wide range of proppant sizes and for proppant size larger than 0.5 mm the productivity index decreases. In tight formations, i.e. k<1 μD, critical proppant size exist that can lead to maximum stimulation efficiency, for the set of parameters presented in table 1 the optimum proppant size turned out to be 0.2 mm. Unlike high permeability formations increasing the proppant size larger than the critical proppant size leads to decrease in productivity index and reduces the stimulation performance efficiency. The impact of optimum proppant size selection on stimulation performance pronounced in lower permeability formations such as Marcellus shale gas reservoir.

Table 7 - Base case parameters

Relative density	2.08
Proppant size	0.2 mm
Reservoir permeability	1 mD
Prop volume	0.7
Fluid viscosity	1 cp
Fracture width	0.017 ft
Injection rate	0.2 ft/s

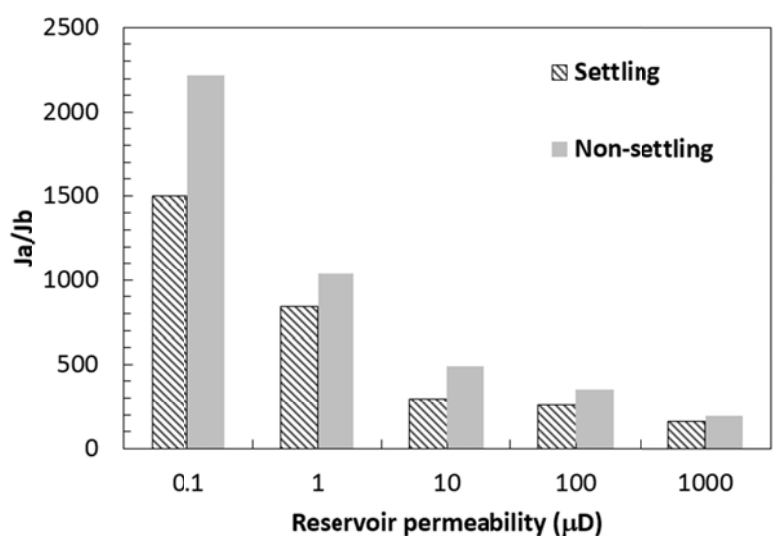

Figure 54 - Influence of proppant settling on dimensionless productivity index, the proppant size is 0.8mm

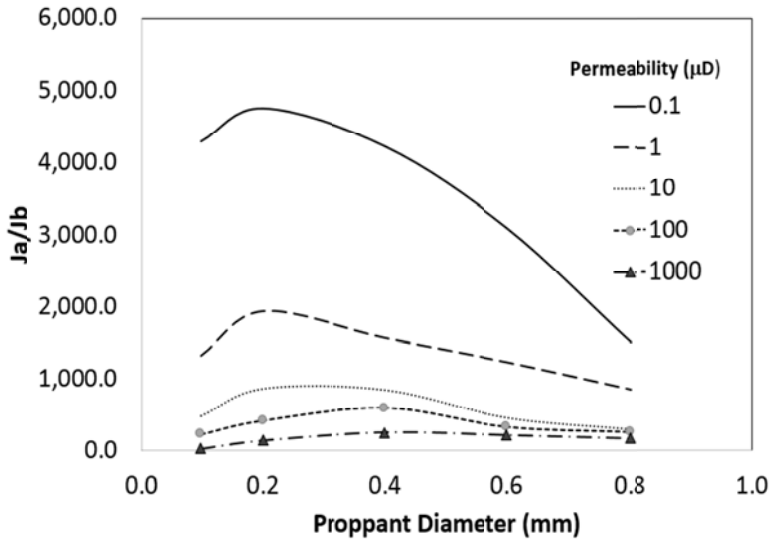

Figure 55 - The effect of proppant size on dimensionless productivity for different permeability reservoir

In the industry sand and resin coated sand with density of 2.65 gr/cc is commonly used. Recently new application of Ultra-lightweight proppant (1.25 gr/cc) resin-impregnated and coated nut hull, ultra-lightwight plastic composite proppant (1.5 gr/cc),light weighted ceramic, intermediate density ceramic and high density ceramic, (2.72 gr/cc, 3.27 gr/cc, and 3.56 gr/cc) is also suggested [19]. **Error! Reference source not found.** shows the impact of the relative density of proppant to fluid on stimulation performance analysis. As relative density of the proppants increases, settling velocity increases that leads to early proppant bank accumulation and decrease in propped area. This consequently decreases the stimulation performance. **Error! Reference source not found.** also shows much higher stimulation efficiency drop in tighter formations such as shale gas reservoirs as a function of relative proppant density.

Error! Reference source not found. shows the impact of Non-Darcian flow in stimulation performance analysis. Ignoring the Non-Darcy effect in simulation results in 4.5% overestimation of stimulation performance. The effect is more pronounced in higher matrix permeability formations as expected.

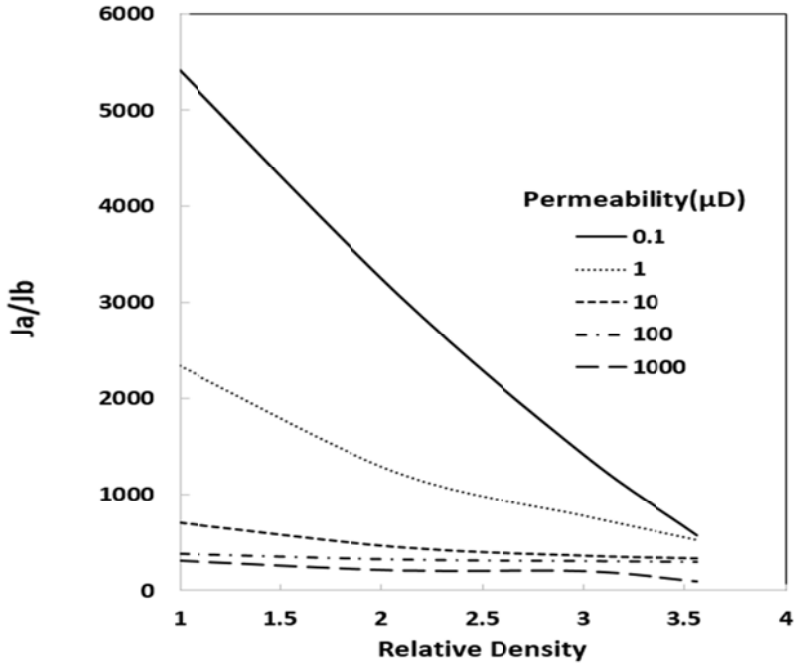

Figure 56 - The effect of relative proppant density on dimensionless productivity for different permeability reservoir

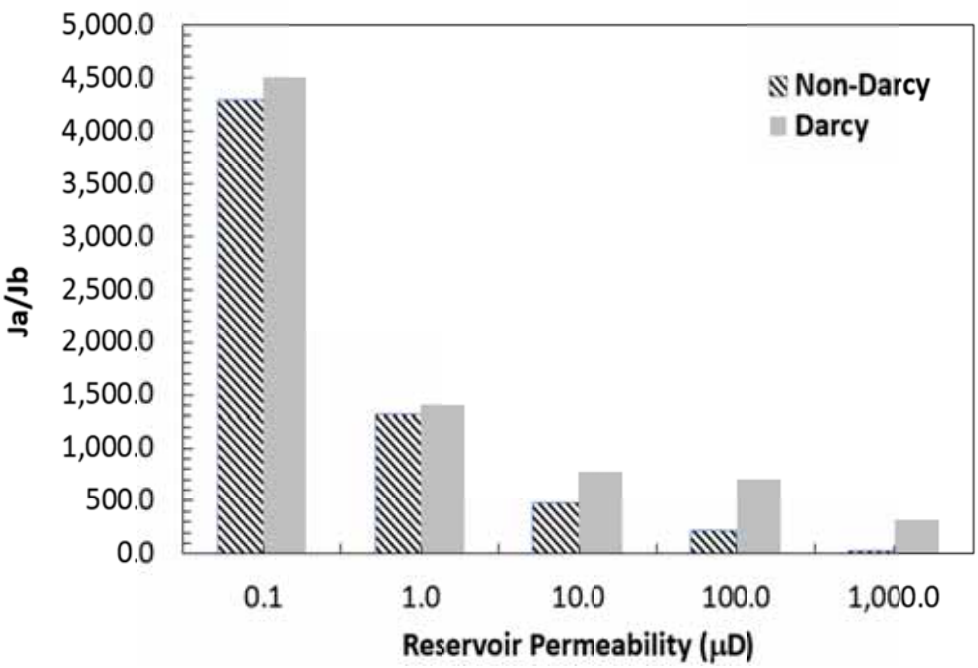

Figure 57 - Influence of Non-Darcy effect on dimensionless productivity index

4.2 Proppant Size Combination Optimization

Multi size proppant combination can maintain relatively large fracture area as well as high fracture permeability in the near wellbore region. In this section, different proppant combinations, i.e., different volume portion, relative proppant density and different proppant size combinations are simulated and their performance is compared with each other. The reservoir permeability is 0.01 μD and the smaller proppant size is 0.2mm. A series of different larger proppant sizes and its volume portion are simulated. The results are shown in **Error! Reference source not found.** a, b and c. Simulation results show that larger size of the later injected proppant leads to a better performance as long as relative density of proppant are in the range of light to intermediate. However in the case of high density ceramics larger proppant size leads to lower hydraulic fracturing performance. Also, there exist an optimum volume portion for the later injected proppant in the range of light to intermediate proppant density, and the portion is about 10% to 15% depending on the proppant size.

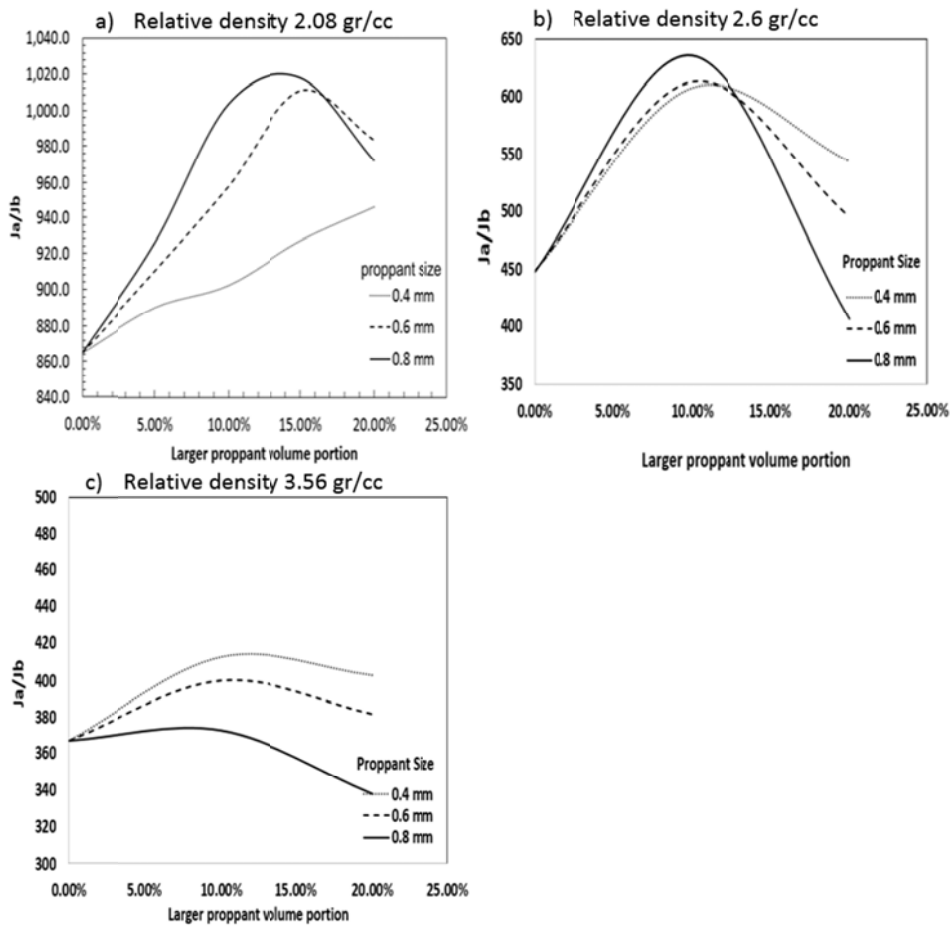

Figure 58 - The effect of proppant size and volume portion combination on dimensionless productivity

4.3 Uncertainty Analysis Using Design of Experiments

For real field application of stimulation performance analysis, one needs to consider the uncertainty analysis and risk assessment using wide range of model variables impacting the process. Due to the fact that different parameters like reservoir permeability, and mechanical properties, proppant size, volume and density, injection rate and fluid viscosity contribute to the hydraulic fracture performance, it is very

hard quantify the impact of each one of these parameters using simple one variable at a time studies (OVAT). This is due to correlations exist between different parameters impacting the hydraulic fracturing performance. In this study Plackett-Burman (PB) experiment technique is used to quantify the contribution of each candidate parameters and their interactions on hydraulic fracturing stimulation. The PB design settings are listed in **Error! Reference source not found.** and **Error! Reference source not found.**3 [25]. The PB design is the most compact two-level design of resolution of III. Resolution III design does confound main effects with two-factor interactions, i.e., all main effects can be determined [10]. In Table 2 and 3, minimum and maximum values assigned to 7 different parameters expected to have the highest impact on hydraulic fracturing performance is presented with -1 and +1 values, respectively. In general, PB requires (n+1) runs, where "*n*" is the number of variables but they are usually in multiples of 4.

Table 8 - Parameter setting of PB design

Parameter	-1	1	unit
A:Fluid viscosity	1	10	cp
B:Proppant size	0.1	2	mm
C:Relative density	1.5	3.5	1
D:Injection rate	0.2	1	ft/s
E:Fracture width	0.017	0.2	ft
F:Permeability	0.1	100	mD
G:Prop volume	0.45	0.9	1

Table 9 - PB matrix for 7 variables (-1 = low value, +1 = high value)

	Factor 1	Factor 2	Factor 3	Factor 4	Factor 5	Factor 6	Factor 7	Response
Run	A:Fluid viscosity	B:Proppant size	C:Relative density	D:Injection rate	E:Fracture width	F:Permeability	G:Prop volume	Dimensionless PI
	cp	mm	1	s	in	D		
1	1	1	-1	1	1	-1	1	2.11E+02
2	1	1	1	-1	1	1	-1	4.15E+01
3	1	1	-1	1	-1	-1	-1	2.07E+02
4	-1	1	-1	-1	-1	1	1	1.01E+02
5	1	-1	1	-1	-1	-1	1	4.14E+02
6	1	-1	1	1	-1	1	-1	2.69E+01
7	-1	1	1	-1	1	-1	-1	2.57E+02
8	-1	1	1	1	-1	1	1	9.02E+01
9	-1	-1	-1	-1	-1	-1	-1	2.66E+02
10	-1	-1	-1	1	1	1	-1	2.72E+01
11	1	-1	-1	-1	1	1	1	2.77E+01
12	-1	-1	1	1	1	-1	1	4.12E+02

In this research, Pareto chart, and normal plot of the standardized effects will be used for uncertainty analysis. Figure 59 shows reservoir permeability, proppant volume and proppant density have significant influence on the dimensionless productivity index while proppant size, fluid viscosity, injection rate and

fracture width having less impact. However, one needs to consider the fact that PB design is not fully considering the two-factor interactions. In the normal probability plot of the effects Figure 60, points that do not fall near the line usually indicate important effects. Important effects are larger and generally further from the fitted line than unimportant effects. Unimportant effects tend to be smaller and centered on zero, these are in agreement with Figure 59. Also, normal plot can identify the effect polarity of each variable. For example, the standard effect of reservoir permeability is negative, which means small permeability reservoir tend to have better improvement from hydraulic fracturing treatment. Figure 60 clearly shows that reservoir matrix permeability has the highest negative impact on simulation response and prop volume and then relative density of proppant to fracturing fluid has the highest positive impact on dimensionless productivity index. The alias structure of PB design is complex [10]. All main effects have two-factor, three-factor and more interaction alias chains. To minimize the error, we also performed full fold-over design to eliminate the entire two-factor interaction alias from main effects.

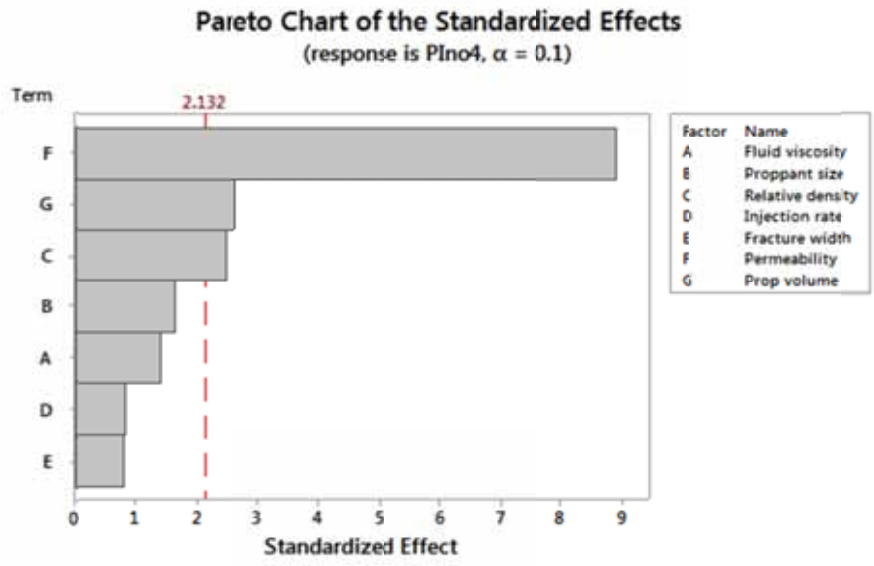

Figure 59 Pareto chart shows the importance of parameters evaluated on the t-value of original case

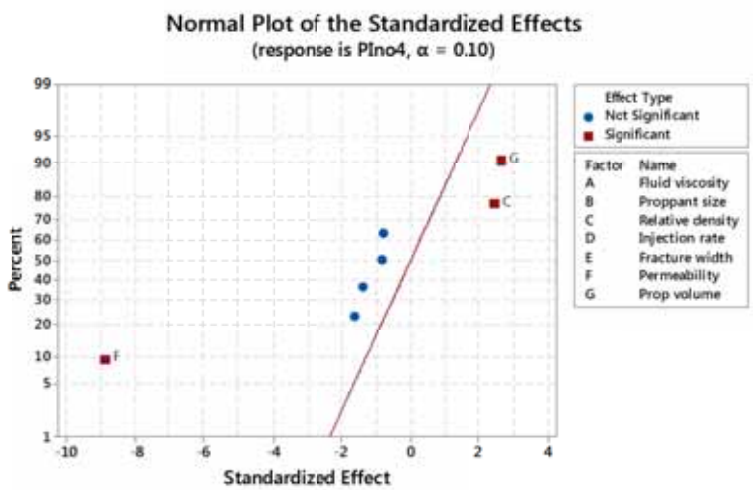

Figure 60 Normal plot of the standardized effects of original case shows the importance of parameters

Conclusion

Unified 3-D numerical simulator is developed using Fortran 90 including three major parts: hydraulic fracture propagation model, fluid and proppant transport, hydraulic fracture geometry calculation after flow back and hydraulic fractured gas reservoir production. In this study different parameters impacting proppant-settling velocity such as non-Newtonian flow, fracture width, fracture leak-off, proppant volume, relative density, size and concentration effects are considered. In addition, sensitivity analysis is implemented to evaluate the impact of different controllable and uncontrollable parameters on dimensionless productivity index. Design of experiment technique (PB) is used to identify the magnitude and statistical significance of most important parameters impacting hydraulic fracturing stimulation.

3.5. Characterization of Stresses

A single fracture is used in order to establish a baseline for study of congruent fracture stress relation. The relationship of stress surrounding a single fracture will identify to its corresponding properties of injection rate and surrounding geomechanical properties. Therefore in future scenarios, under identical conditions, as the number of fractures is increase their effect upon the relative stress variation can be seen. An outline of the sensitivity cases can be seen in **Table 10**.

Single Fracture at 0.00005 Injection				
Cases	Fracture Spacing	Injection Rate	Modulus of Elasticity	Poisson's Ratio
1	N/A, single	0.00005	150	0.2
2	N/A, single	0.00005	170	0.2
3	N/A, single	0.00005	190	0.2
4	N/A, single	0.00005	170	0.1
5	N/A, single	0.00005	170	0.2

6	N/A, single	0.00005	170	0.3

Table 10 Single Fracture Sensitivity

The figures below identify the effects of the major geomechanical properties on fracture length and width. These properties include the elastic modulus of the reservoir, corresponding to its ability to resist deformation and Poisson's ratio. There were a total of 6 cases run in order to establish their respective relationships.

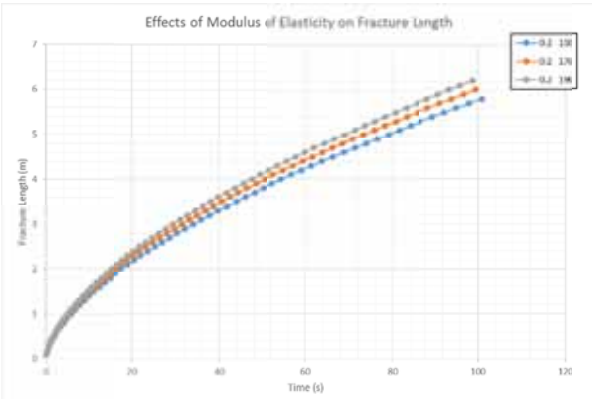

Figure 61 Elastic Modulus Effect on Fracture Length

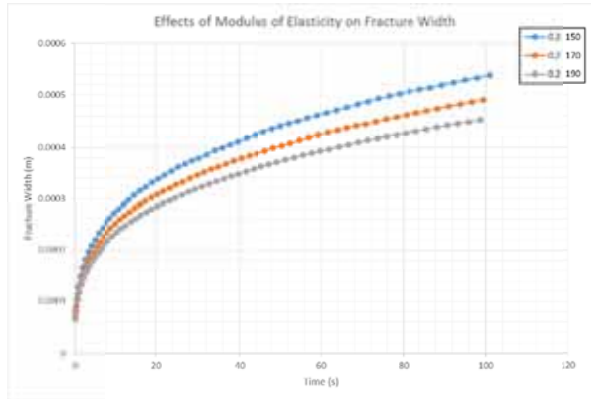

Figure 62 Elastic Modulus Effect on Fracture Width

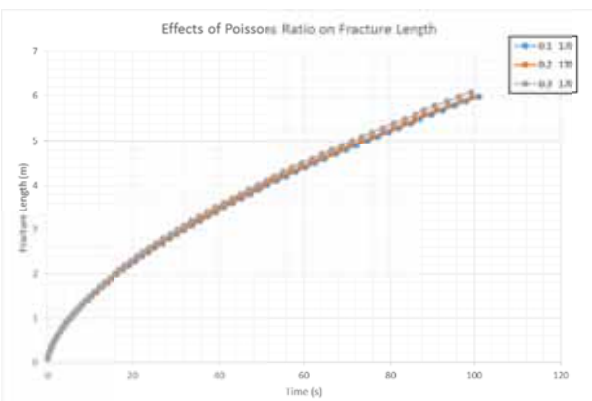

Figure 63 Poisson Ratio Effect on Fracture Length

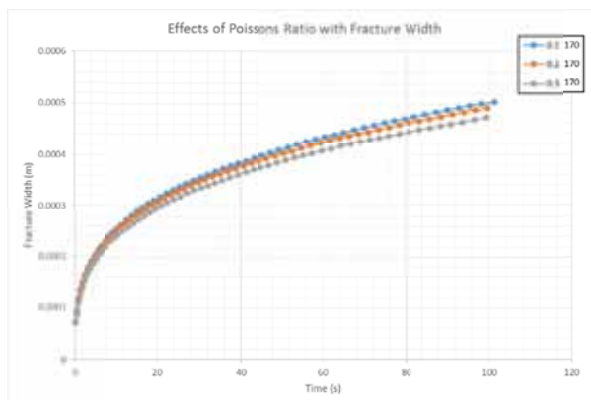

Figure 64 Poisson Ratio Effect on Fracture Width

The figures above indicate the sensitivity of associated geomechanical properties on fracture width and length through time. In this comparison the results were determined over equal time periods for each solution which was predefined at 100 seconds of injection at an injection rate of 0.00005 m^2/s. These results indicate that the fracture geometry, as expected is much more sensitive to variations in the materials elastic modulus than that of Poisson's ratio.

Fracture Length

The maximum rate of change seen in fracture length was 9.71% with an average of 7.78% as the elastic modulus was decreased from 170k to 150k. The maximum rate seen with an increase in elastic modulus from 170k to 190k was 8.85% with an average of 7.10%. In comparison, the maximum rate of change seen when increasing Poisson's ratio from 0.2 to 0.3 was 4.2% with an average of 3.35%. The maximum

rate of change seen when decreasing Poisson's ratio from 0.2 to 0.1 was 2.51% with an average of 1.82%.

Fracture Width

The maximum rate of change seen in fracture width was 4.00% with an average of 3.38% as the elastic modulus was decreased from 170k to 150k. The maximum rate seen with an increase in elastic modulus from 170k to 190k was 3.48% with an average of 2.95%. In comparison, the maximum rate of change seen when increasing Poisson's ratio from 0.2 to 0.3 was 1.73% with an average of 1.43%. Decreasing Poisson's ratio from 0.2 to 0.1 saw a maximum rate of change of 1.00% with an average of 0.84%.

These results clearly indicate that the modulus of elasticity has the greatest impact upon both fracture length as well as width. Furthermore, the largest rate change in both length and width with respect to Poisson's ratio were seen as it was increased. On the other hand, the largest rate change for both length and width with respect to elastic modulus were seen as it was decreased. This depicts a positive correlation between rate changes for length and width but their response is inversed between changes in Poisson's ratio and modulus of elasticity. This correlation was similarly observed using an injection rate 10 fold of that depicted here however the fracture width was much less influenced due to the high rate of injection.

The figures below depict the illustration of fractures in the reservoir for a single fracture case and for a multiple, or three fracture case. In the case of two parallel fractures, the center fracture is removed from the three fracture illustration and they will lie equidistant from the centerline of the reservoir.

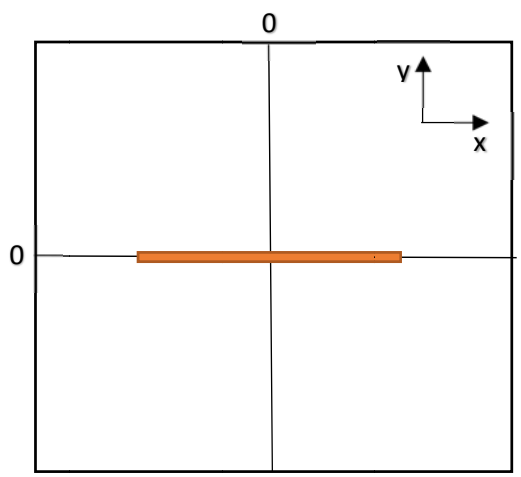

Figure 65 Illustration of Expected Single Fracture

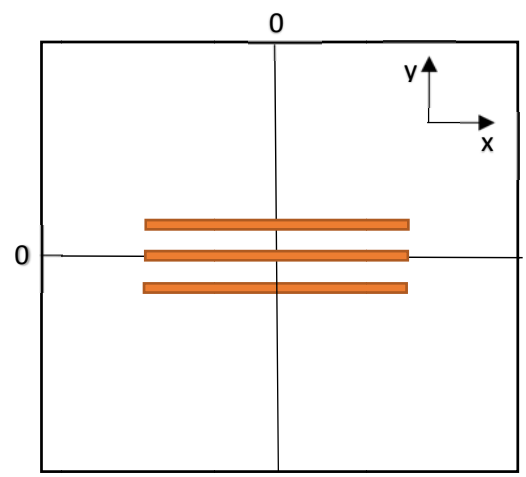

Figure 66 Illustration of expected Multiple Fractures

Table 11 - Reservoir properties

Poisson's ratio	0.20
Young's modulus	17,000,000
Injection rate	0.0005
Injection rate division	0.3333
Leak-off rate	1.47e-5
Fracture spacing	5 m

In the case of three congruent fractures using an equivalent spacing of 5 meters and a uniform volume injection rate of 0.0005 m/s^2 divided between the three fractures. These figures to the left below displays the horizontal stress distribution along the x-axis at a snapshot taken at 45 seconds. This displays a concentration of stress at the fracture tips of the offset fractures. The centric fracture displays an interaction with the offset fractures in both direction and magnitude of stresses along with an alteration of fracture geometry. The figure below to the right displays the horizontal stress distribution along the y-axis. This displays a stress concentration at the fracture tips that is mirrored around the central fracture where a maximum is observed, again both magnitude and direction of stresses are influenced by this central fracture.

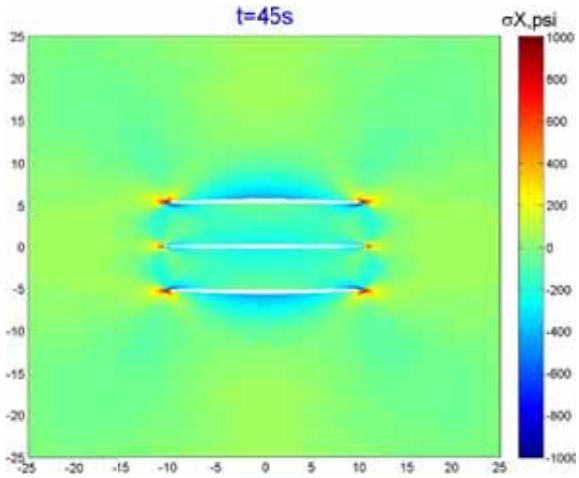

Figure 67 Stress Change in the X-Direction

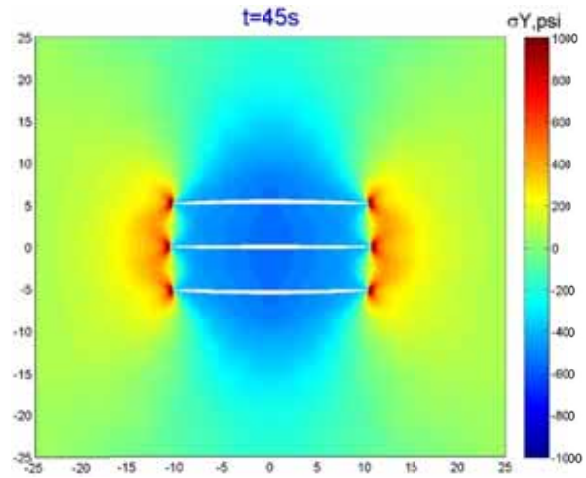

Figure 68 Stress Change in the Y-Direction

The fracture geometry is affected by the spacing of the offset fractures and the relative stress magnitudes that are seen around the developing fracture. Under equidistant spacing and injection rates the fracture geometry is mirrored around the central fracture location. Assuming that each fracture is undergoing injection at the same time then the central fracture begins to trade width for length in comparison to the two offset fractures.

The most effective way of analyzing stress distributions for any system is through the principle stress relationships. This is merely a stress transformation which orients the X and Y stress fields, whose vectors may point in any given direction and magnitude along the principle axis. Therefore the shear stress is diminished to zero, as the principle stresses are aligned along the corresponding axis by minimum, maximum and intermediate values in three dimensional analyses. In two dimensional analyses the third principle stress is dependent upon the analytical solution of plane strain or stress. The Von Mises stress is an important criteria selected for this research as it exemplifies the entire stress field with only a single consolidated value.

The changes in horizontal stress can be interpreted from the resultant values of the simulation through the solution time. In order to see the effects of these stress relationships, the stress values are interpolated over a cross-sectional and a profile cross-section of the reservoir domain at specified locations, as seen below in **Figure 65**. These locations are plotted at the intersection of the injection point as well as at an offset location that is determined by the number of fractures and the fracture spacing, if applicable. In the case of multiple fractures, the profile will always be plotted against the

uppermost fracture. In order to see cross-sectional and profile views intersecting at the center of the reservoir then please refer to **Appendix 8.4 Figures**.

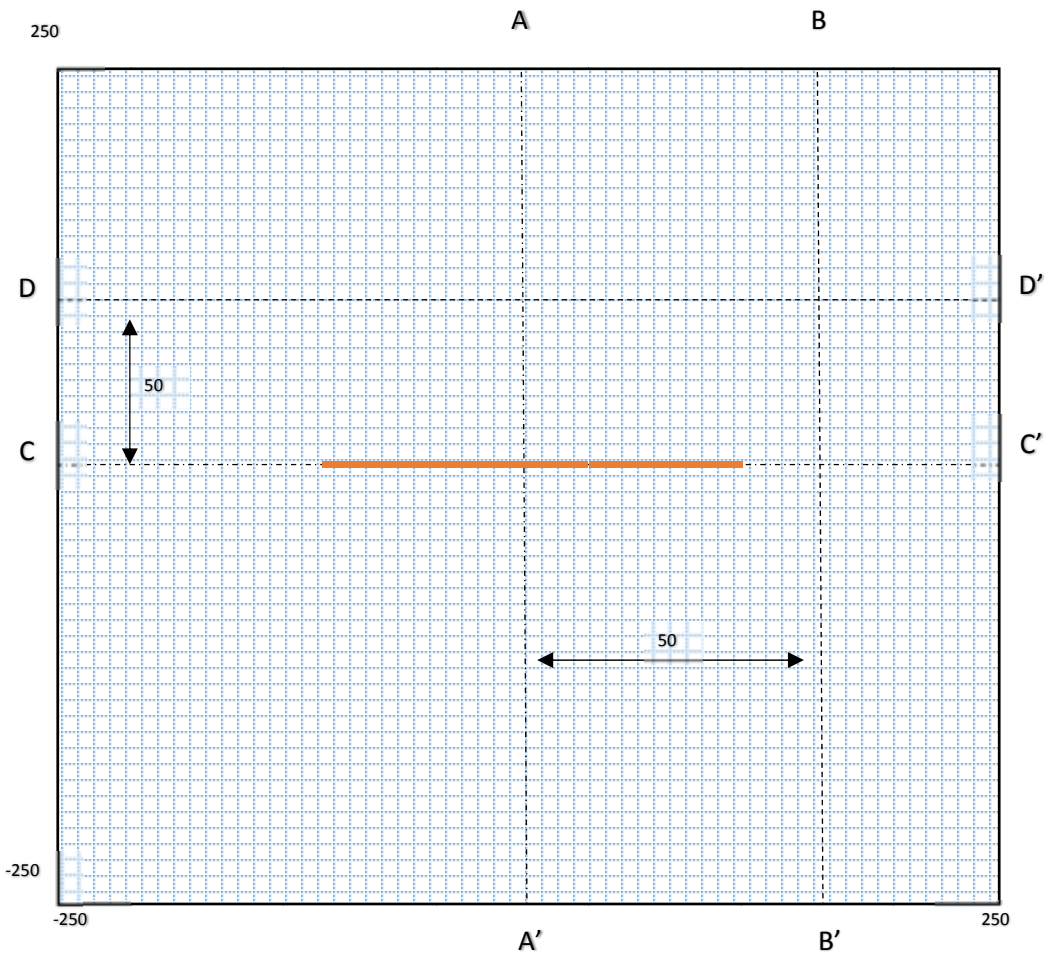

Figure 69 Illustration of Line Locations for Stress-Change Plots

Figure 65 represents the line locations at which stresses will be plotted. The lines A – A' and B – B' run North to South and represent the cross-sectional plots running perpendicular to the fracture at the point of injection and at a specified distance 50 meters from the point of injection. The lines C – C' and D – D' which run East to West represent the profile plots of the stress and stress relationships which are running parallel to the fracture. In order to visualize these stress transformations, the stresses will be displayed at single time steps as well as for the rate of change in order to determine the general static and dynamic response which surrounds fracture propagation and the redistribution of stress.

Single Fracture Case

The following three figures of **Figure 70 (a)** σ_x, **(b)** σ_y, and **(c)** τ_{xy} represent the stress distributions at the injection point and at distance of 50 meters from the injection point. This is for a single fracture that has been injected at a constant injection rate of 0.0005 m/s. These figures represent the cross-sectional view of the reservoir at lines A – A' (green) and B – B' (blue) shown in **Figure 69**. As one would expect,

the stress change seen at the site of injection is much higher than that seen a distance (50 m) from the fracture tip.

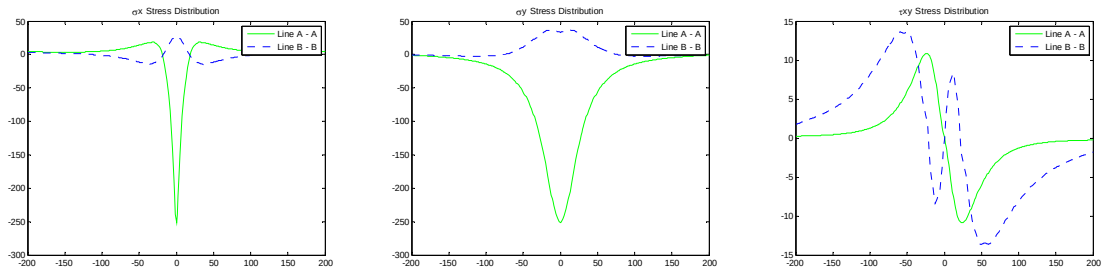

(a) **(b)** **(c)**

Figure 70 The Static Component Stress Distribution Surrounding a Single Fracture, t=60s

These figures of **Figure 71 (a)** σ_1, **(b)** σ_2, and **(c)** σ_{vm}represent the consolidated component stress distributions surrounding the fracture at the injection site and at a distance 50 meters from the injection site. The first two **Figure 71 (a)** and **(b)** represent the principle stresses in two-dimensions, that is the maximum and minimum. The third **Figure 71 (c)** is representative of the Von Mises stress distribution. These represent the stress transformation of the component stress tensors shown independently in **Figure 70**. This information is useful in deciphering the interactions in comparison with the component stresses. Their appearances seem to simply be rearranged between the diagrams but they provide useful insight to other applications. The Von Mises is reflective of all the stress contributions and therefore lends insight to the dominant stresses. A different relationship can clearly be seen in the peak of the Von Mises stress which displays the transition between the dominant stress components.

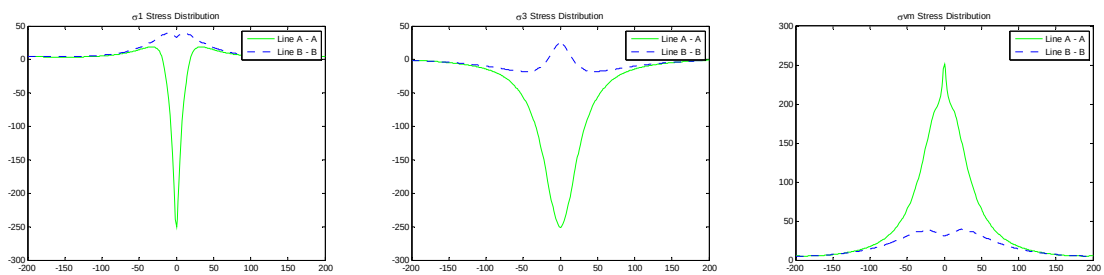

(a) **(b)** **(c)**

Figure 71 The Static Principle Stress Distribution Surrounding a Single Fracture, t=60s

Figure 72 represents the profile of the fracture with respect to the component stresses. These figures **(a)** σ_x, **(b)** σ_y, and **(c)** τ_{xy} are shown with respect to the profile reservoir cross-sections along lines C – C' (green) and D – D' (blue). These same line location profile plots are shown in **Figure 73 (a)** σ_1, **(b)** σ_3, and **(c)** σ_{VM}

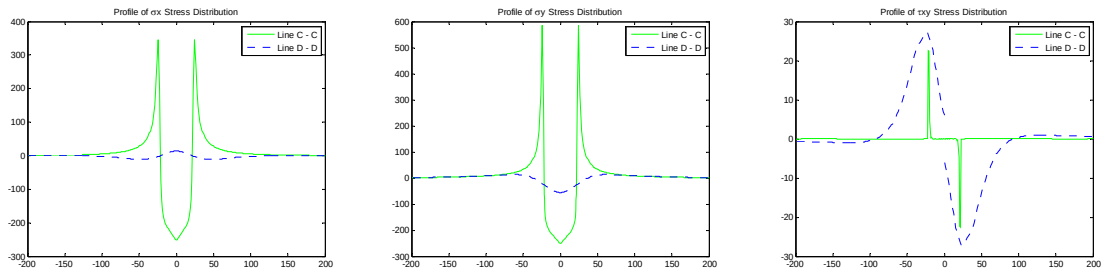

(a) **(b)** **(c)**

Figure 72 The Static Component Stress Profile Surronding a Single Fracture, t=60s

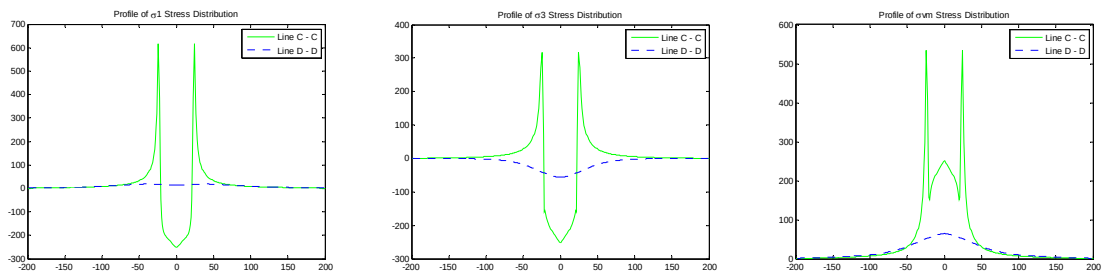

(a) **(b)** **(c)**

Figure 73 The Static Principle Stress Profile Surrounding a Single Fracture, t=60s

The previous figures defined a static snapshot of the stress distribution at two different locations taken at the same instant in time. This is useful for comparison to other similar studies however the transient response is of concern with relation to this investigation. The time dependent behavior of the stress fields are described by **Figure 74 (a)** maximum component stress field variation, **(b)** minimum component stress field variation and **(c)** the maximum principal and Von Mises stress variations. These plots display the maximum or minimum value of stress versus time without regard for distance to or from the fracture or injection point. This identifies the general behavior that is to be seen throughout the period of injection.

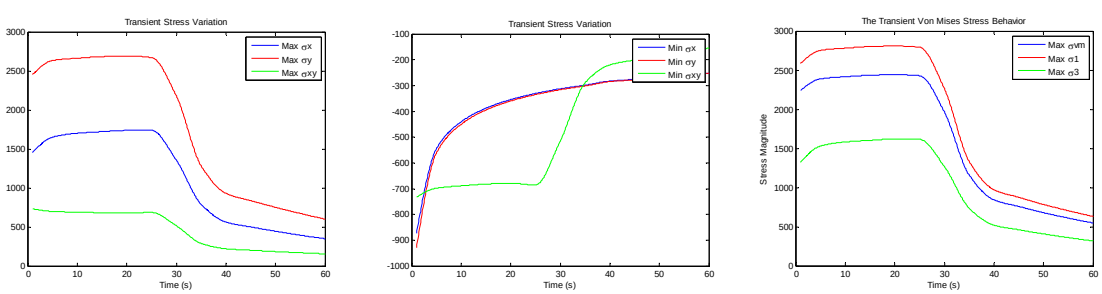

(a) **(b)** **(c)**

Figure 74 The General Transient Behavior of Stress Surrounding a Single Fracture, t=0 to 60s

These **Figure 74 (a)**, **(b)** and **(c)** depict a similar behavior for the component stress distributions through time. The principle and Von Mises stress are also shown to depict a predictable behavior. These

consolidated stresses are shown in order to introduce their behavior and the influence of all the contributing component stresses in order to verify their use in further discussion.

In addition to their predictable behavior(s), a relationship can be seen between the principle stress σ_1 and the Von Mises stress σ_{VM} in **Figure 74 (c)**. This relationship is key to defining the Von Mises stress as an applicable consolidated stress value to this type of problem.

Two Fracture Case

The following three figures represent the stress distributions at a distance of 50 meters from the injection point for a system of two equally injected fractures at a distance of 5 meters spacing. Unlike the single fracture case described in the previous section, the case of two fractures introduces an additional complexity to the stress distributions, as would be expected. These stresses portray themselves in a variety of ways which can be seen below in **Figure 75** where **(a)**, **(b)** and **(c)** are σ_x, σ_y, and τ_{xy} respectively after 60 seconds of injection.

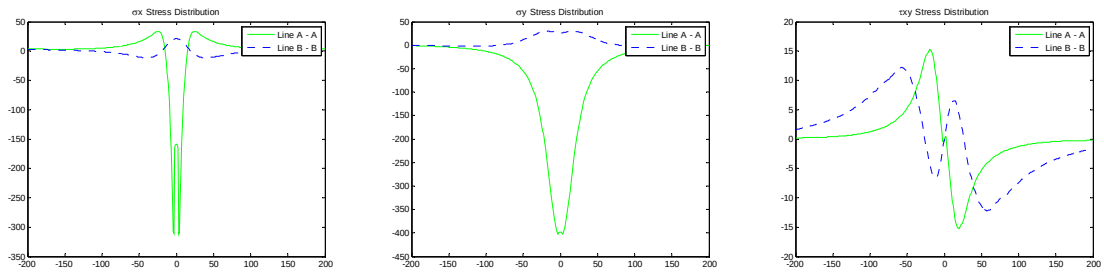

(a) **(b)** **(c)**

Figure 75 The Static Component Stress Behavior Surrounding Dual Fractures at 5 Meters Spacing, t=60s

The static stress distributions are an important step to the classification of these stress interactions as it provides verification of the trend that is seen in similar static case studies but also provides the ability to compare states when adding additional complexities, such as by increasing the number of fractures. The static principle and Von Mises stress distributions are depicted below by **Figure 76**. These figures represent a cross-sectional view of the reservoir and fractures at the lines A – A' (green) and B – B' (blue) after an injection time of 60 seconds. These two cross-sections are again taken at the point of injection and at a distance of 50 meters of the injection site as depicted in **Figure 69**.

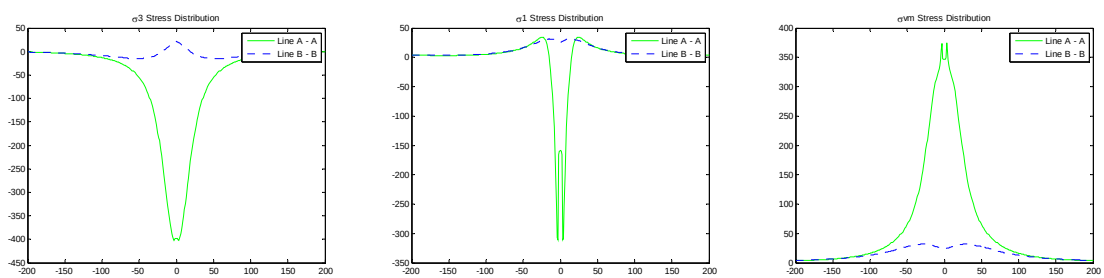

(a) **(b)** **(c)**

Figure 76 The Static Principle Stress Distribution Surrounding Dual Fractures at 5 Meters Spacing, t=60s

The following **Figure 77** represents a profile view of the stress distribution along the outermost fracture where **(a)** is σ_x, **(b)** is σ_y, and **(c)** τ_{xy} at a time of 60 seconds after injection. This is to say that this profile is 2.5 meters from the reservoir centerline and 5 meters from the second fracture. These lines represent that of C – C' and D – D' as described in **Figure 69**. This same process is repeated for the corresponding principle stresses of σ_1, σ_2, and σ_{VM} in **Figure 78 (a)**, **(b)**, and **(c)**.

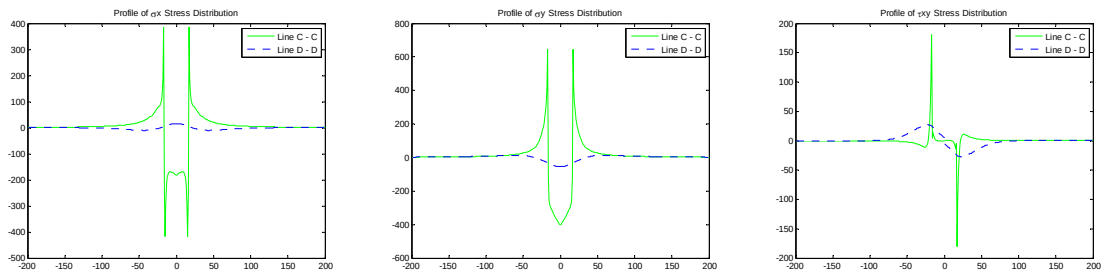

(a) **(b)** **(c)**

Figure 77 The Static Component Stress Profile Along the Outermost Fracture in a Dual Fracture System at 5 Meters Spacing, t=60s

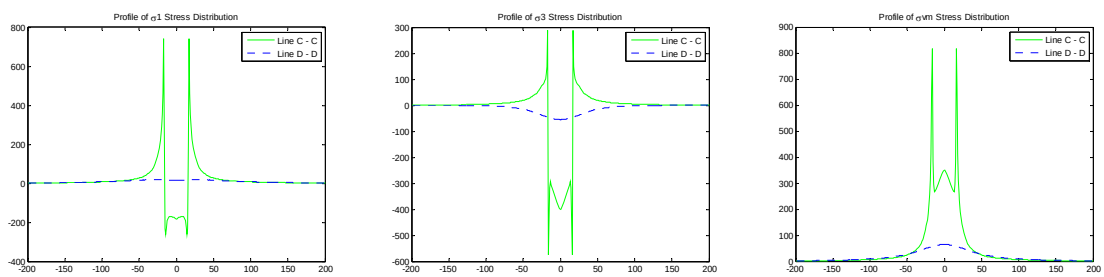

(a) **(b)** **(c)**

Figure 78 The Static Principle Stress Profile Along the Outermost Fracture in a Dual Fracture System at 5 Meters Spacing, t=60s

Figure 79 is representative of the profile at the reservoir centerline. It is not along the profile of a fracture but simply taken at the center of the reservoir, therefore it lies 2.5 meters from both fractures. These figures **(a)**, **(b)** and **(c)** are of σ_x, σ_y, and τ_{xy} respectively.

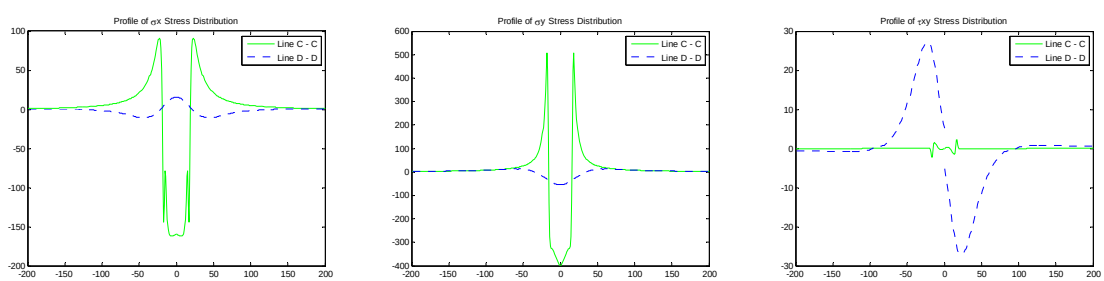

(a) **(b)** **(c)**

Figure 79 The Static Component Stress Profile Along the Reservoir Centerline Between Dual Fractures at 5 Meters Spacing, t=60s

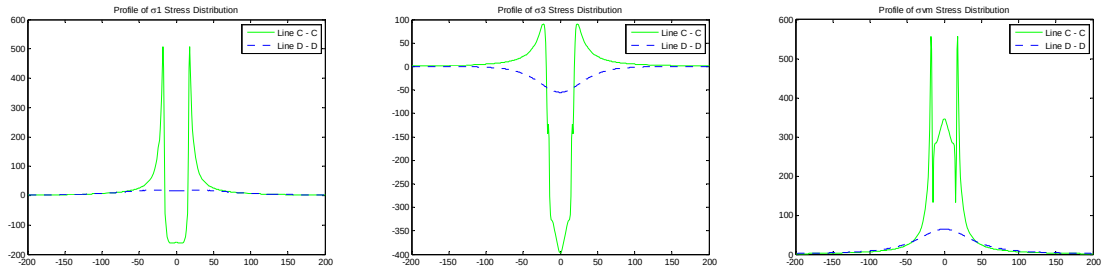

(a) **(b)** **(c)**

Figure 80 The Static Principle Stress Profile Along the Reservoir Centerline Between Dual Fractures at 5 Meters Spacing, t=60s

The transient response of the stresses is of the most concern with respect to this type of research as these have rarely been fully explored. These stresses are often viewed for static cases and do not analyze the representative patterns as they develop. In the case of two fractures the transient stress response can be seen in **Figure 81 (a)** the maximum component stresses, **(b)** the minimum component stresses, and **(c)** the maximum principle and Von Mises stresses where the development of these profiles can be used to infer some of these interactions.

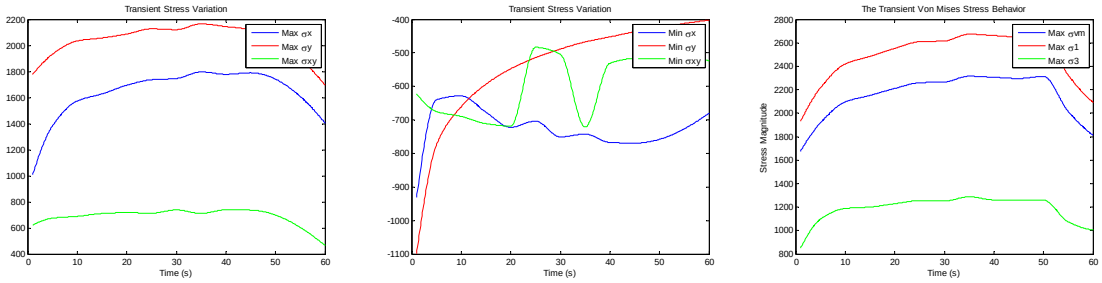

(a) **(b)** **(c)**

Figure 81 The General Transient Behavior of Stress Surrounding Dual Fractures at 5 Meters Spacing, t=0 to 60s

Three Fracture Case

The following three figures represent the stress distributions at a distance of 50 meters from the injection point for a system of three equally injected fractures at a distance of 5 meters spacing. Unlike the single fracture case described in **Figure 70** the case of three fractures brings another layer of complexity to the stress distributions. The following **Figure 82 (a)**, **(b)**, and **(c)** represent σ_x, σ_y, and τ_{xy} respectively which are taken at the cross-sectional lines A – A' (green) and B – B' (blue) at the injection point and at a distance 50 meters from the injection point.

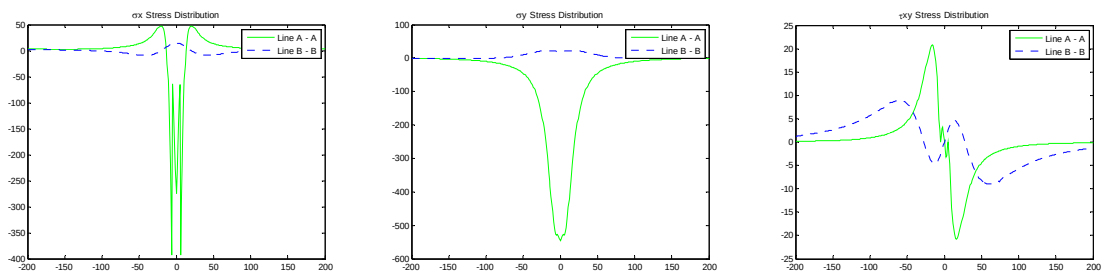

(a) **(b)** **(c)**

Figure 82 The Static Stress Distribution Surrounding a System of Three Fractures at 5 Meter Spacing, t=40s

Again, unlike the single fracture cases where the surrounding stress fields are only representative of the lone fracture(s) interaction with the surrounding media, multiple fractures are further influenced of the surrounding stress magnitude by the introduction of additional fractures. Typically the stresses that are incurred surrounding in the x-direction off of the fracture tips generate the larger stress magnitude. At this spacing of 5 meters it can be seen that the maximum stress magnitude is dominated by the y-direction stress due to the proximity of the fractures interacting causing a stress magnification.

Figure 83 below illustrates the principle stress distribution of the component stress shown in **Figure 82** above. These are again plotted over the cross-sectional lines of A – A' (green) and B – B' (blue) at the site of injection and at a distance of 50 meters from the site of injection.

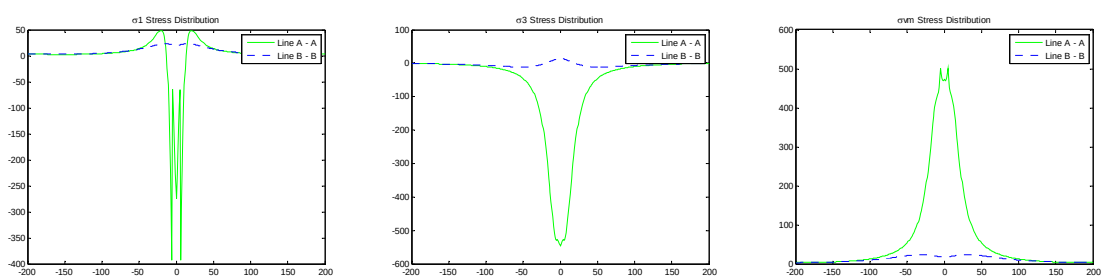

(a) **(b)** **(c)**

Figure 83 The Static Principle Stress Distribution SUrrounding Three Fractures at 5 Meter Spacing, t=40s

The next figures are representative of the profile stress distributions along the length of the fracture(s) and beyond. **Figure 84** illustrates the static stress profile along the outermost fracture in a three fracture system where **(a)**, **(b)** and **(c)** are representative of σ_x, σ_y, and τ_{xy} respectively along the profile lines C – C' (green) and D – D' (blue) at a time of 40 seconds.

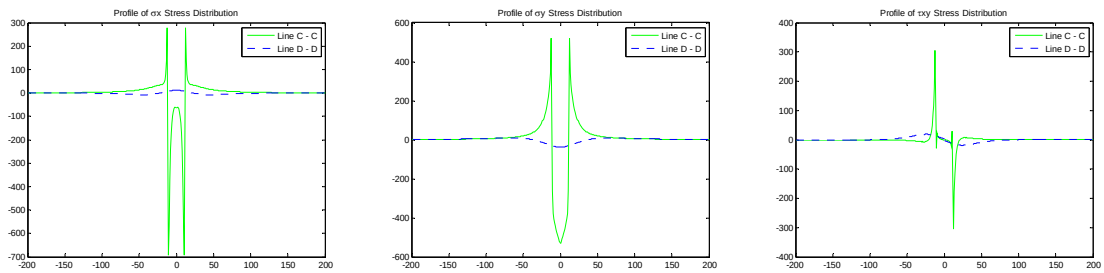

(a) **(b)** **(c)**

Figure 84 The Static Component Stress Profile Along the Outermost Fracture in a Three Fracture System at 5 Meters Spacing, t=40s

The next figures are representative of the profile stress distributions along the length of the fracture(s) and beyond. **Figure 85** illustrates the static stress profile along the outermost fracture in a three fracture system where **(a)**, **(b)** and **(c)** are representative of σ_1, σ_2, and σ_{VM} respectively along the profile lines C – C' (green) and D – D' (blue) at a time of 40 seconds.

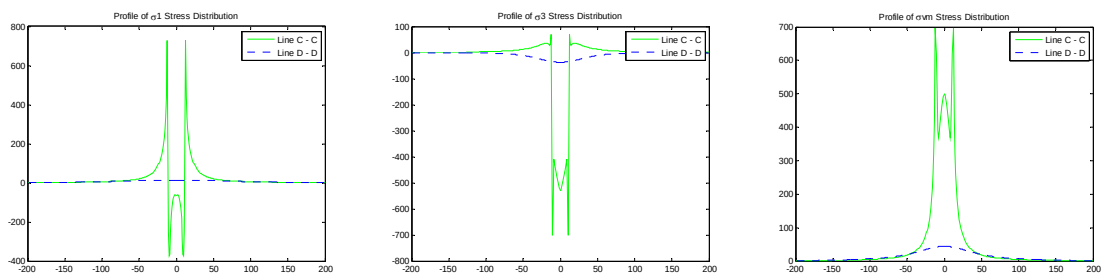

(a) **(b)** **(c)**

Figure 85 The Static Principle Stress Profile Along the Outermost Fracture in a Three Fracture System at 5 Meters Spacing, t=40s

The following displays the component stress profile at the central fracture location; therefore it lies at the center of the reservoir and at the center of the two outlying fractures, both 5 meters away. **Figure 86 (a)**, **(b)**, and **(c)** correspond to the component stresses are σ_x, σ_y, and τ_{xy} at a time of 40 seconds. At the same locations the corresponding principle and Von Mises stresses are depicted in **Figure 87** at the same solution time.

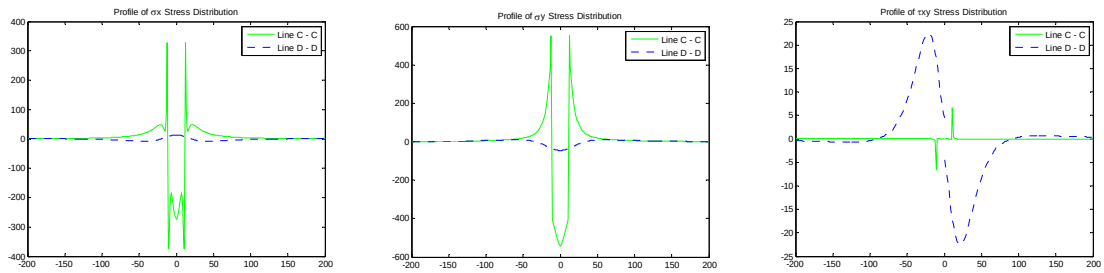

(a) **(b)** **(c)**

Figure 86 The Static Component Stress Profile Along the Center Fracture In A Three Fracture System at 5 Meters Spacing, t=40s

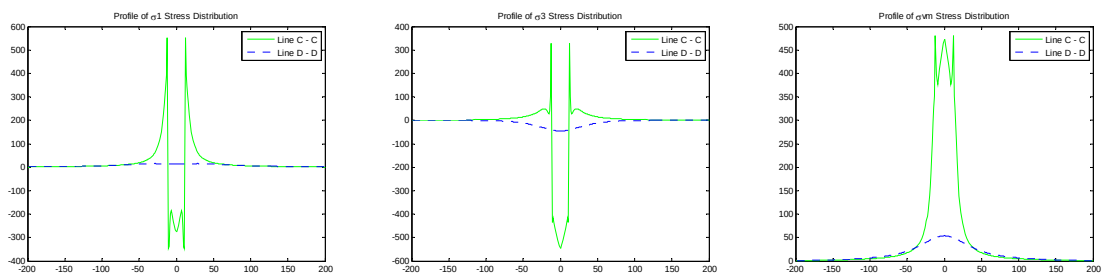

(a) **(b)** **(c)**

Figure 87 The Static Principle Stress Profile Along the Center Fracture in a Three Fracture System at 5 Meters Spacing, t=40s

The change in the principal stresses is displayed in **Figure 88 (a)** dynamic profile of maximum principle stress and **(b)** dynamic profile of minimum principle stress, in order to observe the changes that occur throughout fracture propagation and verify whether the assumptions that are made in static models can be justified which were found in (Cheng, 2012). Although both of these profiles are similar, their relationship is seen to change dramatically through time in relative and overall stress magnitude. This indicates that the assumption of static models cannot be trusted as it incorrectly skews the depiction of stress towards early stage behavior, at the initial time of injection.

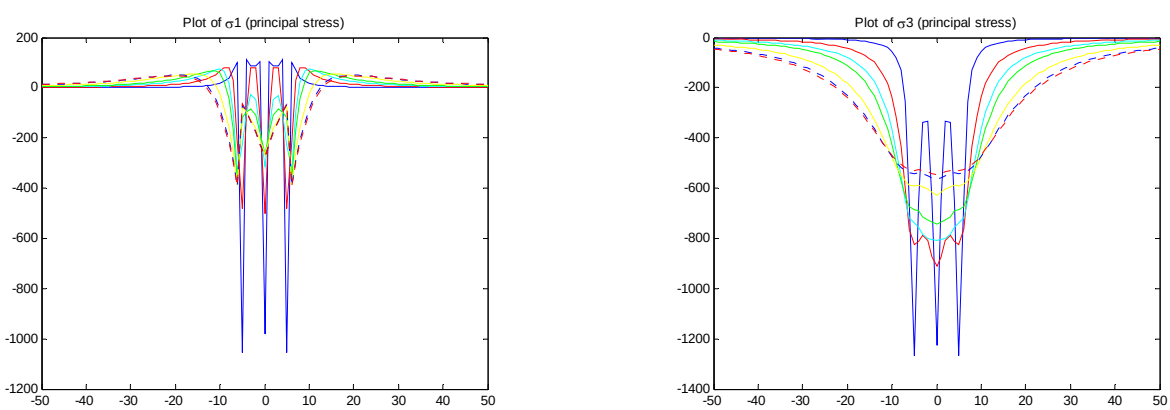

(a) **(b)**

Figure 88 The Dynamic Behavior of the Principle Stresses, t=0 to 60s

The development of the transient response in the three fracture system which is shown below in **Figure 89 (a)** the maximum component stress, **(b)** the minimum component stress, and **(c)** the maximum principle and Von Mises stress. Keep in mind that the length of the simulation is shorter for this cases than that of one and two fractures so the decline in maximum stresses cannot be seen, however they have reached their peak and is expected to follow the same trend as displayed in the previous two examples.

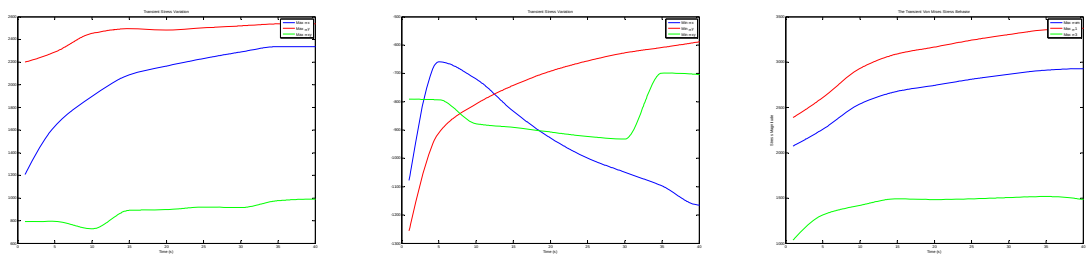

(a) **(b)** **(c)**

Figure 89 The General Transient Behavior of Stress Surrounding the Three Fracture System at 5 Meters Spacing, t=0 to 40s

The Von Mises stress clearly illustrates its behavior with respect to the other stress magnitudes in all three cases. When the stresses are at their maximum value this correlation of the Von Mises to the maximum principle stress displays its greatest difference. During the initial periods of injection and after the fracture interactions have occurred they are much more resembling of each other.

The previous figures throughout this section were used to illustrate the component contributions to the consolidated stresses which in this case are the principle and Von Mises stress. These behaviors offer an insight to the dominating stress influence at any particular time and distance which is critical in establishing dynamic stress relationships. **Figure 90 (a)** indicates the maximum and **(b)** the minimum Von Mises stress with respect to the distance from the fracture tip. This is data is representative of a single fracture after 60 seconds of injection at 0.0005 m/s^2.

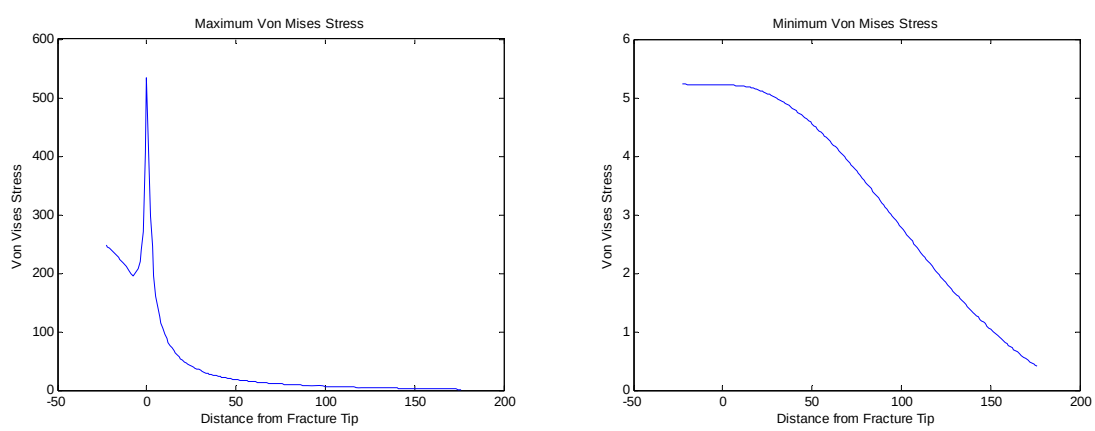

(a) **(b)**

Figure 90 Von Mises Stress with Relation to the Fracture Length and Distanct from the Fracture Tip at t=60s for a Single Fracture

The Von Mises stress is a culmination of the surrounding stress fields such that one value can be used to compare given states of stress. This is particularly useful when you are not so concerned with the direction of the force but the magnitude. This is often why Von Mises is used as a yield criterion. The distance from the fracture tip to the maximum Von Mises stress occurring on each cross-section from the point of injection is plotted in the figure above. Here, the zero is identifying the fracture tip such that the left of zero includes the fracture to the point of injection.

The Von Mises stress is used to identify two distinct patterns that are seen surrounding fracture propagation and associated stresses. There are two distinct sets of behavior for the area trailing the fracture tip and then for the area leading the fracture tip that can be seen in **Figure 91**. At the point of injection the maximum Von Mises stress decline throughout the length of the fracture. As the fracture tip is approached, the maximum Von Mises stress begin to increase sharply to a maximum value which is observed at the tip of the fracture. After the tip of the fracture a secondary behavior is observed leading the fracture tip. In this behavior the maximum Von Mises stress declines rapidly in an exponential manner.

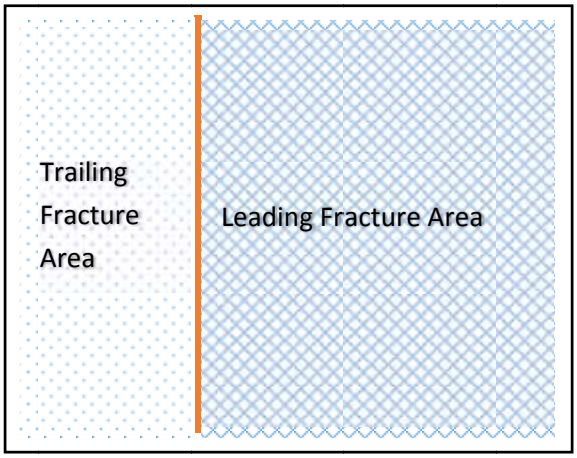

Figure 91 Maximum Von Mises Stress Behavior Surrounding a Single Fracture

This behavior head and tail behavior of the fracture surrounding the fracture tip can be used in order to quantify the data that is observed throughout the stress interactions of the Von Mises stress distributions. The behavior at the head of the fracture for a single fracture is least impacted by the fracture propagation due to the homogenous reservoir properties and constant fluid injection properties. With these values held constant, then the dynamics of the fracture propagation can be limited to the surrounding stress interactions. As one would expect the head of the fracture is least impacted and therefore displays a trend like behavior which can be predicted. This is due to the limited interactions that are occurring ahead of the fracture tip throughout the undisturbed media since the only stress fields are those due to the observed fracture propagation.

The tail behavior of the fracture is more reliant upon the injection parameters and the distance at which the fracture tip extends from the point of injection. This identifies two specific zones within the head and tail of the fracture known as the zones of influence. In the tail of the fracture there is a zone of influence surrounding the point of injection which affects the surrounding stresses, much like the zone of influence surrounding the fracture tip in the head of the fracture. This can be seen in **Figure 87** below.

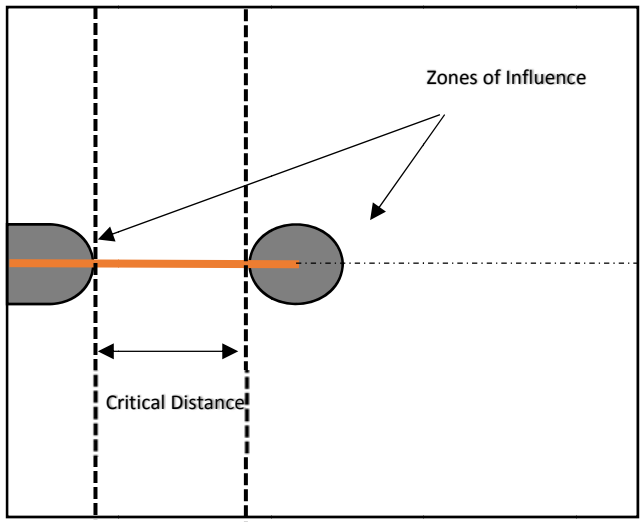

Figure 92 Zones of Influence Surrounding A Single Fracture

The critical distance in question can be observed by evaluating the solution for a single fracture throughout its transient behavior. This identifies the change in distance that is observed which can then be used to establish a critical distance between the injection point and fracture tip with which stress influences are reduced. A single fracture at a single time step is used in order to establish the main points of interest on the Von Mises stress plot.

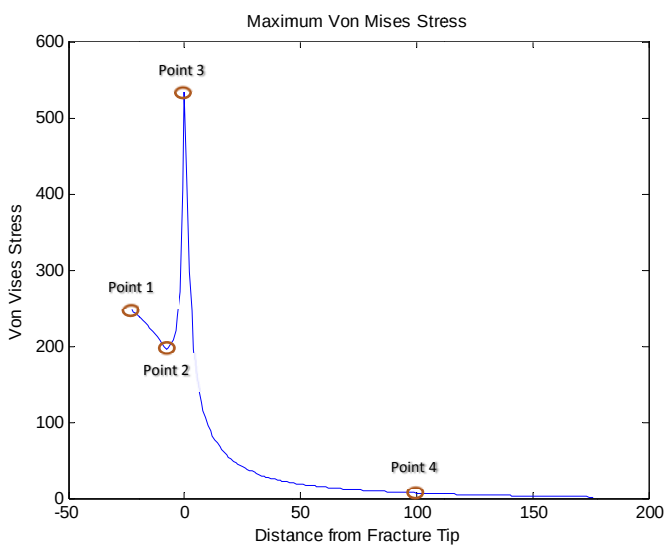

Figure 93 Points of Concern for Static Von Mises Stress Distribution

Point Data for Von Mises Stress in a Single Fracture Case								
Time	Point 1	Von Mises	Point 2	Von Mises	Point 3	Von Mises	Point 4	Von Mises
10	6.49	431.2	2.49	349.2	0	668.7	100	1.67
30	14.24	309.4	5.24	248.2	0	602	100	4.16
45	18.64	273.5	6.64	215.8	0	655.7	100	5.58
60	22.89	248.6	7.89	195.4	0	534	100	6.94
90	30.57	216.8	10.57	169.3	0	369.8	100	9.20
300	68.66	144.9	24.66	108.3	0	231.7	100	16.96
900	125.1	108.8	40.12	77.14	0	247.1	73*	31.43*
1500	172.2	99.35	48.16	67.1	0	254.2	26*	89.22*

Table 12 Point Data for Transient Maximum Von Mises Stress for a Single Fracture Case

Table 12 illustrates the position and magnitude of Von Mises stress along the fracture and surrounding reservoir area at the head of the fracture. The data for points 1 and 2 lie to the left of zero and therefore their absolute value has been shown in the table above. Data point 3 is a zero that is representative of the fracture tip and is shown for reference but has become obsolete now that the absolute values of previous points are used. The data at point 4 is representative of the Von Mises stress at a distance of 100 meters from the head of the fracture tip.

Figure 94 below displays the critical distance that was observed in the interactions of the Von Mises stress. This corresponds to the tail of the fracture behavior where the local minimum was seen versus the length of the propagating fracture. Plotting these distances shows a linear relationship between the distance of the local minimum and the fracture length as the fracture propagates through time. This behavior demonstrates that the Von Mises can be useful in predicting fracture and stress behavior.

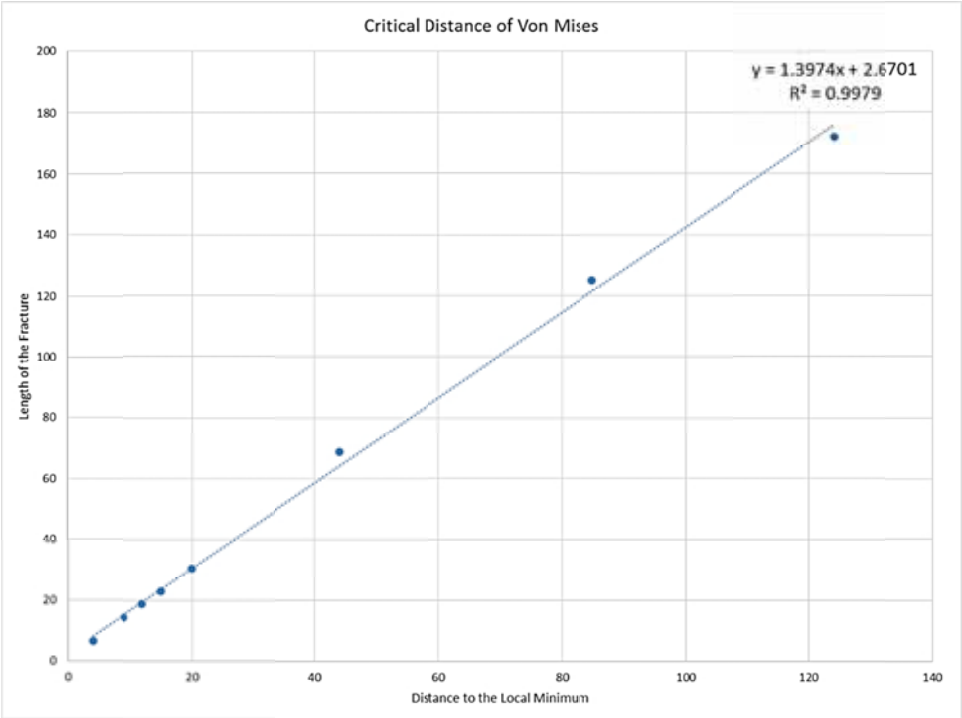

Figure 94 Critical Distance of the Von Mises Stress from the Point of Injection

4. Conclusions

The stress distributions surrounding a fracture have shown to depict a dynamic behavior that differentiates entirely from the standard, static stress case. This becomes significantly important to the study of fracture mechanics in both porous media as well as having application to many other fields of engineering research and design. These dynamic relationships relate specifically to the topic of hydraulic fracturing as it can causes complications with regard to fracture interaction, efficiency and surrounding stability prediction in addition to general fracture predictions.

The behaviors of stresses due to processes such as hydraulic fracturing are often assumed to be constant throughout the injection period however the determination of these stresses is a dynamic process with differing stress characteristics in comparison to static models. The static distribution of stress has been shown to favor the early period of injection just as hydraulic forces are applied to the fracture boundaries. This information also moves to introduce a failure criterion or area of weakened state which is based upon the Von Mises stress, without the requirement of interpreting multiple stress parameters. This will define a critical distance and angle with relation to the fracture(s) dynamic propagation path. This is anticipated to provide insight to fracture interaction and reservoir stability as these results clearly indicate that the Von Mises stress is capable of predicting these behaviors of not only the static interaction surrounding the fracture, but also this dynamic stress behavior which is similar to that of the commonly used principle stress relationships.

The relevancy of these stress fields is not only regarding the surrounding stability but also their direct correlation to fracture propagation of both current and subsequent fractures. The in-situ stress distributions control the immediate response of the fracture propagation, however the dynamic stress fields of these fracture interactions can impede or enhance the subsequent fracture paths. The stresses projected off of the fracture tip display a high increase in the immediate stress fields to the point which they will impact these subsequent fractures and further fracture development. This has been determined both in this thesis and throughout other similar bodies of work however at the time this was the first application of such methodology to the transient behavior of these stresses. The proposed use of the Von Mises stresses is the ability to predict near and far field stress patterns using single consolidated value from which the most efficient stimulation plan may be developed.

The use of varying injection rates gives an insight to the interaction of trailing fracture stresses of the leading fracture impacting the path, direction and magnitude of stresses surrounding subsequent fractures throughout the same injection period. Therefore creating stimulation plans which either mitigates the energy loss occurring from interactions or causing interactions which enhance fracture tip stresses to aid in propagation is an interesting proposition. This is directed at pulsed injection or delayed staging techniques to enhance the quality and efficiency of the treatment zone and in turn increase production from unconventional reservoir formations by thoroughly understanding these dynamic stress variations and using them to our advantage.

The continuation of this type of research is important to furthering our knowledge of geomechanics as well as to increasing the understanding of hydraulic fracture and unconventional reservoir development. Hydraulic fracturing has been crucial to the advancement in the search for energy independence in the United States by aiding in the profitable production of shale formations which dominate most of North America. There is still a great need however to further the effectiveness and understanding of hydraulic

fracture treatment so that we can increase production and profitability while decreasing the risks commonly associated with public health and the environment.

The results of the 3D numerical model were compared to analytical solutions for the induced stresses. As we can see, the normalized induced stress ($\Delta\sigma_{yy}/p_{net}$) in the direction perpendicular to the fracture is in agreement with the analytical solution. There is a slight disparity between analytical and numerical results in ($\Delta\sigma_{xx}/p_{net}$) along the direction parallel to the fracture. This is due to the fact that analytical solutions are based on the plane-strain condition, which is not fully governed in 3D numerical model. For the same reason, the contour surfaces of slip-tendency demonstrate different behavior along the direction parallel to the fracture. The contour surfaces have almost the same profiles in the region where fractures exist. Within the regions where pressurized fractures exist, the plane strain condition can be assumed such that the contour surfaces have almost the same profiles.

Slip tendency, T_s, is calculated based on Eqs. (10) and (12) for 2D plane strain models. Eqs. (10) and (12) are also used for 3D numerical simulations. For this purpose the faults are assumed to be parallel to the intermediate principal stress (σ_{Hamx} or σ_v), and β the same as that of initial critically stressed faults. In other words, the fault plane orientations are remained the same as those for initial critically stressed state when calculating T_s during hydraulic fracturing stimulation. Faults with angles other than the initial optimal oriented angle β may also be activated during hydraulic fracturing stimulation, that is not considered here. More details on obtaining the shear and normal stresses on an arbitrarily oriented plane can be found in Zoback (2007).

Strictly speaking, the maximum slip tendency should be the maximum one among all possible fault orientations. Whether the fault plane will be parallel to the intermediate principal stress (σ_{Hamx} or σ_v) or not, needs more detailed field studies. Under initial critically stressed state, $\sigma_v > \sigma_{Hmax} > \sigma_{hmin}$ is assumed for normal faults, $\sigma_{Hmax} > \sigma_v > \sigma_{hmin}$ for strike-slip faults. Before applying hydraulic pressure, optimal orientation of faults can be assumed to be parallel to the intermediate principal stress (σ_{Hamx} or σ_v), as illustrated in Zoback (2007, p155, Fig. 5.9a).

The in-situ principal stresses will be altered during hydraulic fracturing stimulation, this can lead to change in the optimal oriented angle β through Eq. (7) that clearly shows β as a function of minimum and maximum principal stresses. This change in principal stresses can lead to possibility of having the critically stressed faults being not parallel to σ_{Hamx} or σ_v, especially in the region close to fracture tips where stress concentration occurs. At fracture tips, the stress distributions are complex as illustrated by 3D numerical simulation. Having closer look at the strike-slip faulting environment, one can clearly see if the induced stress contrast, such as ($\Delta\sigma_{yy}$ - $\Delta\sigma_{xx}$), is less than the initial in-situ stress contrast ($\sigma_{xx} - \sigma_{yy}$), there will be no stress reverse region around pressurized fracture (stress reverse indicates horizontal principal stresses rotate 90°). In this situation, the critically stressed faults will still be parallel to the initial intermediate principal stress. Comparing the analytical solution for 2D plane strain model with 3D numerical simulation and show that the induced stress on fracture surface away from fracture tips is equal to p_{net}. If p_{net} is relatively small compared to initial in-situ stresses, the extent of stress reverse regions will be fairly small or may not exist. Thus the faults could be still assumed to be parallel to the initial intermediate principal stress σ_v. However, when p_{net} is relatively large compared to initial in-situ stresses, the directions of principal stresses will be complex around pressurized fracture. Similar behavior is also valid in the case of Normal faults.

Higher net pressures will increase the stimulated volume, however, the induced stresses decrease drastically as the distance from pressurized fracture increases (Fig. 10) such that at r/H = 3 different net pressures yield almost the same slip-tendency. These observations imply that there should be an optimal net pressure that will yield maximum economic Stimulated Reservoir Volume (SRV). In shear fracture reactivation, shear stimulation, higher net pressure will generate larger shear displacement, but the enhanced fracture permeability does not increase linearly with shear displacement. In other words, the relationship between shear displacement and change of permeability is nonlinear. This has been experimented in granite and marble along artificial, rough fractures under a variety of stress conditions by Lee and Cho (2002). They have demonstrated that the permeability increases initially as a function of shear displacement and eventually arrested and approached a limiting value. This clearly shows that there is a critical net pressure that can generate the maximum stimulated region, however, more experimental and numerical studies are required to make solid statements on the subject.

Monitoring microseismic events are often used to estimate the extent of SRV. The model presented in this manuscript predicts the unstable regions extend from fracture tips in both lateral and vertical directions that can be corresponded to relatively planar distributed microseismic events. Relatively planar patterns of microseismic events are commonly observed in the field and reported in published literatures (Shaffner et al. (2011). However, due to multi-stage stimulation, interaction of adjacent wells, and geological complexity, more diffuse event patterns are also frequently observed (Vermylen and Zoback 2011; Warpinski et al. 2012). Even though the microseismic events have been used extensively in oil and gas industry to locate the discontinuities and faults in unconventional reservoirs, however, shale composition and discontinuities affects the generation of microseismic events (Zoback et al., 2012).

The distributions of slip tendency along the line perpendicular to fractures. The numerical results are in agreement with the analytical solutions in the case of a single pressurized fracture. Within the distance of 3H, the slip tendency is less than the original value of 0.6 for models with a single fracture as well as multiple fractures. The slip tendency for the model with a single pressurized fracture is always larger than that with multiple pressurized fractures. As the distance from fractures increases, the slip tendency tends to restore to 0.6.

Influence of stress contrasts on slip tendencies in normal and strike-slip faulting environments is an interesting topic. According to our analyses, larger stimulated volume will be created in a lower stress contrasts in normal faulting regime compared to that of strike-slip faulting regime. The change of T_s during hydraulic stimulation for normal and strike-slip faulting environments, where p_{net}/σ_{hmin} = 0.2 and numbers in legend (0.2 and 0.6) indicate the initial slip tendency before performing hydraulic stimulation. As illustrated in the figure, the increased slip tendency for normal faulting regime almost independents of initial stress contrast where r/H > 0.5. And the changes of slip tendency in normal faulting regime are larger than those in the strike-slip faulting regime for initial slip tendency equal to 0.2 and 0.6. Within strike-slip faulting environment, faults with higher initial slip tendency, thus larger initial in-situ stress contrast, exhibits larger change of T_s.

It should be noted that this study does not consider the poroelastic effects and assumes an elastic medium with homogeneous and isotropic properties. It is commonly considered that the increase of pore pressure causes an increase of total compressive horizontal stress (Engelder and Fischer 1994). However, the effective normal stress acting on a fault plane would still be reduced due to the increase

of pore pressure. The combined effect tends to increase the slip-tendency and reduce the fault stability. More analyses are needed to improve this mode.

Our study shows that proppant settling can cause heterogeneous distribution of proppant and reduce the cumulative production by 18.6% or more depending on the reservoir matrix permeability. It also predicts an optimum proppant size to achieve maximum hydraulic fracturing efficiency in tight formations such as shale with known matrix permeability as a function of relative proppant density. The Simulation results also predict that the combination of smaller proppant followed by larger proppant size can improve the stimulation performance and there exist an optimum value for larger proppant size volume injected to achieve the maximum stimulation efficiency. It also predicted that the magnitude of the difference between two proppant sizes can also significantly impact the stimulation efficiency depending on the relative proppant density.

Sensitivity analysis of proppant size while other parameters kept constant shows that in low permeability reservoir, smaller proppant size with lower relative density is generally more suited and there is an optimum proppant size exist that can reduce the settling velocity and lead to a larger flowing area; in a high permeability reservoir, however, larger proppant can provide better performance because high permeability flow channel is more granted.

5. Acknowledgements

Funding for this project is provided by RPSEA through the "Ultra-Deepwater and Unconventional Natural Gas and Other Petroleum Resources" program authorized by the U.S. Energy Policy Act of 2005. RPSEA (www.rpsea.org) is a nonprofit corporation whose mission is to provide a stewardship role in ensuring the focused research, development and deployment of safe and environmentally responsible technology that can effectively deliver hydrocarbons from domestic resources to the citizens of the United States. RPSEA, operating as a consortium of premier U.S. energy research universities, industry, and independent research organizations, manages the program under a contract with the U.S. Department of Energy's National Energy Technology Laboratory.

Range Resources

Contributors

6. Publications and Presentations

1 – J.Q. Bao, E. Fathi, S. Ameri. A Method for the Numerical Simulation of Hydraulic Fracturing with a Condensation Technique. Engineering Fracture Mechanics, 2014. Volume 131. p. 269-281.

2 – J.Q. Bao, E. Fathi, S. Ameri. Uniform Investigation of Hydraulic Fracturing Propagation Regimes in the Plane Strain Model. International Journal for Numerical and Analytical Methods in Geomechanics, 2015. Volume 39. p. 507-523.

3 – B. Kong, E. Fathi, S. Ameri. Fracturing Performance Optimization in Marcellus Shale Reservoirs. International Journal of Coal Geology, 2015. Volume 147-148. p. 35-45.

4 – Q. Gao, Y. Cheng, E. Fathi, S. Ameri. Analysis of Stress-Field Variations Expected on Subsurface Faults and Discontinuities in the Vicinity of Hydraulic Fracturing. Society of Petroleum Engineers, 2013. Unconventional Resources Technology Conference. Denver, Colorado. USA.

5 – R. Zhong, J. Bao, E. Fathi. Fully Coupled Finite Element Model to Study Fault Reactivation during Multiple Hydraulic Fracturing in Heterogeneous Tight Formations. Society of Petroleum Engineers, 2014. SPE Eastern Regional Meeting. Charleston, West Virginia. USA.

6 – A. Jenkins, E. Fathi, L. Reddy. Dynamic Assessment of Stress Field Behavior Induced by Fracture Tip Propagation in Quasi-Brittle/Ductile Shale Reservoirs: A New Approach Based on Modified Theory of Critical Distances. 13th U.S. National Congress on Computational Mechanics, 2015. San Diego, California. USA.

7 – L. Reddy, A. Jenkins, E. Fathi. Dynamic Assessment of Induced Stresses and In-Situ Reorientation during Multi-Stage Hydraulic Fracturing in Unconventional Reservoirs. Society of Petroleum Engineers, 2015. SPE Eastern Regional Meeting. Morgantown, West Virginia. USA.

8 – J.Q. Bao, Y. Cheng. Numerical Simulation of Hydraulic Fracturing with Finite Element Method. Computer Methods in Applied Mechanics and Engineering, 2014. (Under Review).

7. References

Cheng, Y. (2012, December). Mechanical Interaction of Multiple Fractures-Exploring Impacts of the Selection of the Spacing/Number of Perforation Clusters on Horizontal Shale Gas Wells. *SPE Journal*, 992-1001.

Dhondt, G. (2004). *The Finite Element Method for Three-Dimensional Thermomechanical Applications.* John Wiley & Sons.

Ellsworth, W. L. (2013, July 12). Injection-Induced Earthquakes. *Science, 341*(6142). doi:10.1126/science.1225942

Nathan M. Newmark, E. R. (1971). *Fundamentals of Earthquake Engineering.* Englewood Cliffs, N.J.: Prentice Hall, Inc.

Qian Gao, Y. C. (2013). Characterization of Stress-Field Variation on Subsurface Faults in Surrounding Areas of Hydraulic Fracuring. *Unconventional Resources Technology Conference.* URTeC.

8. Appendix

8.1. Marcellus Assessment

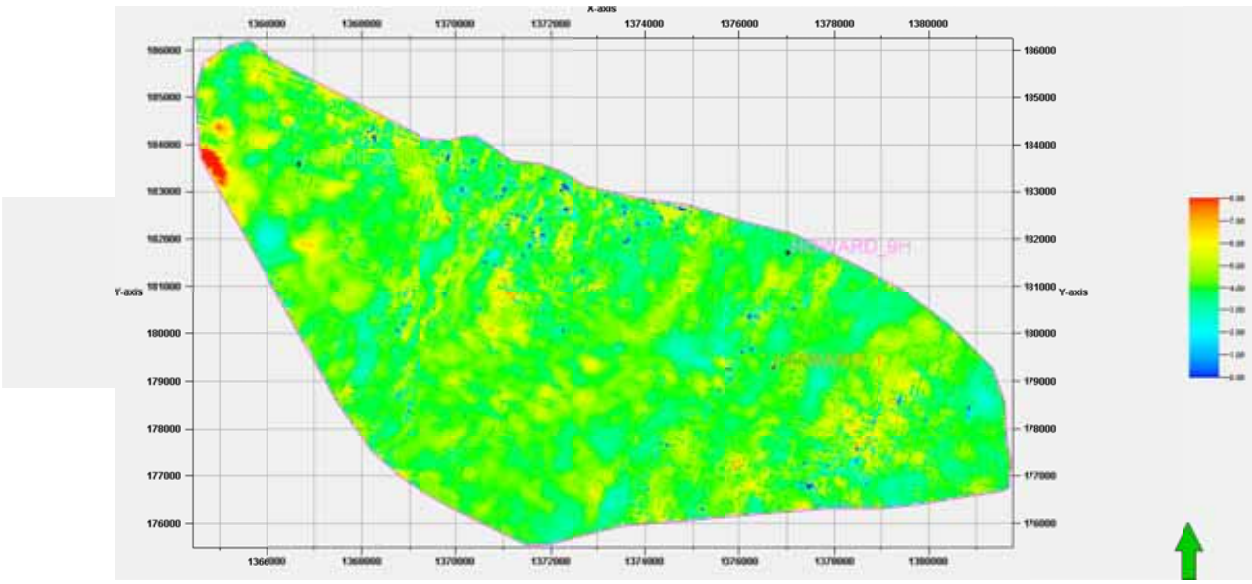

Figure 95 - Young's Modulus of Marcellus Shale

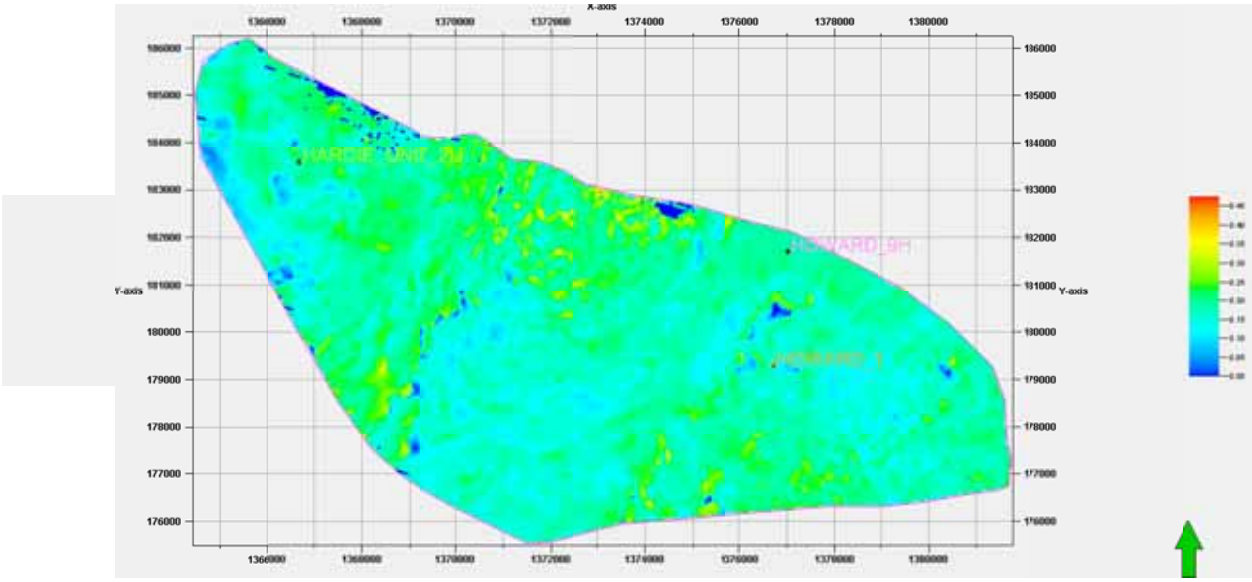

Figure 96 - Poisson's Ratio of Marcellus Shale

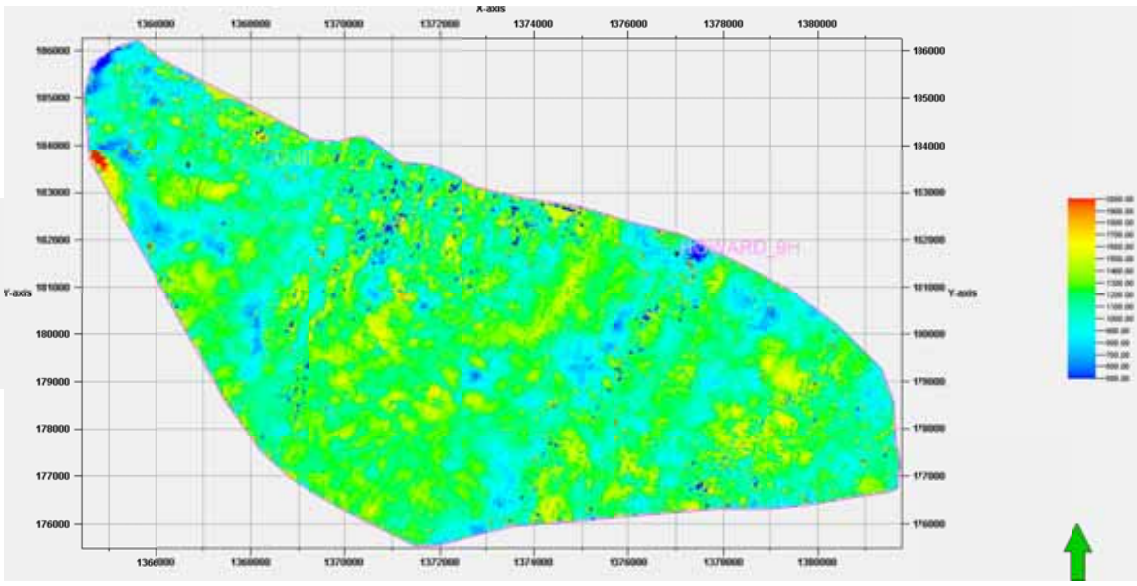

Figure 97 - Tensile Stress of Marcellus Shale

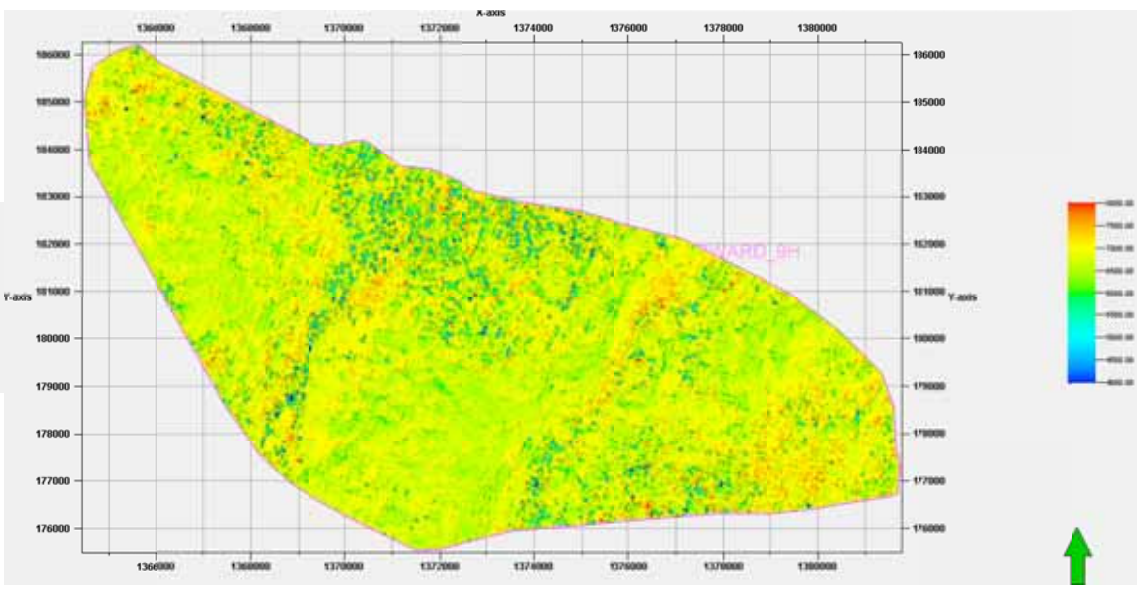

Figure 98 - Minimum Horizontal Stress of Marcellus Shale

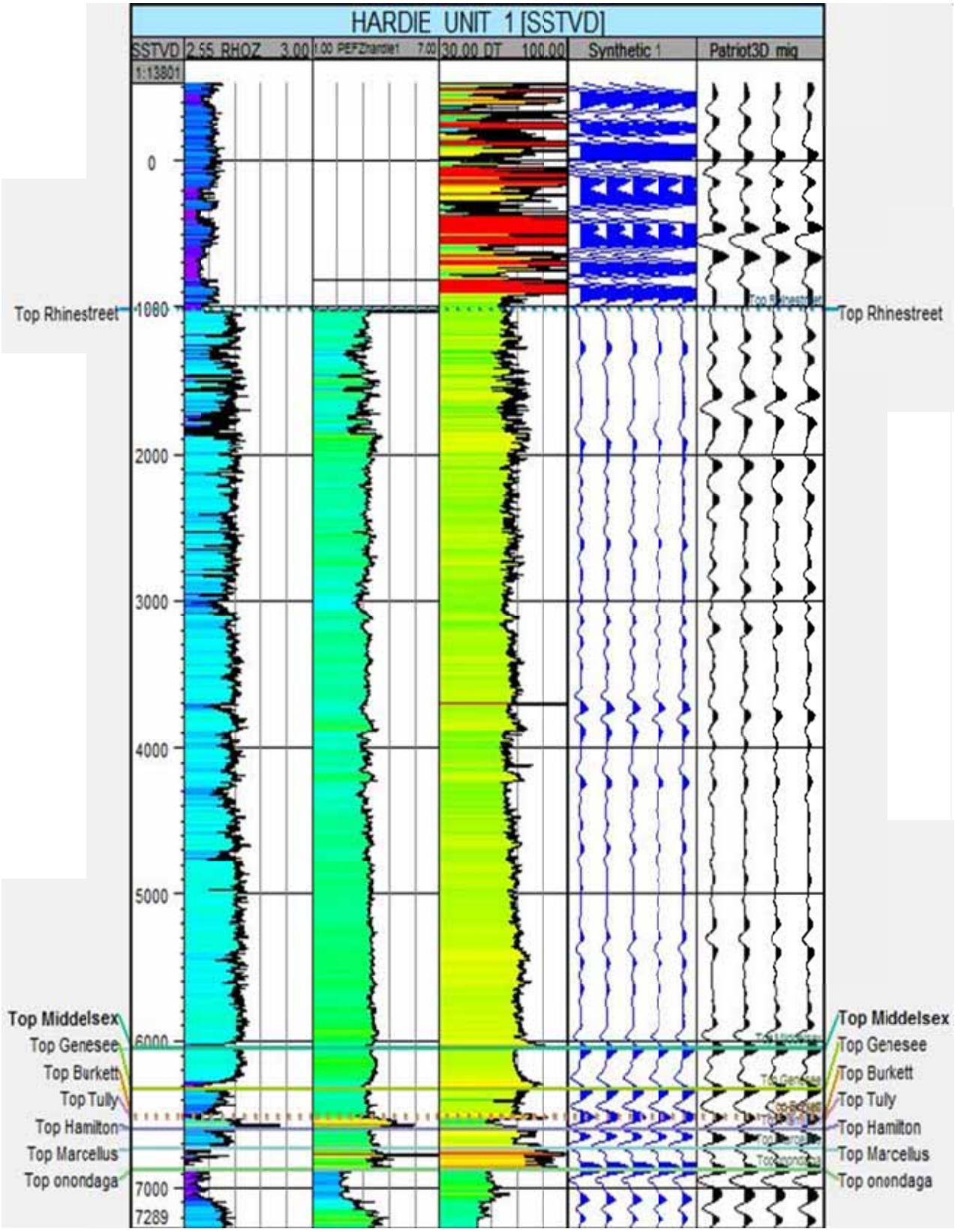

Figure 99 - Synthetic Seismogram, Real Seismic Trace and Well Tops (Hardie Unit 1)

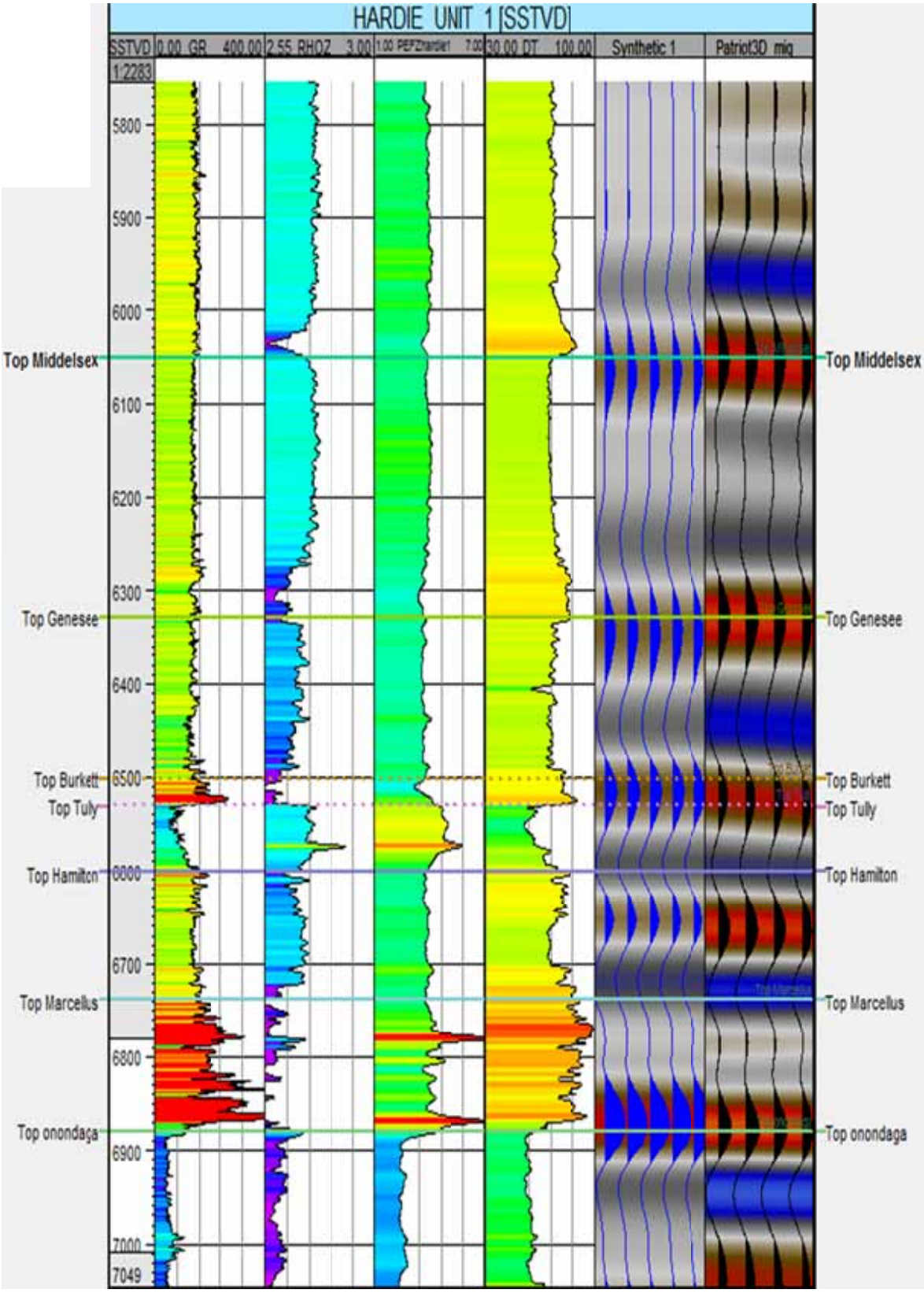

Figure 100 - Readjustments of Synthetic Seismogram

8.2. Geomechanical Model

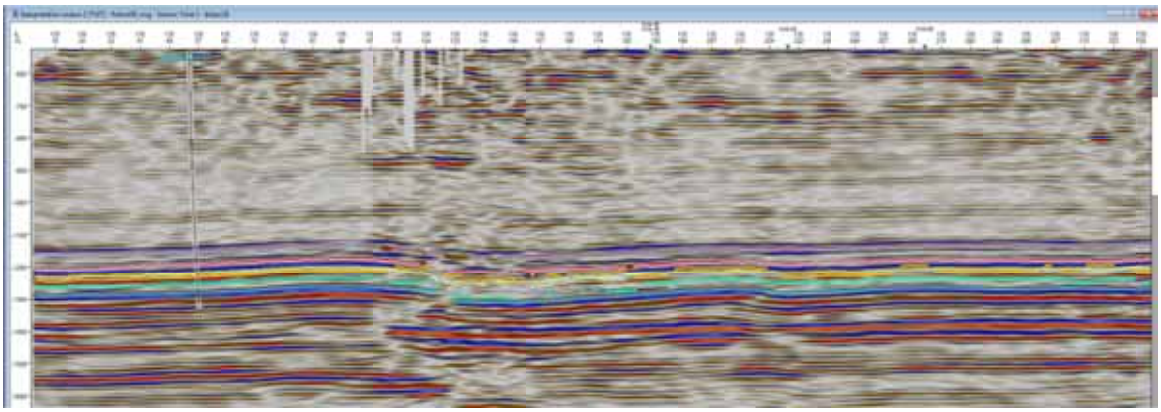

Figure 101 Illustration of Horizons Picked on Seismic Profile

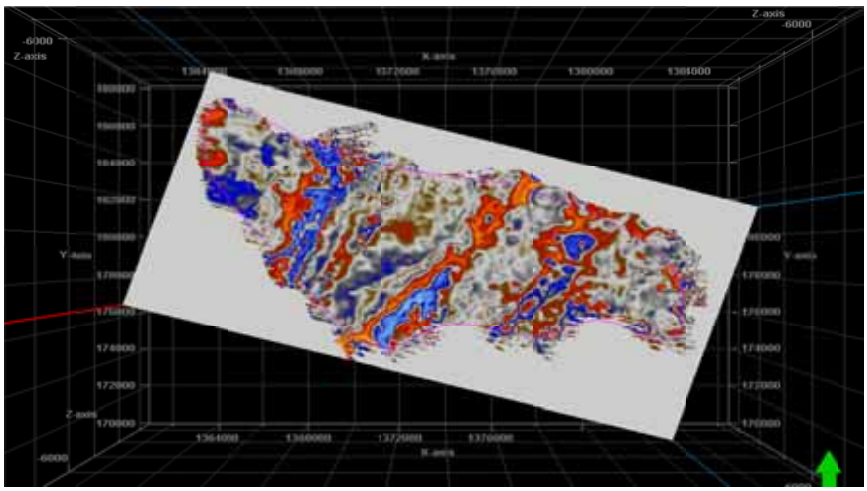

(a) Seismic survey area

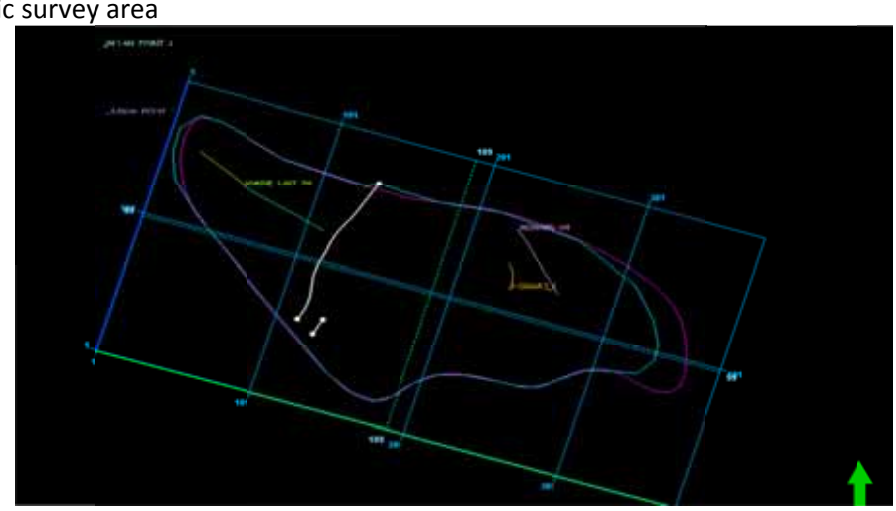

(b) Boundaries of the study area (green line) and seismic survey (pink line)

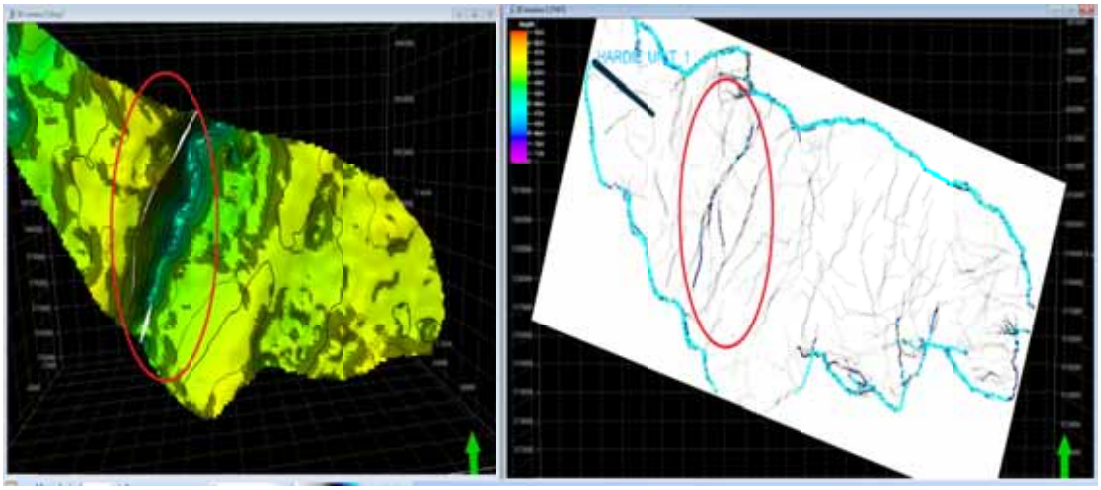

Figure 102 - Illustration of the main faults identified through ant tracking

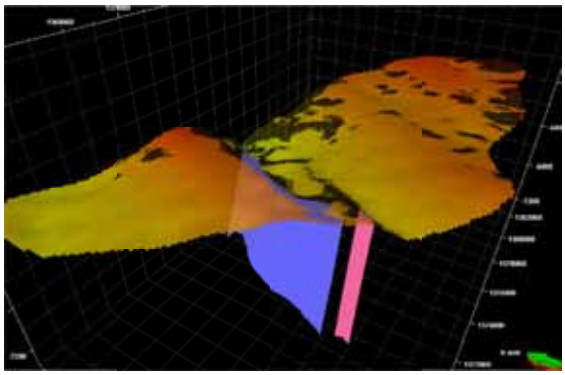

(a) Surface of the top of Middlesex shale

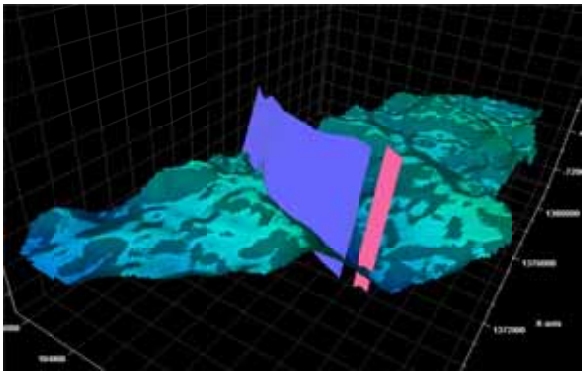

(b) Surface of the top of Marcellus shale

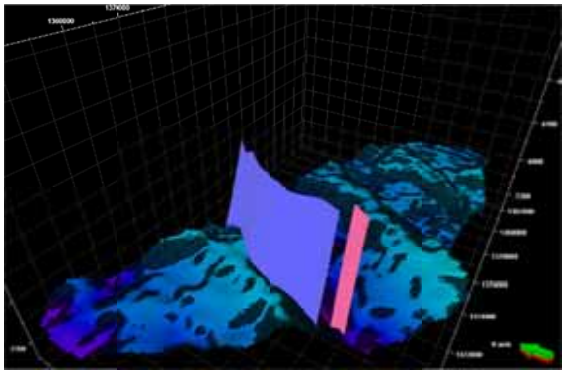

(c) Surface of the top of Onondaga limestone

Figure 103 - Spatial relationship of faults and surface of different formations

8.3. Finite Element Solution of Static Stress Reservoir

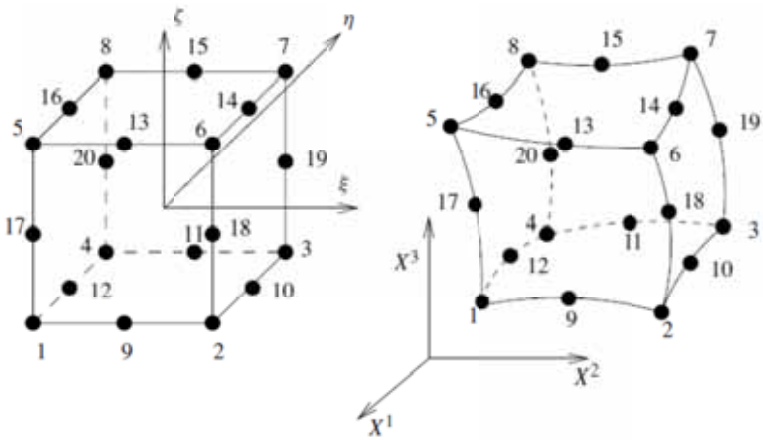

Figure 104 Schematic of the 20 Node Brick Element

At each vertex of the brick element a node exists such that the shape functions are as follows:

$$\varphi_i(\xi_j, \eta_j, \zeta_j) = \delta_{ij}$$

This satisfies the discrete position and shape function relationship using the isoperimetric (i.e. the same) formulation defined below:

$$U(X) = \sum_{i=1}^{N} \varphi_i(\xi, \eta, \zeta) U(X_i)$$

$$X = \sum_{i=1}^{N} \varphi_i(\xi, \eta, \zeta) X_i$$

The shape functions of the 20 node element are as follows for each of the individual nodal points throughout the element. In the case of the 20 node hexahedron these nodes are located at each of the corner points and mid points of a three dimensional cube as shown in the figure above. These nodal shape functions define the exact solutions whereas the intermediate areas of the solution are approximated from the known solution at these points.

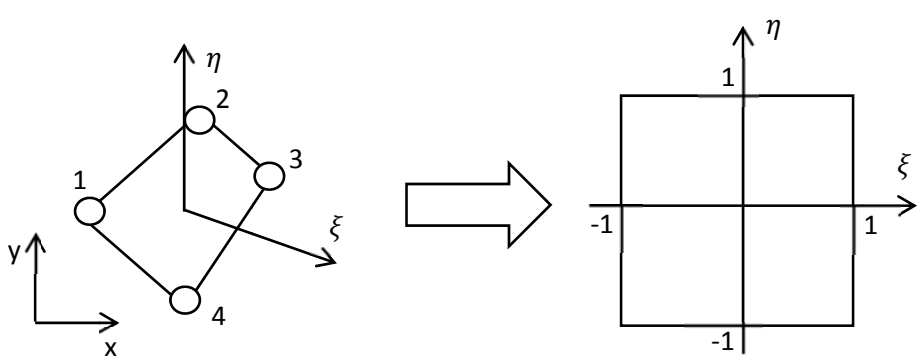

Figure 105 Mapping a Surface Element in Local Coordinates onto Global Coordinates

The coordinates of the nodes with respect to a central local and global system are defined in Error! Reference source not found..

	X	Y	Z
N1	-1	-1	-1
N2	1	-1	-1
N3	1	1	-1
N4	-1	1	-1
N5	-1	-1	1
N6	1	-1	1
N7	1	1	1
N8	-1	1	1
N9	0	-1	-1
N10	1	0	-1
N11	0	1	-1
N12	-1	0	-1
N13	-1	-1	0
N14	1	-1	0
N15	1	1	0
N16	-1	1	0
N17	0	-1	1
N18	1	0	1
N19	0	1	1
N20	-1	0	1

Table 13 Nodal Coordinate Locations of a 20-Node Hexahedron Element

$$[N] = [N_1\ N_2\ N_3\ N_4\ N_5\ N_6\ N_7\ N_8\ N_9\ N_{10}\ N_{11}\ N_{12}\ N_{13}\ N_{14}\ N_{15}\ N_{16}\ N_{17}\ N_{18}\ N_{19}\ N_{20}]$$

The first eight equations here represent the shape functions at the corners of the hexahedral, while the remaining twelve equations are representative of the associated midpoints on the cube. The three dimensional notation of [x,y,z] is represented by $[\xi, \eta, \zeta]$ respectively.

$$\varphi_1 = -(1-\xi)(1-\eta)(1-\zeta)(2+\xi+\eta+\zeta)/8$$

$$\varphi_2 = -(1+\xi)(1-\eta)(1-\zeta)(2-\xi+\eta+\zeta)/8$$

$$\varphi_3 = -(1+\xi)(1+\eta)(1-\zeta)(2-\xi-\eta+\zeta)/8$$

$$\varphi_4 = -(1-\xi)(1+\eta)(1-\zeta)(2+\xi-\eta+\zeta)/8$$

$$\varphi_5 = -(1-\xi)(1-\eta)(1+\zeta)(2+\xi+\eta-\zeta)/8$$

$$\varphi_6 = -(1+\xi)(1-\eta)(1+\zeta)(2-\xi+\eta-\zeta)/8$$

$$\varphi_7 = -(1+\xi)(1+\eta)(1+\zeta)(2-\xi-\eta-\zeta)/8$$

$$\varphi_8 = -(1-\xi)(1+\eta)(1+\zeta)(2+\xi-\eta-\zeta)/8$$

$$\varphi_9 = (1-\xi)(1+\xi)(1-\eta)(1-\zeta)/4$$

$$\varphi_{10} = (1+\xi)(1-\eta)(1+\eta)(1-\zeta)/4$$

$$\varphi_{11} = (1-\xi)(1+\eta)(1+\zeta)(1-\zeta)/4$$
$$\varphi_{12} = (1-\xi)(1-\eta)(1+\zeta)(1-\zeta)/4$$
$$\varphi_{13} = (1-\xi)(1+\eta)(1-\zeta)(1+\zeta)/4$$
$$\varphi_{14} = (1+\xi)(1-\eta)(1+\zeta)(1+\zeta)/4$$
$$\varphi_{15} = (1-\xi)(1+\eta)(1+\zeta)(1+\zeta)/4$$
$$\varphi_{16} = (1-\xi)(1-\eta)(1+\zeta)(1+\zeta)/4$$
$$\varphi_{17} = (1-\xi)(1-\eta)(1-\zeta)(1+\zeta)/4$$
$$\varphi_{18} = (1+\xi)(1-\eta)(1-\zeta)(1+\zeta)/4$$
$$\varphi_{19} = (1+\xi)(1+\eta)(1-\zeta)(1+\zeta)/4$$
$$\varphi_{20} = (1-\xi)(1+\eta)(1-\zeta)(1+\zeta)/4$$

Defining an element vector containing all displacements belonging to the element, such as:

$$\{U\}_e = \begin{bmatrix} U_{11} \\ U_{12} \\ U_{13} \\ U_{21} \\ \dots \\ U_{N1} \\ U_{N2} \\ U_{N3} \end{bmatrix}_e$$

So that in three dimensions the element stiffness matrices' properties are derived and represented as follows:

$$[k_m] = \int\int\int [B]^T [D][B]\, dx\, dy\, dz$$

$$\begin{Bmatrix} \epsilon_x \\ \epsilon_y \\ \epsilon_z \\ \gamma_{xy} \\ \gamma_{yz} \\ \gamma_{zx} \end{Bmatrix} = \begin{bmatrix} \frac{\partial}{\partial x} & 0 & 0 \\ 0 & \frac{\partial}{\partial y} & 0 \\ 0 & 0 & \frac{\partial}{\partial z} \\ \frac{\partial}{\partial y} & \frac{\partial}{\partial x} & 0 \\ 0 & \frac{\partial}{\partial z} & \frac{\partial}{\partial y} \\ \frac{\partial}{\partial z} & 0 & \frac{\partial}{\partial x} \end{bmatrix} \begin{Bmatrix} u \\ v \\ w \end{Bmatrix}$$

The following 3 x 3 x 3 integration scheme Error! Reference source not found. represents the full-integration of the 20-node hexahedral element:

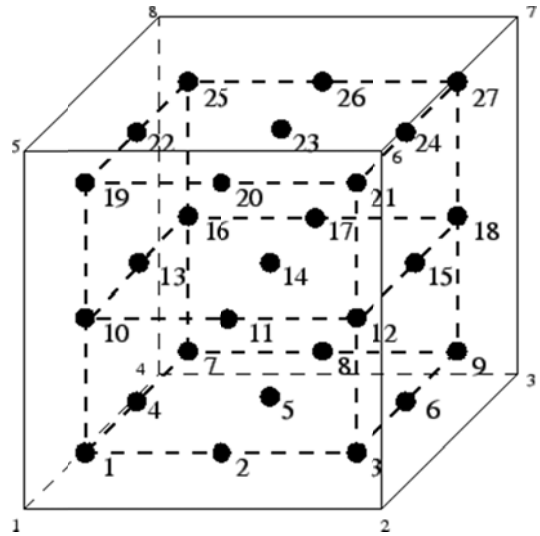

Figure 106 The 3 x 3 x 3 Integration point scheme on hexahedral elements

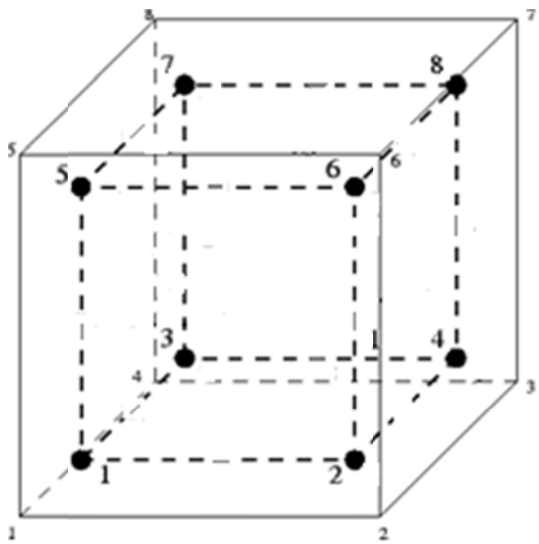

Figure 107 The 2 x 2 x 2 Integration Point Scheme on Hexahedral Elements

Scheme	Location	Number	Weight
1 x 1 x 1	$(0,0,0)$	1	8
2 x 2 x 2	$\left(\pm\frac{1}{\sqrt{3}},\pm\frac{1}{\sqrt{3}},\pm\frac{1}{\sqrt{3}}\right)$		
3 x 3 x 3	$\left(\pm\frac{3}{\sqrt{5}},\pm\frac{3}{\sqrt{5}},\pm\frac{3}{\sqrt{5}}\right)$	8	$\left(\frac{5}{9}\right)^3$
	$\left(0,\pm\frac{3}{\sqrt{5}},\pm\frac{3}{\sqrt{5}}\right)$	12	$\left(\frac{8}{9}\right)\left(\frac{5}{9}\right)^2$
	$\left(0,0,\pm\frac{3}{\sqrt{5}}\right)$		

$(0,0,0)$	6	$\left(\frac{8}{9}\right)^2\left(\frac{5}{9}\right)$
		$\left(\frac{8}{9}\right)^3$
	1	

Table 14 Location of Integration Points in Hexahedral Elements

$$\sigma_{xxj} = \sum_{i=1}^{8} \varphi_i(\xi_j, \eta_j, \zeta_j)\sigma_{xxi}, \;\; j = 1, \dots, 8$$

Where i are the nodes and j are the integration points for a reduced integration 20-node hexahedral.

This can be presented in matrix form as follows:

$$\{\sigma_{xx}\}_{integration\ points} = [A]\{\sigma_{xx}\}_{nodes}$$

From this the nodal values can be determined by inverting the previous equation.

$$\{\sigma_{xx}\}_{nodes} = [A]^{-1}\{\sigma_{xx}\}_{integration\ points}$$

The size of [A] in this case (20-node reduced integration hexahedron) is an 8 x 8 matrix which can be evaluated explicitly as both the shape functions and integration point location are known. The explicit definition of the inverse matrix $[A]^{-1}$ is as follows:

$$[A]^{-1} = \begin{bmatrix} +2.549 & -0.683 & -0.683 & +0.183 & -0.683 & +0.183 & +0.183 & -0.049 \\ -0.683 & +2.549 & +0.183 & -0.683 & +0.183 & -0.683 & -0.049 & +0.183 \\ +0.183 & -0.683 & -0.683 & +2.549 & -0.049 & +0.183 & +0.183 & -0.683 \\ -0.683 & +0.183 & +2.549 & -0.683 & +0.183 & -0.049 & -0.683 & +0.183 \\ -0.683 & +0.183 & +0.183 & -0.049 & +2.549 & -0.683 & -0.683 & +0.183 \\ 0.183 & -0.683 & -0.049 & +0.183 & -0.683 & +2.549 & +0.183 & -0.683 \\ -0.049 & +0.183 & +0.183 & -0.6683 & +0.183 & -0.683 & -0.683 & +2.549 \\ +0.183 & -0.049 & -0.683 & +0.183 & -0.683 & +0.183 & +2.549 & -0.683 \end{bmatrix}$$

In order to evaluate the fully integrated case of a 20-node hexahedral then the system becomes over determined as there becomes a system of 27 equations and only 20 unknowns, seen from the element shape function below:

$$\sigma_{xxj} = \sum_{i=1}^{20} \varphi_i(\xi_j, \eta_j, \zeta_j)\sigma_{xxi}, \;\; j = 1, \dots, 27$$

In order to solve these types of systems a solution scheme must be chosen. A standard procedure in the solution of an over determined system such as this is the least squares method where the fully integrated equation shown above becomes:

$$b_j = \sum_{i=1}^{20} a_{ji} x_i, \;\; j = 1, \dots, 27$$

$$I := \sum_{j=1}^{20} \left(\sum_{i=1}^{27} a_{ji} x_i - b_i, \right)^2$$

The least squares approximation allows the solution to be found by the use of typical differentiation techniques:

$$\frac{\partial I}{\partial x_k} = 2 \sum_{j=1}^{27} \left[\left(\sum_{i=1}^{20} a_{ji} x_i - b_i \right) a_{jk} \right] = 0, \;\; k = 1, \dots, 20$$

$$\sum_{i=1}^{20} \left[\left(\sum_{j=1}^{27} a_{ji} a_{jk} \right) x_i \right] = \sum_{j=1}^{27} a_{jk} b_j \,, \;\; k = 1, \dots, 20$$

Or can also be defined by the following condensed form instead of that shown above:

$$\sum_{i=1}^{20} c_{ki} x_i = d_k, \;\; k = 1, \dots, 20$$

Where the expansion of c_{ki} and d_k is:

$$c_{ki} = \sum_{i=1}^{27} a_{jk} a_{ji}, \;\; k = 1, \dots, 20$$

$$d_k = \sum_{i=1}^{27} a_{jk} b_j, \;\; k = 1, \dots, 20$$

This produces a solvable system of 20 equations and 20 unknowns. If $\{b_1\}$ is a unit vector with a unit value located in the first row then the solution $\{x_1\}$ contains the nodal values for a unit value in the first integration point and zero in all of the other integration points. This process is repeated for all other integration points throughout the element which yields a 20 x 27 matrix $[B]$ that appears in the equations below:

$$\{\sigma_{xx}\}_{nodes} = [B]\{\sigma_{xx}\}_{integration\ points}$$

Which takes the following form for all of the associated integration points as noted above.

$$[B] = [\{x_1\}\{x_2\} \dots \{x_{27}\}]$$

Equation of Stress Equilibrium

To represent the distribution of stress and strain, the equation of stress equilibrium – a governing partial differential equation in the displacement form is needed (Jaeger, Cook and Zimmerman, 2007). The hydro-mechanical behavior can be considered based on Biot's theory of poroelasticity.

$$G\nabla^2\boldsymbol{\delta} + \frac{G}{1-2\nu}\nabla(\nabla\cdot\boldsymbol{\delta}) + \alpha\nabla p + \rho\mathbf{F} = 0$$

*where G is the shear modulus, $\boldsymbol{\delta}$ is the displacement vector with three components (u, v, w), ν is Poisson's ratio, α is Biot's poroelastic constant (generally assumed as 1), p is the pore pressure, ρ is the bulk density and **F** is the body force vector per unit mass. ∇^2 is the Laplacian operator and ∇ is the gradient/divergence operator. With the strain-displacement relations*

$$\boldsymbol{\varepsilon} = \frac{1}{2}[\nabla\boldsymbol{\delta} + (\nabla\boldsymbol{\delta})^T]$$

and the stress-strain relations

$$\boldsymbol{\sigma} = \lambda trace(\boldsymbol{\varepsilon})\mathbf{I} + 2G\boldsymbol{\varepsilon}$$

strain and stress can be found once the displacement is solved. In Eqs 2 and 3, $\boldsymbol{\varepsilon}$ represents the strain matrix, $\nabla\boldsymbol{\delta}$ is the displacement gradient, *T* stands for the transpose of a matrix, $\boldsymbol{\sigma}$ is the stress matrix, λ is the Lam*é* parameter, **I** is the identity matrix and *G* is the shear modus.

Continuity Equation

It is a mathematical representation of the principle of mass conservation. Continuity equation of a fluid in a porous rock is given by

$$\nabla\cdot(\rho\mathbf{u}) = -\frac{\partial(\nabla\cdot\boldsymbol{\delta})}{\partial t} + \phi c_f\frac{\partial p}{\partial t}$$

The assumption related to Eq. 4 is that the density of the rock grains is constant (Chin, Raghavan and Thomas, 2000, Thomas, *et al.*, 2003). In the equation, **u** is the fluid velocity vector, c_f is the compressibility of the fluid in pores of rock and ϕ is the porosity.

Darcy's Law

The flow of a fluid through a porous medium is modeled by Darcy's law, which is an expression of conservation of momentum. It relates fluid velocity proportionally to the gradient of the potential.

$$\mathbf{u} = -\frac{k}{\mu}\nabla\Phi$$

where k is the permeability of a porous medium and μ is the fluid viscosity.

In Eq. 5, $\nabla\Phi$ is the gradient of flow potential defined as

$$\nabla\Phi = \nabla p + \rho g\nabla Z$$

where g is the gravitational acceleration and Z is elevation.

Equation of State

An equation of state presents a relation between properties of matters and a given set of physical conditions. In a porous medium, both pores and fluid are compressible. With the assumption of

isothermal conditions, the compressibility of the pores is represented by the change in porosity with pressure,

$$c_p = \frac{1}{\phi}\frac{\partial \phi}{\partial p}$$

while the compressibility of the liquid is represented by the change in density with pressure

$$c_f = \frac{1}{\rho_l}\frac{\partial \rho_l}{\partial p}$$

where ρ_l is the liquid density. For gas, the real-gas law is used to model the behavior of the gas

$$\rho = \frac{pM}{zRT}$$

where M represents the molecular weight of the gas, z stands for the compressibility factor, R is referred to as universal gas constant and T is the reservoir temperature. The compressibility of the gas is given by

$$c_g = \frac{z}{p}\frac{\partial}{\partial p}\left(\frac{p}{z}\right)$$

Eq. 1 provides three governing equations, one for each of displacement components. The diffusion equation for pore fluid obtained by combination of continuity equation, Darcy's law and equation of state is accounted for another governing equation. The three displacement components and the pore pressure are taken as the four basic field unknowns of poroelasticity. This is a well-posed problem to solve.

The reservoir geometry is assumed a parallelepiped. The outer boundary conditions are given at a constant displacement for each of individual boundaries except the top. At the reservoir top, a constant overburden stress is used. The inner boundary condition is a constant net pressure applied along the hydraulic fractures.

A numerical model was established by discretization of partial differential equations over each element using the finite element method. With the Galerkin's method, the equation of stress equilibrium and the diffusion equation are discretized into a linear system of equation with unknowns of nodal displacement field and nodal pore pressure field. The displacement and pore pressure at an arbitrary point over an element are

$$\boldsymbol{\delta} = \sum_{i=1}^{n} N_i \boldsymbol{\delta}_i$$

$$\mathrm{p} = \sum_{i=1}^{n} N_i p_i$$

where N is the shape functions, δ_i and p_i represent values at nodes, respectively. The discretized equations have the following forms,

$$[\mathbf{k}_s]\boldsymbol{\delta} + [\boldsymbol{c}_s]p = \mathbf{r}_s$$

$$[\mathbf{k}_p]\dot{\boldsymbol{\delta}} + [\mathbf{b}]\dot{p} + [\boldsymbol{c}_p]p = \mathbf{r}_p$$

where $\boldsymbol{k_s}$ is a matrix related to rock elastic properties and shape functions; $\boldsymbol{c_s}$ and $\boldsymbol{k_p}$ are matrix dependent on shape functions; $\boldsymbol{c_p}$ and $\boldsymbol{b}$ are matrix related to properties of rock and reservoir fluid; $\boldsymbol{r_s}$ and $\boldsymbol{r_p}$ represent residual force vectors; $\dot{\boldsymbol{\delta}}$ is the partial derivative of the displacement with respect to time; and $\dot{p}$ is the partial derivative of the pore pressure with respect to time.

8.4. Finite Element Solution with Dynamic Fracture Propagation

Fracture propagation momentum from the injection of an incompressible Newtonian fluid with constant rate is considered in this paper. Based on LEFM, a plane-strain fracture propagation in an isotropic and homogeneous solid medium is related to its material properties, i.e., elastic modulus *E*, the Poisson's ratio ν, and fracture toughness K_{IC}. Let Q_0 denote the injection rate as shown in Fig. 1, μ denote the dynamic viscosity of the fluid, and C_l denote the leak-off coefficient. New material parameters are defined for convenience as

$$E' = \frac{E}{1-\nu^2}, \quad K' = 4\left(\frac{2}{\pi}\right)^{1/2} K_{IC}, \quad \mu' = 12\mu, \quad C_l' = 2C_l$$

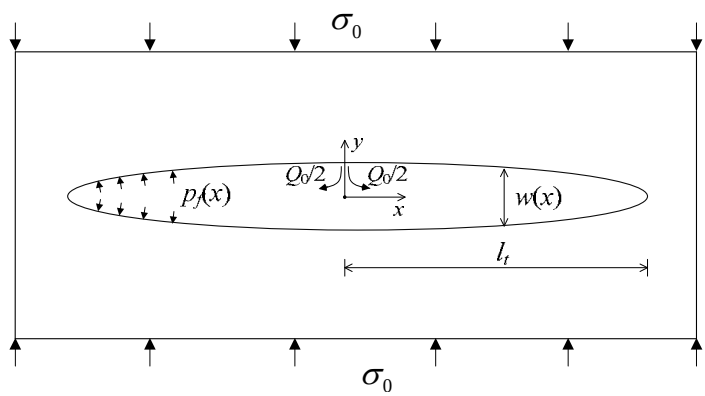

Figure 108 - Sketch of a plane-strain fluid-driven fracture

The fracture profile is symmetric if the confining stress σ_0 as shown in Fig. 1 is uniform, and the relationship between fracture width *w* and net fluid pressure p at any moment *t* in the half space ($x \geq 0$) can be expressed as [25]

$$w(x,t)=\frac{\pi}{4E'}\int_{l_t}\ln\left|\frac{\sqrt{l_t^2-x^2}+\sqrt{l_t^2-x_1^2}}{\sqrt{l_t^2-x^2}-\sqrt{l_t^2-x_1^2}}\right|p(x_1,t)dx_1$$

where l_t is the half fracture length at time t as shown in Fig. 1, and the net pressure p satisfies

$$p(x,t)=p_f(x,t)-\sigma_0(x)$$

where p_f is fluid pressure, and σ_0 is positive when it is compressive . It is seen in Eqs. (2) and (3) that net pressure rather than fluid pressure contributes to fracture width. Due to symmetry and Eqs. (2) and (3), the model in Fig. 1 can be represented by its equivalent quarter model as shown in Fig. 2, where the fracture surface is applied with net pressure.

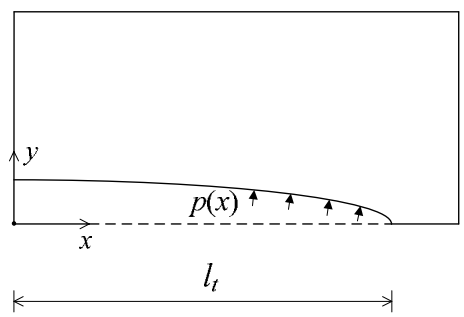

Figure 109 - Equivalent quarter model

Fracture propagation is dominated by the normal opening mode, and the propagation criterion is

$$K_I=K_{IC}$$

where K_I is the stress intensity factor (SIF) for the tensile opening mode of the fracture, and K_{IC} is the fracture toughness of the tensile opening mode. When K_I reaches K_{IC} at the fracture tip, the near tip fracture width can be approximated by [33]

$$w(x)=\frac{K'}{E'}(l-x)^{1/2}+O[(l-x)^{3/2}],\ l-x<<l$$

The governing equation for incompressible fluid flow in the fracture arises from the mass conservation of the fluid, and is written as

$$\frac{\partial w}{\partial t}+g=-\nabla\cdot\boldsymbol{q}$$

where ($\nabla\cdot$) is the divergence operator, $\boldsymbol{q}$ is the fluid flux, and g is the leak-off. It is seen in Eq. (6) the fluid flowing through the fracture is divided into two parts: the first part is to be stored in the fracture and increase the fracture width, and the second part leaks into the solid medium.

According to lubrication theory, the relationship between the fluid flux $\boldsymbol{q}$ and fracture width w is given by Poiseuille law's [34], i.e.,

$$\boldsymbol{q} = -\frac{w^3}{\mu'}\nabla p_f$$

where (∇) is the gradient operator. The leak-off is characterized by Carter's model [11] as

$$g(x,t) = C_l' / \sqrt{t - t_0(x)}\ ,\ t > t_0(x)$$

where t_0 is the fracture tip arrival time. If there is no fluid lag and the confining stress is uniform, Eq. (7) can be rewritten as

$$\boldsymbol{q} = -\frac{w^3}{\mu'}\nabla p$$

It is worth pointing out that the divergence and gradient operators in Eqs. (6), (7) and (9) are defined in fracture propagation direction, i.e., the *x* direction in Fig. 2.

The boundary conditions for fluid flow are

$$\boldsymbol{q}(x=0^+,t) = Q_0/2,\ \boldsymbol{q}(x=l_t,\ t) = 0$$

The first boundary condition in Eq. (10) is from the symmetry of the bi-wing fracture as shown in Eq. (10). The second boundary condition of zero flux at the fracture tip in Eq. (10) originates from zero fracture width at the tip [6] as seen in Eq. (7).

Via divergence theorem[35], Eq. (6) combined with the boundary condition in Eq. (10) and the leak-off model in Eq. (8) leads to the global fluid continuity equation [16]

$$\int_0^{l_t} w(x,t)dx + \int_0^t \int_0^{l_{t'}} g(x,t')dxdt' = \frac{1}{2}Q_0 t$$

According to Eq. (11), the injection efficiency η, which is the volume ratio of the fluid stored in the fracture to the injected fluid, is defined as

$$\eta(t) = \int_0^{l_t} w(x,t)dx \Big/ \left[\frac{1}{2}\left(Q_0 t\right)\right]$$

3. Hydraulic fracturing regimes and asymptotic solutions

Hydraulic fracturing regimes in the plane strain model are constructed by a rectangular phase diagram $M\tilde{M}K\tilde{K}$ as shown in Fig. 3 in (K_m , C_m) space[15], where K_m and C_m are defined as:

$$K_m = \frac{K'}{E'}\left(\frac{E'}{\mu' Q_0}\right)^{1/4}, \; C_m = C'\left(\frac{E't}{\mu' Q_0^3}\right)^{1/6}$$

K_m and C_m are the indicators to differentiate the energy dissipation regime and the fluid storage regime, respectively. It is observed in Eq. (13) that K_m is time-independent, and C_m is time-dependent. C_m always evolves from zero to infinity along a straight evolution line as shown in Fig. 3 if it has a non-zero leak-off coefficient. This means on the beginning the fluid is mainly stored in the fracture and the injection efficiency is close to 1, while later the injection efficiency get decreased as more fracture surface is exposed to leak-off.

According to K_m, hydraulic fracturing propagation regimes can be divided into the toughness-dominated, the intermediate, and the viscosity-dominated ones. There exists no definite boundary to differentiate different regimes. According to the work by Hu and Garagash [16], it is reasonable to assume that the regime is toughness-dominated if its K_m is larger than 4.0, the regime is viscosity-dominated if its K_m is smaller than 1.0, otherwise the regime is intermediate. These regimes can also be sub-divided according to C_m.

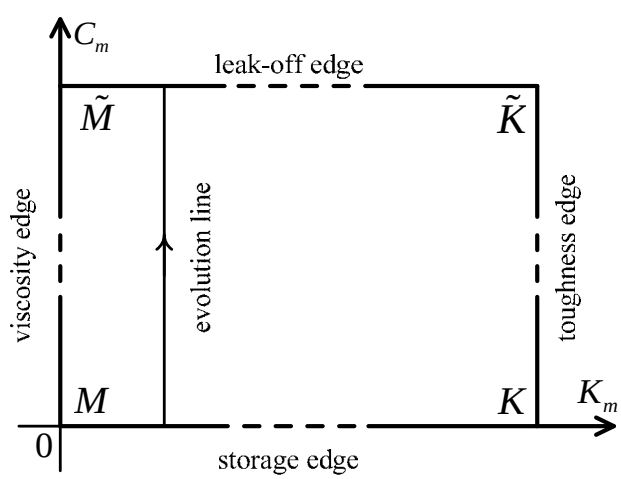

Figure 110 - Hydraulic fracturing regimes in (,) space and its evolution line (after [15]).

Hydraulic fracturing regimes can be presented by the introduction of a scaling technique [16], which transfers the variables p, w, and l in Eqs. (2) ~ (12) into dimensionless variables Π, Ω, and γ, respectively. The variables Π and Ω are functions of dimensionless coordinate ξ, which ranges from 0 at the inlet to 1 at the fracture tip. The scaling technique has the advantage of reducing the variables in hydraulic fracturing regimes to dimensionless quantities of order 0(1) whenever possible [16], and relieving the burden for constructing the asymptotic solutions. The key issue for the asymptotic solutions is to construct appropriate tip asymptote [13]. Some of the asymptotic solutions in the literature are introduced in brief as follows.

K and M vertex solutions

The K vertex regime corresponds to the case of zero fluid viscosity and zero leak-off. The K vertex solution has a uniform net pressure, and the second term on the right hand of the Eq. (5) is zero. Therefore, the fracture tip width has the asymptote of $(1-\xi)^{1/2}$. In the *K* vertex asymptotic solution, the dimensionless opening is defined as [14]

$$\Omega(\xi) = 2^{-1/2}\gamma(1-\xi^2)^{1/2}$$

The M vertex regime corresponds to the case of zero fracture toughness and zero leak-off, and the second term on the right hand of Eq. (5) plays an important role. The near-tip fracture width has the asymptote of [6, 18]

$$\Omega(\xi) \sim (1-\xi)^{2/3}$$

The M asymptotic solution [17] is achieved by approximating Ω with a series of weighted Gegenbauer polynomial [36], where the weighted function has the form of $(1-\xi^2)^{2/3}$.

Near K and near M solutions

The asymptotic solutions for the near K and near M regimes, where there is no leak-off, are collectively denoted as $F(\xi) = \{\Omega(\xi),\ \Pi(\xi),\ \gamma\}$. The *n*-order approximation of self-similar $F(\xi)$ is [14, 16]

$$F(\xi) = \sum_{i=0}^{n} C^i F_i(\xi),\ F_i(\xi) = \{\Omega_i(\xi),\ \Pi_i(\xi),\ \gamma_i\}$$

where C equals K_m^{-4} for the near K asymptotic solution, and C equals K_m for the near M asymptotic solution. The K and M vertex asymptotic solutions are the zero-order approximation of the near K and near M asymptotic solutions.

$K\tilde{K}$ and M$\tilde{M}$edge solutions

The $K\tilde{K}$ edge regime corresponds to the cases of zero fluid viscosity with leak-off evolving from zero to infinity. The net pressure is uniform at any time. Like the K vertex solution, the $K\tilde{K}$ edge solution [15] also has the property of self-similarity, and the fracture tip always has the asymptote of $\Omega \sim (1-\xi)^{1/2}$.

For the $M\tilde{M}$ edge regime, the tip behavior evolves from $\Omega \sim (1-\xi)^{2/3}$ at small leak-off to $\Omega \sim (1-\xi)^{5/8}$ at large leak-off [6]. The transient solution is achieved by the application of an explicit finite difference scheme in a moving spatial grid and the displacement discontinuity method [37] with constant-strength dislocations [6].

Intermediate solution

Hu and Garagash [16] developed an asymptotic solution for the intermediate regime. In the intermediate solution, the net pressure function Π is proposed to have the form of

$$\Pi = \Pi_L + \Pi_s$$

where Π_L is a piecewise linear function, and Π_s is a singular function and has the form of $\ln(1-\xi^2)$. Π_s is proposed based on the analysis of the tip behavior. The solution is achieved by using the method of lines [14].

Elastic response using Finite Element Method

By discreticizing the equivalent model with finite elements as shown in Fig. 4, we can achieve a finite element equation, which describes the elastic response of the solid medium and is cast as

$$\boldsymbol{K}_u \Delta \boldsymbol{U} = \Delta \boldsymbol{F}$$

where $\boldsymbol{K}_u$ is the global assembly of the stiffness of the finite elements, $\Delta \boldsymbol{U}$ is the vector of nodal displacement increment, and $\Delta \boldsymbol{F}$ is the vector of the equivalent node force caused by the increment of net pressure.

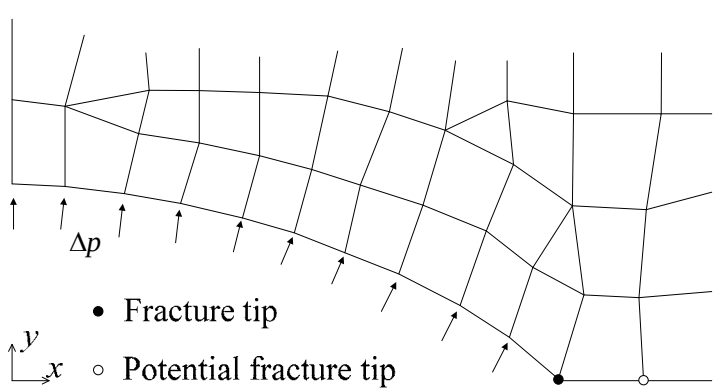

Figure 111 - Discretization of the equivalent quarter model with finite elements

As only net pressure increment has contribution to $\Delta \boldsymbol{F}$, Eq. (18) can be rewritten as

$$\boldsymbol{K}_u \Delta \boldsymbol{U} = \boldsymbol{B} \Delta \boldsymbol{P}$$

where $\Delta \boldsymbol{P}$ is a vector formed by the node pressure increment on the fracture surface as shown in Fig. 4, and matrix $\boldsymbol{B}$ plays the role to transfer the fluid pressure increment to equivalent node force.

The interaction integral method [38] is introduced to calculate K_I. For the plain strain model, the approximation of K_I is

$$K_I = E' \left\{ \int_A \left[\sigma_{ij} \frac{\partial u_i^a}{\partial x_1} + \sigma_{ij}^a \frac{\partial u_i}{\partial x_1} - \sigma_{mn}^a \varepsilon_{mn} \delta_{1j} \right] \frac{\partial \chi}{\partial x_j} dS - \int_{S_e} \chi p \frac{\partial u_i^a}{\partial x_1} dL \right\}$$

where domain A is a set of elements around the fracture tip as shown in Fig. 4, S_e is a set of edges of the finite elements in set A and these edges coincide with the fracture surface as shown in Fig. 5 with dashed line, σ_{ij} is the stress field, u_i is the displacement field, $x_j (j = 1, 2)$ is the local coordinate, δ is the Kronecker operator, χ is a scalar field, ε_{mn} is the strain field, and σ_{ij}^a and u_i^a are the auxiliary stress and displacement field, respectively. The analytical solutions of σ_{ij}^a and u_i^a are listed in Appendix A. Einstein summation convention is used for repeated indices in Eq. (20).

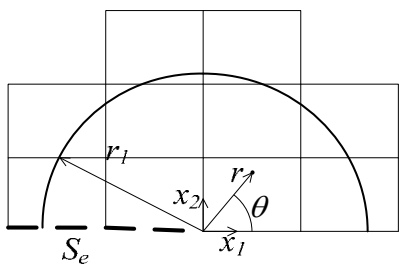

Figure 112 - Domain for the interaction integral

The characteristic radius r_c of the fracture tip is defined for the determination of domain A, and

$$r_c = \sqrt{A_{tip}}$$

where A_{tip} is the summation of the area of the elements which share the node on the fracture tip. Elements having node(s) in the semi-circle as shown in Fig. 5 set up the domain A, and the semi-radius of the circle equals r_c. The scalar χ is taken to have a value of unity for nodes in the semi-circle, and zero for nodes outside the semi-circle [32]. Theoretically, the interaction integral is independent of the domain A.

It is assumed in this paper that the propagation size at every step is determined by the finite element mesh. This means that the node on the tip is when K_I is not smaller than K_{IC}, and the fracture extends into the node ahead of the fracture tip as shown in Fig. . Similar assumptions can be found in the literature [32, 39].

Fluid flow in the fracture

Eq. (6) leads to its weak form [24] as

$$\int_{l_t}\left[-\nabla(\delta p)\cdot\boldsymbol{q}+(\delta p)\frac{\partial w}{\partial t}+(\delta p)g\right]dl+\delta p(\boldsymbol{q}\cdot n_1)\big|_S=0$$

where δp is a testing function, and S is the collection of boundary conditions in Eq. (10). Eq. (22) combined with Eq. (10) leads to a nonlinear finite element equation for fluid flow in the fracture[24], which is symbolically cast as

$$\boldsymbol{K}_w(\boldsymbol{W})\boldsymbol{P}+\boldsymbol{L}\dot{\boldsymbol{W}}+\boldsymbol{H}=\boldsymbol{0}$$

*where $\boldsymbol{W}$ is a vector formed by the widths of the nodes on the fracture surface, $\boldsymbol{K}_w(\boldsymbol{W})$ is the assembly of the flux stiffness of the fluid elements, **L** is the assembly of the length stiffness of the fluid elements, and **H** concludes the contributions of the fluid leak-off and the fluid injection.*

Taking time integration with Eq. (23), we have

$$\int_{t_n}^{t_{n+1}}\left[\boldsymbol{K}_w(\boldsymbol{W})\boldsymbol{P}+\boldsymbol{L}\dot{\boldsymbol{W}}+\boldsymbol{H}\right]dt=\boldsymbol{0}$$

Backward Euler scheme for time difference is used in this paper, so according to Eq. (24) we have

$$\boldsymbol{K}_w(\boldsymbol{W}_{n+1})\boldsymbol{P}_{n+1}\Delta t-\boldsymbol{L}(\boldsymbol{W}_{n+1}-\boldsymbol{W}_n)+\boldsymbol{H}\Delta t=\boldsymbol{0}$$

of which $\boldsymbol{W}_{n+1}$ and $\boldsymbol{P}_{n+1}$ are the unknown fracture width and net fluid pressure at the *n*+1-*th* step, respectively, $\boldsymbol{W}_n$ is the known fracture width at the *n-th* step, and Δt is the time step between the *n-th* step and the *n*+1-*th* step.

For the *n*+1-*th* step, we have

$$\boldsymbol{W}_{n+1}=\boldsymbol{W}_n+\Delta\boldsymbol{W},\ \boldsymbol{P}_{n+1}=\boldsymbol{P}_n+\Delta\boldsymbol{W}$$

For any moment, we have

$$\Delta u_y(x)=2\Delta w(x),\ 0\le x\le l_t$$

where Δu_y is the displacement increment in y direction on fracture surface in the equivalent quarter model, and Δw is the fracture width increment. Therefrore, Eq. (25) can be rewritten in a generalized way as

$$\boldsymbol{K}_w(\boldsymbol{U}_n+\Delta\boldsymbol{U})(\boldsymbol{P}_n+\Delta\boldsymbol{P})-\boldsymbol{L}'\Delta\boldsymbol{U}+\boldsymbol{H}\Delta t=\boldsymbol{0}$$

where $\boldsymbol{L}'$ determines the contribution of node displacement increment to fracture width increment.

Solution of coupled equations

It is obvious that the unknown fracture width increment and fluid pressure increment at *n*+1-*th* step can be obtained by solving the coupled Eqs. (19) and (28), with known fracture width and net fluid pressure at *n-th* step. The Newton-Raphson iteration algorithm [40, 41] is used to solve the non-linear coupled equations. In every step, the following condition is used as the convergence criterion

$$\left\|\Delta\boldsymbol{w}^{(m+1)}-\Delta\boldsymbol{w}^{(m)}\right\| / \left\|\Delta\boldsymbol{w}^{(m+1)}\right\| \le \varepsilon_{tol}$$

where $\| \ \|$ is the 2-norm operator, $\Delta\boldsymbol{w}^{(m+1)}$ and $\Delta\boldsymbol{w}^{(m)}$ is the result of fracture width increment after m+1_th iteration and m_th iteration, respectively, and ε_{tol} is the specified tolerance and it equals 1.0e-8 in this paper. In every step, the fracture doesn't propagate if the stress intensity factor is smaller than the fracture toughness.

It is seen that the essential work in the proposed method is to solve the coupled Eqs. (19) and (28). No special attention is paid to the fracture tip behavior whatever the hydraulic propagation regime is.

8.5. Derivation of Fracture efficiency Equations

The proppant velocity in x (horizontal) and y (vertical) directions can be written as follow:

$$v_x^p = v_x$$

$$v_y^p = v_y + v_{settle}$$

Settling velocity can be calculated using Stokes law, which describes a single spherical particle settling in an infinitely large environment[11]. The following equation holds when Reynolds number is less than 2.

$$V_\infty = \frac{g(\rho_p - \rho_f){d_p}^2}{18\mu}$$

For $2 < \mathrm{Re} < 500$ equation 7 changes to:

$$V_\infty = \frac{20.34(\rho_p - \rho_f)^{0.71} d_p^{1.14}}{\rho_f^{0.29}\mu^{0.43}}$$

And for $\mathrm{Re} \geq 500$ equation 9 described the proppant settling velocity as follow:

$$V_\infty = 1.74\sqrt{\frac{g(\rho_p - \rho_f)d_p}{\rho_f}}$$

Where ρ_p is proppant density, ρ_f is fracturing fluid density, d_p is proppant particle diameter, and μ is fluid viscosity, V_∞ is the falling velocity of a single particle in an infinitely large environment. Settling velocity of proppant can be obtained applying the polynomial correlation to V_∞ that includes the effect of proppant concentration (interaction between proppant particles) and fracture width. In this study, correction introduced by Gadde et. al., 2004 is applied in two steps to obtain settling velocity in equation 12 [21].

$$V_w = V_\infty\left[0.563\left(\frac{d_p}{w}\right)^2 - 1.563\left(\frac{d_p}{w}\right) + 1\right]$$

Where V_w is settling velocity corrected for fracture wall effect, V_∞ is uncorrected settling velocity, d_p is proppant particle diameter, w is fracture width.

$$V_c = V_\infty(2.37c^2 - 3.08c + 1)$$

Where V_c is the settling velocity corrected for proppant concentration effect, $V_\infty$is uncorrected settling velocity, and c is proppant concentration. Fluid viscosity also needs to be corrected as follow:

$$\mu = \mu_0\left\{1 + \left[0.75(e^{1.5n} - 1)e^{-\frac{\gamma(1-n)}{1000}}\right]\frac{1.25c}{1-1.5c}\right\}^2$$

In this case to account for non-Darcy flow effect Forchheimer equation can be used as follows:

$$\frac{1}{k_{app}} = \frac{1}{k} + 3.238 * 10^{-8}\frac{\rho\beta v}{\mu}$$

Where β is Non-Darcy factor or Forchheimer factor, k_{app} is the apparent permeability. Following correlation can be used to calculate Non-Darcy factor

$$\beta = 1.88 * 10^{10}k^{-1.47}\emptyset^{-0.53}$$

The fracture width at 0 closure stress"w_f'" can be obtained using proppant concentration and original fracture width after injection as follow:

$$w_f' = \mathrm{w}\,\frac{\mathrm{c}}{\mathrm{c_{max}}}$$

Where, w is original fracture width after injection, c is proppant concentration and c_{max} is maximum proppant concentration. Based on this equation the area where proppant concentration reaches the maximum value will hold the original fracture width, while the area where proppant concentration doesn't reach the maximum value will have smaller fracture width. The proppant pack permeability, k_f, can be theoretically estimated in terms of the proppant diameter, d_p, porosity, $\emptyset$, proppant sphericity, Φ, propped fracture width, w, and damage factor, DF, using the equation given below[24]

$$\mathrm{k_f} = \frac{\emptyset^3(\mathrm{d_p}\Phi)^2}{72\lambda_\mathrm{m}(1-\emptyset^2)}\left(1 + \frac{\mathrm{d_p}\Phi}{3(1-\emptyset)\mathrm{w}}\right)^{-2}(1 - \mathrm{DF})$$

Where $\lambda_m \approx 25/12$ for most of the porosity ranges in hydraulic fractures.

where the productivity index for gas reservoir is defined as:

$$J_g = \frac{q\mu z}{\bar{p}_r^2 - p_{wf}^2}$$

Where J_g is the productivity index of gas reservoir, z is the gas compressibility factor, μ is the gas viscosity, q is the gas flow rate in standard conditions, $\bar{p}_r$ is the reservoir average pressure, and p_{wf} is the flowing bottom hole pressure.

8.6. Derivation of Slip Tendency and Stress Relationships

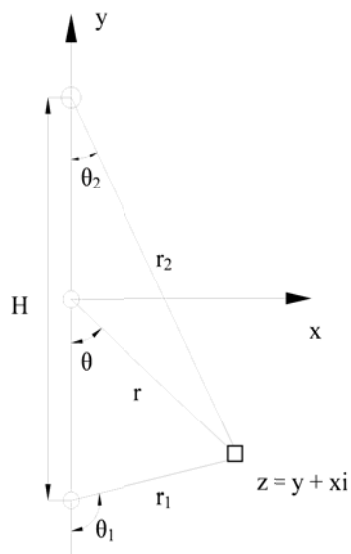

Figure 113 Analytical Solution of Stress Distribution Surrounding a Pressurized Fracture

The determination of slip tendency was performed using a projection of stresses found from the FEM analysis in accordance with **Figure 113** above (Qian Gao, 2013).

$$\frac{1}{2}\left(\Delta\sigma_y + \Delta\sigma_x\right) = -p_{net}\left(\frac{r}{\sqrt{r_1 r_2}}\cos(\theta - 0.5\theta_1 - 0.5\theta_2) - 1\right)$$

$$\frac{1}{2}\left(\Delta\sigma_y + \Delta\sigma_x\right) = p_{net}\left(\frac{2rsin\theta}{H}\right)\left(\frac{H^2}{4r_1 r_2}\right)^{\frac{3}{2}}\sin\left(\frac{3}{2}(\theta_1 + \theta_2)\right)$$

$$\Delta\tau_{xy} = -p_{net}\left(\frac{2rsin\theta}{H}\right)\left(\frac{H^2}{4r_1 r_2}\right)^{\frac{3}{2}}\cos\left(\frac{3}{2}(\theta_1 + \theta_2)\right)$$

$$\Delta\sigma_z = v\left(\Delta\sigma_y + \Delta\sigma_x\right)$$

Applying the general Coulomb Failure Criterion in terms of principle stresses the following relationship can be determined based upon the equation shown below.

$$\frac{\sigma_1}{\sigma_3} = \frac{S_1 - P_p}{S_3 - P_p} \geq \left[(\mu^2 + 1)^{\frac{1}{2}} + \mu\right]^2$$

Where σ_1 and σ_3 are the maximum and minimum principle stresses, respectively.

To determine the initial optimal angle of faulting, with angle θ to σ_1.

$$\theta = \frac{1}{2}\tan^{-1}\left(\frac{1}{\mu}\right)$$

The effects of shear and normal stresses across the fault plane are respective to the orientation of the fault.

$$\sigma_{n(\beta)} = \frac{1}{2}(\sigma_1 + \sigma_3) + \frac{1}{2}(\sigma_1 + \sigma_3)\cos 2\beta$$

$$\tau_{n(\beta)} = -\frac{1}{2}(\sigma_1 - \sigma_3)\sin 2\beta$$

Effective overburden pressure at a given depth is given below.

$$\sigma_v = \rho g z(1 - \lambda)$$

This is used to determine the limiting conditions in regards to the three types of faulting methods.

The T_s is a function of β in Eq. **Error! Reference source not found.**. For a given stress state, the maximum value of slip tendency (T_s) can be determined by taking the derivative of T_s with respect to 2β:

$$\frac{\partial T_s}{\partial(2\beta)} = \frac{(\sigma_1 - \sigma_3)(\sigma_1 + \sigma_3)cos2\beta + (\sigma_1 - \sigma_3)^2 - 2S_0(\sigma_1 - \sigma_3)sin2\beta}{[(\sigma_1 + \sigma_3) + (\sigma_1 - \sigma_3)cos2\beta]^2}$$

Knowing the derivative is equal to zero at slip tendency with a maximum value, cos2β can be obtained as follows:

$$co\,s(2\beta) = -\frac{\sigma_1 - \sigma_3 - 2S_0}{\sigma_1 + \sigma_3 + 2S_0}\ (\sigma_1 > \sigma_3 > 0)$$

Utilizing the Eq. **Error! Reference source not found.** to get a value of cos2β, inserting the value into the Eq. **Error! Reference source not found.** one can obtain the slip tendency (T_s) with a maximum value. Assuming earth's crust contains widely distributed faults and other discontinuities in all directions and in critical stress states, the slip tendency for a particular stress field should have a maximum value. At the scale of hydraulic fractures, smaller-scale fractures, which usually have a dominant orientation, and optimally oriented faults – if present – could also be in critical stress states around pressurized hydraulic fractures. In this study, we assume the cohesion strength on pre-existing faults is zero, which means S_0 = 0. Then the maximum slip tendency can be obtained, based on Eqs **Error! Reference source not found.** to **Error! Reference source not found.**, as follows:

$$T_{s\,max} = \frac{\frac{\sigma_1 - \sigma_3}{2}}{\sqrt{\left(\frac{\sigma_1 + \sigma_3}{2}\right)^2 - \left(\frac{\sigma_1 - \sigma_3}{2}\right)^2}} \qquad with \;\; cos(2\beta) = -\frac{\sigma_1 - \sigma_3}{\sigma_1 + \sigma_3}$$

Similar analyses are thoroughly discussed in Jaeger et al., (2007) and Zoback (2007). Based on Mohr-Coulomb law, Chin et al. (2012) proposed a method of factor of safety (SF), to evaluate the potential for shear and tensile failure in reservoir rock. In his paper the corresponding SFs for shear and tensile failures were discussed in detail, however, here different formulations are adopted since a quantitative measure of slip tendency is required for evaluating the fault stability. The slip tendency values are compared with friction coefficients of faults to quantify the stability state of the fault. Reactivation of fault is assumed to occur when the slip tendency is larger than the characteristic friction coefficient of a fault.

Normal Faulting Environment

The maximum and minimum principal stresses under the normal faulting environment are the vertical and minimum horizontal stresses, respectively ($\sigma_1 = \sigma_v$, $\sigma_3 = \sigma_{h,min}$). Substituting σ_1 and σ_3 into Eqs. **Error! Reference source not found.** and **Error! Reference source not found.**, the following expressions are found:

Before performing hydraulic stimulation

$$T_s = \frac{\sigma_v^0 - \sigma_{h,min}^0}{2\sqrt{\sigma_v^0 \sigma_{h,min}^0}}$$

$$with \;\; cos(2\beta) = -\frac{\sigma_v^0 - \sigma_{h,min}^0}{\sigma_v^0 + \sigma_{h,min}^0} \quad \left(\sigma_v^0 > \sigma_{h,min}^0 > 0\right)$$

During hydraulic stimulation

$$T_s = \frac{\frac{1}{2}(\sigma_v - \sigma_{h,min})sin(2\beta) - \tau_{vh}cos(2\beta)}{\frac{1}{2}(\sigma_v + \sigma_{h,min}) + \frac{1}{2}(\sigma_v - \sigma_{h,min})cos(2\beta) + \tau_{vh}sin(2\beta)}$$

$$\frac{1}{2}(\sigma_v + \sigma_{h,min}) = \frac{1}{2}(\sigma_v^0 + \sigma_{h,min}^0) - p_{net}\left(\frac{r}{\sqrt{r_1 r_2}}cos(\theta - 0.5\theta_1 - 0.5\theta_2) - 1\right)$$

$$\frac{1}{2}(\sigma_v - \sigma_{h,min}) = \frac{1}{2}(\sigma_v^0 - \sigma_{h,min}^0) + p_{net}\frac{2r\,sin\theta}{H}\left(\frac{H^2}{4r_1 r_2}\right)^{\frac{3}{2}} sin\left(\frac{3}{2}(\theta_1 + \theta_2)\right)$$

$$\tau_{vh} = \tau_{vh}^0 - p_{net}\frac{2r\,sin\theta}{H}\left(\frac{H^2}{4r_1 r_2}\right)^{3/2} cos\left(\frac{3}{2}(\theta_1 + \theta_2)\right)$$

where σ_v^0 and $\sigma_{h,min}^0$ are the initial vertical and minimum horizontal principal stresses, respectively. τ_{vh}^0 is the initial shear stress in vertical plane striking to the direction of minimum horizontal stress, τ_{vh} is the shear stress after applying hydraulic pressure. θ is calculated based on the initial stress state

Strike-Slip Faulting Environment

Before performing hydraulic stimulation

$$T_s = \frac{\sigma_{H,max}^0 - \sigma_{h,min}^0}{2\sqrt{\sigma_{H,max}^0 \sigma_{h,min}^0}}$$

$$with \quad cos(2\beta) = -\frac{\sigma_{H,max}^0 - \sigma_{h,min}^0}{\sigma_{H,max}^0 + \sigma_{h,min}^0} \quad (\sigma_{H,max}^0 > \sigma_{h,min}^0 > 0)$$

During hydraulic stimulation

$$T_s = \frac{\frac{1}{2}(\sigma_{H,max} - \sigma_{h,min})sin(2\beta) - \tau_{Hh}cos(2\beta)}{\frac{1}{2}(\sigma_{H,max} + \sigma_{h,min}) + \frac{1}{2}(\sigma_{H,max} - \sigma_{h,min})cos(2\beta) + \tau_{Hh}sin(2\beta)}$$

$$\sigma_{H,max} = \sigma_{H,max}^0 + \Delta\sigma_{H,max}$$

$$\sigma_{h,min} = \sigma_{h,min}^0 + \Delta\sigma_{h,min}$$

$$\Delta\sigma_{H,max} = -2\nu p_{net}\left(\frac{r}{\sqrt{r_1 r_2}}cos(\theta - 0.5\theta_1 - 0.5\theta_2) - 1\right)$$

$$\Delta\sigma_{h,min} = -p_{net}\left(\frac{r}{\sqrt{r_1 r_2}}cos(\theta - 0.5\theta_1 - 0.5\theta_2) - 1\right) - p_{net}\frac{2r\,sin\theta}{H}\left(\frac{H^2}{4r_1 r_2}\right)^{3/2} sin\left(\frac{3}{2}(\theta_1 + \theta_2)\right)$$

$$\tau_{Hh} = 0$$

Analysis of Eqs. **Error! Reference source not found.** to **Error! Reference source not found.** indicates that all stresses can be normalized by $\sigma_{h,min}^0$ and all lengths can be normalized by the fracture height *H*.

The final form of the solutions for semi-infinite crack are listed in the following:

$$\frac{1}{2}(\Delta\sigma_y + \Delta\sigma_x) = -p_{net}\left(\frac{r}{\sqrt{r_1 r_2}}cos(\theta - 0.5\theta_1 - 0.5\theta_2) - 1\right)$$

$$\frac{1}{2}(\Delta\sigma_y - \Delta\sigma_x) = p_{net}\frac{2r\,sin\theta}{H}\left(\frac{H^2}{4r_1 r_2}\right)^{\frac{3}{2}} sin\left(\frac{3}{2}(\theta_1 + \theta_2)\right)$$

$$\Delta\tau_{xy} = -p_{net}\frac{2r\,sin\theta}{H}\left(\frac{H^2}{4r_1 r_2}\right)^{\frac{3}{2}} cos\left(\frac{3}{2}(\theta_1 + \theta_2)\right)$$

$$\Delta\sigma_z = \nu(\Delta\sigma_y + \Delta\sigma_x)$$

where $\Delta\sigma_x$, $\Delta\sigma_y$ and $\Delta\tau_{xy}$ are stress changes when applying hydraulic pressure. p_{net} is the fracture pore pressure in excess of minimum horizontal stress σ_{hmin}, H the fracture height, and v is Poisson's ratio, r distance from fracture center to point, r_1 distance from negative fracture tip to point, r_2 distance from positive fracture tip to point, ϑ angle from fracture center to point, ϑ_1 angle from negative fracture tip to point, and ϑ_2 angle from positive fracture tip to point. Detailed mathematical development can be found in Sneddon and Elliot (1946).